

EXPERIMENTAL STUDY OF A LOW-FREQUENCY
THERMOACOUSTIC DEVICE

A Thesis

Submitted to the Faculty

of

Purdue University

by

Ariana G. Martinez

In Partial Fulfillment of the

Requirements for the Degree

of

Master of Science in Aeronautics and Astronautics

December 2019

Purdue University

West Lafayette, Indiana

THE PURDUE UNIVERSITY GRADUATE SCHOOL
STATEMENT OF THESIS APPROVAL

Dr. Stephen Heister, Chair

School of Aeronautics and Astronautics

Dr. Carlo Scalo

School of Mechanical Engineering

Dr. Timothee Pourpoint

School of Aeronautics and Astronautics

Dr. Mario Migliorino

Department of Mechanical and Aerospace Engineering, Sapienza University of
Rome

Approved by:

Dr. Gregory A. Blaisdell

Head of the School Graduate Program

To Jill

ACKNOWLEDGMENTS

First, thanks to Pat Sweeney and everyone at Rolls Royce who provided input and guidance through this project.

Next, I would like to thank Dr. Scalo and Dr. Migliorino for providing an immense amount of expertise, support, and enthusiasm to this project. Their involvement has been invaluable.

Finally, I would like to thank three mentors who have helped me grow to where I am today. First, Scott Meyer, who taught me how to be an experimentalist. Second, Dr. Pourpoint, who has been a mentor to me since undergrad, and for that I am grateful. Finally, Dr. Heister, who I am incredibly lucky to be able to call my advisor.

TABLE OF CONTENTS

	Page
LIST OF TABLES	vii
LIST OF FIGURES	viii
SYMBOLS	xiii
NOMENCLATURE	xvi
ABSTRACT	xvii
1 INTRODUCTION	1
1.1 Motivation	2
1.2 Literature Review	2
1.2.1 Historical Context	3
1.2.2 Background	4
1.2.3 Literature on Energy Extraction	9
1.2.4 Previous Work with R-218	21
1.2.5 Linear Stability and Navier-Stokes Models	25
2 EXPERIMENTAL FACILITY	30
2.1 Experimental Objectives	30
2.2 Test Article Design	32
2.2.1 System Overview	32
2.2.2 Instrumentation	34
2.2.3 Heat Exchanger	35
2.2.4 Resonator Sections	38
2.2.5 Supporting Hardware	43
2.3 Preliminary Analysis	49
2.3.1 Resonator Structural Analysis	50
2.3.2 Heat Transfer Analysis	51
2.3.3 Microtube Structural Analysis	58
2.3.4 Water Mass Flow Rate	60
2.3.5 Oil Mass Flow Rate	60
2.3.6 Uncertainty Analysis	63
3 EXPERIMENTAL RESULTS	70
3.1 Testing and Data Analysis Methods	73
3.2 Test Matrix A: Gen. 1 Rig Test Results	74
3.2.1 Oil and Water Adjustments	78

	Page
3.2.2	Phasing of Pressure Amplitude with Axial Location 78
3.2.3	Temperatures in the Stack 79
3.3	Test Matrix B: Variance of Bulk Pressure and ΔT 81
3.3.1	Predictions on Expected Behavior 82
3.3.2	Variance of Bulk pressure and ΔT Results 83
3.3.3	Modeling Validation 85
3.3.4	Waveform Shape 86
3.3.5	Time Averaged Pressure Variations 89
3.3.6	Investigation of Phase Angle 90
3.3.7	Temperature Gradient Linearity 92
3.3.8	"Sloshing" Behavior 92
3.3.9	Pressure Excursions at high Heating Conditions 94
3.4	Test Matrix C: Variance of Resonator Length 94
3.4.1	Waveform Shape for Various Resonator Lengths 96
3.5	Assessment of Pumping Characteristics 97
3.5.1	Test Matrix D: Pumping Tests at $\Delta T = 116K$ 99
3.5.2	Test Matrix E: Pumping Tests at $\Delta T = 134K$ 101
3.5.3	Test Matrix F: Pumping Tests at $\Delta T = 150K$ 107
3.5.4	Assessment of Power Extraction 110
4	CONCLUSIONS AND FUTURE WORK 113
4.1	Summary of Results 113
4.2	Future Work 114
4.2.1	Energy Extraction Options 114
4.2.2	Generation 3 Rig 117
4.3	Lessons Learned 117
	REFERENCES 120
A	Supplementary Material 124
A.1	Hot Side Cavity Technical Drawing 125
A.2	Resonator Section 1 Technical Drawing 126
A.3	Resonator Section 3 Technical Drawing 127
A.4	End Cap Technical Drawing 128
A.5	Duratherm G Technical Data Sheet 129
A.6	Bladder Accumulator Technical Drawing 132
A.7	Procedures 133
A.8	Complete Test Results 146

LIST OF TABLES

Table	Page
1.1 Summary of Previous Experimental Energy Extraction Methods	20
1.2 Critical Conditions for R-218	22
2.1 Major Rig Dimensions	32
2.2 Heat Transfer Fluid Properties	56
2.3 Heat Exchanger Geometric Parameters	56
2.4 Temperature Measurements	65
2.5 Uncertainty Limits	67
2.6 Computed Uncertainty	68
3.1 Test Summary	72
3.2 Test Matrix # 1: Vary ΔT and Bulk Pressure	81
3.3 Test Matrix C: Varied Resonator Length	95
3.4 Test Matrix D: Pumping Tests at $\Delta T = 116K$	99
3.5 Test Matrix E: Pumping Tests at $\Delta T = 134K$	101
3.6 Test Matrix F: Pumping Tests at $\Delta T = 150K$	108
4.1 Gen. 2 and Gen. 3 Rig Comparison	117

LIST OF FIGURES

Figure	Page
1.1 Sketch of a thermoacoustic device showing basic components.	5
1.2 Ceperley’s traveling-wave engine concept, adapted from Swift. This configuration demonstrates both a heat pump (cold to hot) and a prime mover (hot to cold) configuration.	8
1.3 model of pressure and velocity waves for a standing-wave configuration (left) and a traveling wave configuration (right). the X-axis represents the axial location in a resonator, and amplitude is the wave amplitude. the color change from light to dark shows the wave behavior with time. TEC stands for thermoacoustic energy converter. From Callanan [22].	9
1.4 Diagram of impulse and Wells turbines, showing geometry and velocity parameters. v_∞ is the incoming fluid velocity and v_{imp} is the impinging fluid velocity on the rotor.	11
1.5 numerical evaluation of turbine efficiency for different types of self-rectifying turbines used in OWCs. Airflow coefficient is computed as the ratio of axial flow velocity to circumferential velocity of the turbine. Data from [27], adapted from [28].	12
1.6 Experimental setup of bi-directional turbine with alternator. Turbine operates with air at atmospheric pressure at various operating frequencies, ranging from 20-50 Hz. from de Blok et al. [30]	13
1.7 Experimental results obtained for rotor efficiency as a function of acoustic input power, from de Blok et al. [30].	13
1.8 Alternator efficiency as a function of rotor rotational speed in automotives, from Remy Inc.	15
1.9 CAD model of a typical looped-tube thermoacoustic engine utilizing linear alternators, from Wu et al. [36].	17
1.10	18

Figure	Page
1.10 Diagrams of experimental setups for various thermoacoustic engines utilizing linear alternators for energy extraction. The efficiencies cited refer to thermal-to-electric efficiency. The electric powers cited refer to electric power produced at peak efficiency, although many of these experiments demonstrated larger maximum power outputs at lower efficiencies. All experiments shown used helium as the working fluid.	19
1.11 Plots showing density (left) and specific heat (right) of R-218 in its trans-critical region, from Alexander et al. [2].	21
1.12 Plots showing Coefficient of thermal expansion for R-218 at pressures varying about the critical point (2.37-3.49 MPa) and helium for pressures ranging from 0.69-6.89 MPa and the operating temperature range cited in Backhaus and Swift.	23
1.13 Schematic of rig constructed and modeled in work by Alexander et al. [2].	24
1.14 Stacks used in experimentation from Alexander [4].	25
1.15 Computational modeling setup of Migliorino and Scalo [44].	26
1.16 Modeling results of Migliorino and Scalo showing optimal geometry based on growth rate Isolevels for various temperature differences. These results apply to CO_2 as the working fluid, with a bulk pressure of 10 MPa, $\Delta T = 100K$ (a), $\Delta T = 125K$ (b), and $\Delta T = 150K$ (c).	27
1.17 Axial Distribution of Pressure (a), mass flow rate (b), and phasing (c) computed from predictive models by Migliorino and Scalo. The solid line shows linear stability model results and circles show Navier-Stokes model results.	28
2.1 Diagram of major components in thermoacoustic device.	32
2.2 CAD of Test Article.	33
2.3 Plumbing & Instrumentation Diagram of thermoacoustic test article.	35
2.4 CAD Model of heat exchanger used in test campaign, designed with the help of Mezzo Technologies Engineers. Microtube bundle is 12.0 cm long and 2.35 cm in diameter.	36
2.5 CAD Model of heat exchanger showing thermocouple placement	37
2.6 Scale CAD of microtube stack showing tube spacing.	38
2.7 Features and dimensions of hot side cavity.	39
2.8 Features and Dimensions of Resonator Section 1.	40

Figure	Page
2.9 CAD image showing features and dimensions of Resonator Section 2 (left) and image of resonator construction showing features and dimensions of Resonator Section 2 (right). Dimensions are in cm.	41
2.10 Features and Dimensions of Resonator Section 3.	42
2.11 Features and dimensions of recirculation line.	43
2.12 Image of Oil Heating and Circulation System.	44
2.13 Image of Water Cooling System.	46
2.14 Image of Bladder Accumulator (left) and Technical Drawing of Bladder Accumulator showing internal structure (right).	47
2.15 Image of supporting hardware used for refrigerant loading, reclaiming, and storage.	48
2.16 Data acquisition system used for monitoring and recording data.	49
2.17 Results of ANSYS structural analysis conducted on Resonator Section 3 at 6.9 MPa (1000 psi).	50
2.18 Results of ANSYS structural analysis conducted on Resonator Section 1 and Hot Side Cavity at 6.9 MPa (1000 psi).	51
2.19 Schematic of Heat Transfer Analysis for a bank of tubes in crossflow. . . .	52
2.20 Heating and cooling fluid predicted mass and volumetric flow rate requirements as a function of $ T_i - T_s $	56
2.21 Heating and cooling fluid predicted Reynolds number as a function of $ T_i - T_s $.	57
2.22 Heating and cooling fluid predicted friction factor as a function of $ T_i - T_s $.	57
2.23 Heating and cooling fluid predicted pressure drop as a function of $ T_i - T_s $.	58
2.24 Schematic of structural analysis performed on a single microtube acting as a doubly-fixed beam.	59
2.25 Measured oil mass flow rates at varying temperature and pump speed with uncertainty.	62
2.26 Acoustic power of sample data showing uncertainty. The locations of pressure transducers are highlighted in schematic for reference	69
3.1 Schematic of test article setup for Test 1	74
3.2 Experimental results obtained from the Gen. 1 rig	75

Figure	Page
3.3 Experimental results gathered by Dayle Alexander [4] of a test conducted using the heating cartridge with equal resonator length and similar bulk pressure to Test 1.	77
3.4 Schematic of test article setup for tests 2-4.	79
3.5 Windowed raw data of test 2 showing in-phase pressure oscillations during limit cycle.	79
3.6 Temperature profile in the stack for each test.	80
3.7 Sound Speed at temperatures and bulk pressures used in experimental results	83
3.8 Experimental Results showing plots of thermoacoustic behavior with varying bulk pressure and ΔT	84
3.9 Numerical predictions validated by experimental results for test condition at 1.1 P/P_{cr} , provided by Dr. Migliorino.	86
3.10 Test Article configuration showing location of pressure transducers.	87
3.11 Experimental Results showing plots of waveform behavior along the resonator with varying bulk pressure and ΔT . x/L is the relative axial location along the resonator and L is the total resonator length (239 cm).	88
3.12 Difference in bulk pressure between PT-TA-01 and PT-TA-07 at all test conditions	90
3.13 Experimental Results showing plots of phase angle along the resonator with varying bulk pressure and ΔT . x/L is the relative axial location in the resonator and L is the total resonator length (239 cm).	91
3.14 Experimental Results showing behavior of the temperature gradient with varying bulk pressure	92
3.15 Experimental Results showing chugging behavior observed in two tests	93
3.16 Experimental results with additional data to demonstrate repeatability	94
3.17 Experimental results showing plots of thermoacoustic behavior with varying resonator length at a constant ΔT of 116 K	96
3.18 Experimental Results showing plots of waveform behavior along the resonator with varying bulk pressure and resonator length	97
3.19 Schematic of tests conducted to assess pumping characteristics	98
3.20 Experimental results obtained from Test Matrix D of pumping assessment	100
3.21 Experimental results obtained from Test Matrix E of pumping assessment	102

Figure	Page
3.21 Progression of pressure behavior as fluid is recirculated. The example shown here is for $\Delta T = 134K$ and $P/P_{cr} = 1.2$	105
3.22 Comparison of temperature and mass flow rate of chugging response and sustained thermoacoustic response to demonstrate fluid jet injection into hot side cavity.	106
3.23 Picture demonstrating valve imaging method	107
3.24 Experimental results obtained from Test Matrix 5 of pumping assessment.	109
3.25 Mass flow rate vs pressure amplitude for all tests conducted in test Matrices 3,4,5. Line style indicates specified ΔT , marker shape indicates specified bulk pressure, and color indicates region of operation.	110
3.26 Pumping power vs percentage of acoustic power used for all tests conducted in Test Matrices D, E, and F.	111
3.27 Pumping power vs bulk pressure for peak power obtained at each ΔT and bulk pressure condition.	112
4.1 Piston system concept	115
4.2 Flexible membrane concept	115
4.3 Frictionless piston, image from Thales Cryogenics	116
4.4 Bi-directional turbine concept	116

SYMBOLS

φ	porosity
n	number (quantity)
N_{tubes}	number of tubes in the stack
d	inner diameter (m)
D_{stk}	diameter of stack (m)
\dot{m}	mass flow rate (kg/s)
ρ	density (kg/m^3)
V	volume (m^3)
t	time (s)
δ	uncertainty
δ_k	thermal penetration depth (m)
α_{th}	thermal diffusivity (m^2/s)
σ	standard deviation
\dot{Q}	thermal power (W)
C_p	specific heat capacity at constant pressure
T	temperature (K)
μ	dynamic viscosity ($Pa \cdot s$)
\mathcal{L}_T	nondimensionalized length in the transverse direction
\mathcal{L}_L	nondimensionalized length in the longitudinal direction
h	heat transfer coefficient (W/m^2K)
T_i	incoming fluid temperature (K)
T_o	outlet fluid temperature (K)
T_s	surface temperature (K)
v_i	incoming fluid velocity (m/s)
v_{max}	maximum velocity that occurs in the heat exchanger (m/s)

S_T	transverse tube spacing (m)
S_L	longitudinal tube spacing (m)
S_D	diagonal tube spacing (m)
ΔT_{lm}	log mean temperature difference (K)
\dot{W}	acoustic power (W)
k	constant for determining acoustic power output (W/KPa^2)
k_{th}	thermal conductivity (W/mK)
P	pressure amplitude (KPa)
ε	system efficiency
α_p	coefficient of thermal expansion at constant pressure (J/s)
η_c	Carnot efficiency
u	velocity (m/s)
f	acoustic frequency (Hz)
f_f	friction factor
a	speed of sound (m/s)
λ	wavelength (m)
l_{cav}	hot side cavity length (cm)
l_{stk}	stack length (cm)
L	resonator length (cm)
α	growth rate (Hz)
x	axial location along resonator (cm)
\dot{V}	volumetric flow rate (L/s)
ΔT_{HC}	temperature difference between incoming hot side temperature and incoming cold side temperature (K)
F_{dist}	distributed load (N/m)
ΔP_{tube}	pressure drop across a single microtube
M	moment (Nm)
σ_s	stress (MPa)
s	section modulus (m^3)

I	moment of inertia (m^4)
V	volume (m^3)
t	time (s)
P_{cr}	critical pressure (MPa)
P/P_{cr}	ratio of bulk pressure to critical pressure
\dot{W}_{pump}	acoustic power (W)

NOMENCLATURE

PID	proportional integral derivative
P&ID	Plumbing and Instrumentation Diagram
CAD	Computer Aided Design
DAQ	Data Acquisition System
OD	outer diameter
ID	inner diameter
GPM	gallons per minute
FSO	full scale output
R-218	octafluoropropane
TTE	Transcritical thermoacoustic engine
TAE	Thermoacoustic Engine
TAD	Thermoacoustic Driver
OPTR	orifice pulse tube refrigerator
TADOPTR	Thermoacoustically driven orifice pulse tube refrigerator
MEOP	Maximum expected operating pressure
FFT	Fast-Fourier Transform

ABSTRACT

Martinez, Ariana M.S., Purdue University, December 2019. Experimental Study of a Low-Frequency Thermoacoustic Device . Major Professor: Dr. Stephen D. Heister.

An experimental study of a low-frequency transcritical thermoacoustic device has been conducted at Purdue University's Maurice J. Zucrow Laboratories. The purpose of this study was to characterize the thermoacoustic response of transcritical R-218 and assess its feasibility for energy extraction and waste heat removal. This rig operated as a standing-wave configuration and achieved pressure amplitudes as high as 690 KPa (100 psi) at a ΔT of 150 K and a bulk pressure of $1.3 P/P_{cr}$ (3.43 MPa). To the author's knowledge, this is the highest ever thermoacoustic pressure amplitude achieved in a non-reacting flow. The thermoacoustic response was characterized by varying ΔT and bulk pressure parametrically. The effect of resonator length was characterized in a set of tests where resonator length and bulk pressure was varied parametrically at a single ΔT . Finally, the feasibility for energy extraction was assessed in a set of tests which characterized the ability of the working fluid to pump itself through a recirculation line with check valves. This set of tests showed that the working fluid was able to create self-sustained circulation by inducing a pressure differential across the check valves with the thermoacoustic response. This circulation was induced while still maintaining a significant pressure amplitude, demonstrating promising results as a feasible method for energy extraction and waste heat removal.

1. INTRODUCTION

The term thermoacoustic refers to the conversion of heat to work or work to heat due to the contraction and expansion of a working fluid. The phenomenon was first documented in the mid-19th century, and the technology has rapidly developed since then. In the past century, efforts have been made to model and experiment with this effect - both exploiting the thermoacoustic effect when it is desired to extract energy, and attempting to mitigate it when the response is unwanted, such as in combustion processes [1].

A major appeal of using thermoacoustic engines is that they are able to utilize low-grade heat, or waste heat, to produce acoustic work [2]. This provides a unique opportunity for energy recycling in large systems where even the smallest fraction of energy losses can result in several thousand watts of waste heat. In addition to energy recycling, thermoacoustic devices can also be used to protect systems in cases where energy losses can cause the system to overheat.

The vast majority of studies conducted to exploit this phenomenon have utilized working fluids of air and helium because of their low Prandtl number and high ratio of specific heats, leading to a more efficient thermal diffusion [3]. However, up until 2018, no publicly available work had been found by the author on utilizing transcritical fluids as a working fluid. Because of the high density change when crossing the critical region, transcritical fluids have the potential for higher power outputs than traditional working fluids [4].

This research aims to characterize the thermoacoustic response of the refrigerant octafluoropropane (R-218) in its transcritical region, and assess its feasibility for energy extraction and waste heat removal. This thesis will be organized as follows: First, the motivation for this research as well as a review of literature will be presented.

Then, the facility and experimental setup will be described. Finally, experimental results and their comparison with modeling predictions will be presented.

1.1 Motivation

This project was initiated by the Rolls-Royce University Technology Center (UTC) for advanced Thermal Management in an effort to explore creative methods for thermal management in aircraft engines. Primary heat loads in aircraft come from engine lubrication oil, hydraulic fluid, environmental control systems, avionics, and other electrical systems [5]. When left unattended, these heat loads can exceed the hardware limitations, causing damage in the aircraft. Primarily, fuel is utilized as a coolant because it is readily available has the benefit of increased combustion efficiency with increasing temperature. However, problems arise in heated fuels past a certain temperature, including flashing, coking, and reduced combustion efficiency past its vaporization point [6]. Additionally, thermoacoustic instabilities can occur in fuel lines when supercritical fuel is exposed to uneven heating [7].

Experience with the damaging effects of transcritical and supercritical thermoacoustic instabilities in combustion processes and fuel lines have inspired the team here at Purdue and Rolls-Royce to pursue the exploitation of the thermoacoustic effect in transcritical fluids through the development of a transcritical thermoacoustic engine (TTE) for energy extraction and waste heat removal in fuel lines.

1.2 Literature Review

This literature review will begin with the historical context relevant to this research area, then will provide a background of general thermoacoustics. Next, a review of literature on energy extraction and refrigeration will be presented. Finally, a review of the research conducted here at Purdue in recent years will be presented, including the previous work done with R-218, and the linear stability model that has been used in tandem with this experimental research.

1.2.1 Historical Context

Saundhaus was the first to document studies of this phenomenon in 1850 when he noticed that heating the end of glass tubes caused the air inside to vibrate, resulting in sound [8]. The next major contribution came from Lord Rayleigh in 1877, who was the first to quantitatively describe thermoacoustic phenomenon, detailing that heat causes the fluid inside an open tube to expand, and the heat is rejected when the fluid condenses, resulting in sustained oscillations [9].

Between the 1940's and 1960's the phenomenon was recorded by cryogenics researchers, who noticed that liquid helium had a tendency to spontaneously oscillate inside hollow tubes. One of the first practical uses for thermoacoustics came from cryogenics researchers, who would dip a hollow tube inside liquid helium, and could measure the surface level from the resulting frequency and pressure amplitude generated by the thermoacoustic response [10,11].

In 1958, Marrison proposed that thermoacoustics could be used to convert heat into electricity with a standing-wave heat engine. Marrison patented a heat exchanger device without the use of a stack [12]. Shortly after, standing wave engines which utilized a stack to improve heat transfer were proposed [11,13].

In mathematically describing the thermoacoustic response, Kramers was the first to attempt such an effort 1949, but it was not until 1969 that Nicolas Rott was the first to successfully describe thermoacoustic theory mathematically [14–16]. Rott's linear thermoacoustic theory is widely used today in the thermoacoustics community as the basis for modeling.

In 1979, Ceperley was the first to introduce the concept of the traveling wave engine, which has a thermodynamic cycle equivalent to the Sterling cycle [17]. Traveling wave engines offer higher potential efficiencies because the pressure and velocity waves are phased such that there does not need to be a thermal delay, allowing for a more efficient exchange of heat [18]. Since Ceperley, research in developing thermoacoustic heat engines has focused on maximizing efficiency for both traveling-

wave and standing-wave configurations. In 1999, Backhaus and Swift reported the highest-ever thermal-to-acoustic efficiency of 30% with their torus-shaped traveling-wave engine [19]. While this engine did not have energy extraction methods, the publication set the stage for realizing substantial energy extraction capabilities in the 21st century.

1.2.2 Background

A thermoacoustic engine (TAE) has two modes of operation: it can either work as a heat engine or a heat pump. In a heat engine, heat put into the system, \dot{Q}_{hot} , causes a fluid to expand. Heat is then rejected from the system, \dot{Q}_{cold} , causing the fluid to then contract. This expansion and contraction results in a pressure oscillation of the working fluid and thus acoustic work, \dot{W} . In a heat pump, the reverse process occurs, where work in the form of acoustic pressure oscillations is put into the system, resulting in a transfer of heat from a cooling source to a heating source. This is also known as a refrigerant process. Thus, The Carnot efficiency, η_c , of any thermoacoustic device is given by Equation 1.1 [20].

$$\eta_c = \frac{\dot{Q}_{hot} - \dot{Q}_{cold}}{\dot{Q}_{hot}} \quad (1.1)$$

Swift shows the basic parts of the thermoacoustic engine (Figure 1.1). A TTE consists of a heating source, a cooling source, a stack, a resonator section, and a hot side cavity.

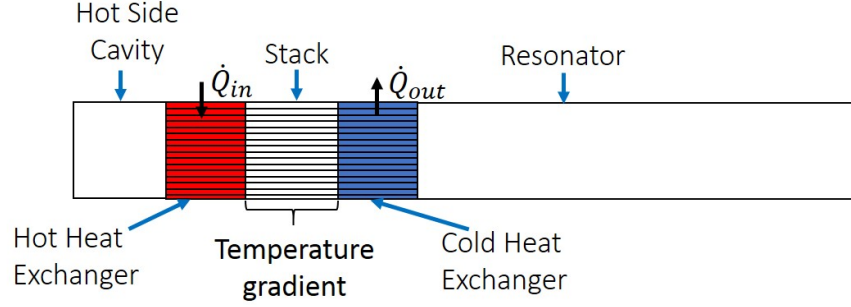


Figure 1.1. Sketch of a thermoacoustic device showing basic components.

Thermoacoustic "Stack"

The purpose of the "stack" is to carry heat to and from the working fluid. The stack can be made of any number of materials and geometries, but is typically a porous metal because it is desired to have fairly high thermal conductivity and small pores so heat can diffuse into the working fluid. This was explained by Swift in terms of thermal penetration depth. Thermal penetration depth, δ_k , is the distance heat can diffuse into the working fluid during one thermoacoustic period. This is given by:

$$\delta_k = \sqrt{\frac{2\alpha_{th}}{\omega}} \quad (1.2)$$

where α_{th} is the thermal diffusivity, and ω is the angular acoustic frequency. In order to diffuse heat efficiently, it is desired to make the spacing where fluid flows equal to $2\delta_k$. Spacing larger than the thermal penetration depth results in an inefficient diffusion of heat, while spacing smaller than this depth can result in attenuation of the wave [17,20]. This is why a majority of thermoacoustic studies utilize helium - the large thermal diffusivity of helium allows for larger pores, which is advantageous from a machinability standpoint. This parameter is commonly referred to as the *porosity*. The porosity, φ , is defined as the ratio of the cross sectional area of working fluid to total cross sectional area in the stack [2]. For a stack made up of many small tubes, as will be used in this experimental campaign, the porosity is given by Equation 1.3.

$$\varphi = N_{tubes} \left(\frac{D_i}{D_{stk}} \right)^2 \quad (1.3)$$

where D_i is the inner diameter of a single tube, and D_{stk} is the total diameter of the stack.

Heat Exchangers

The hot heat exchanger and cold heat exchanger, which can be considered thermal reservoirs, have an optimal length where a fluid parcel with a velocity, u , can pass through the reservoir on the "upswing" of the oscillation (defined at the positive peak, when $u = 0$), absorbing or rejecting heat, and exit the thermal reservoir on the "downswing" of the oscillation (defined at the negative peak, when $u = 0$), transferring heat down the stack. This approximately ideal length is computed by $2u/\omega$. Swift compares this process to a "bucket brigade", where fluid parcels are continuously moving back and forth, and as they do so, they are absorbing heat from the stack at one location, and rejecting it in another location, thus passing heat in between the heat exchangers.

Resonator

The resonator section serves the purpose of allowing the acoustic oscillations to fully develop, and dictates the acoustic frequency. The acoustic frequency, f , is given by Equation 1.4.

$$f = a/\lambda \quad (1.4)$$

where a is the sound speed and λ is the wavelength of sound, which is typically 2 to 4 times the resonator length for a standing-wave resonator with no energy extraction [21]. Because the thermal penetration depth is dependent on frequency, there an

optimal resonator length for a given stack configuration at which the penetration depth can be tuned to match the stack geometry, optimizing efficiency.

Hot Side Cavity

In a standing-wave engine, the hot side cavity is located to the left of the hot heat exchanger (see Figure 1.1). This portion of fluid acts as a spring, pushing the fluid in the stack back and forth such that it may transfer heat in the stack effectively. If the hot side cavity did not exist, there would be a node located immediately next to the hot heat exchanger where velocity would be zero, reducing the ability of the fluid in the stack to move and transfer heat.

Traveling vs Standing Wave Engines

Like standing-wave engines, a traveling-wave thermoacoustic engine (Figure 1.2), consists of a set of hot and cold heat exchangers on either end of a stack to induce a temperature gradient. The difference is that the resonator section is looped such that the pressure and velocity waves can travel around the system continuously, as opposed to back and forth.

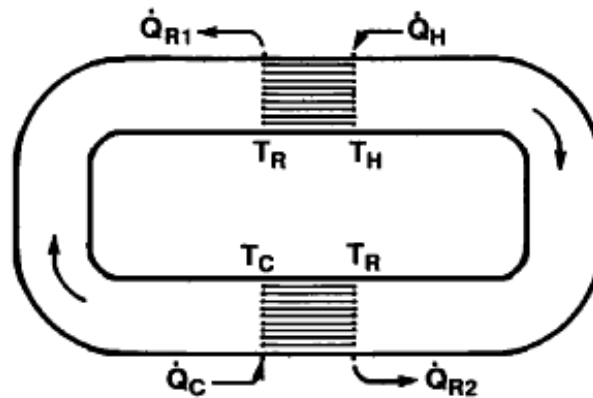


Figure 1.2. Ceperley's traveling-wave engine concept, adapted from Swift. This configuration demonstrates both a heat pump (cold to hot) and a prime mover (hot to cold) configuration.

Traveling-wave engines were first introduced by Ceperley to provide larger energy extraction capability because of phasing between pressure and velocity waves [17]. A pure standing wave configuration has phasing of 90° , which offers zero net work output. Standing-wave engines can only offer power output because of the time lag of imperfect heat transfer, which causes the phasing to shift from 90° . This results in a relatively poor efficiency. A pure travelling-wave engine, like a Sterling engine, has phasing of 0° or 180° , offering maximum work output. However, like standing-wave engines, there is also a phase shift due to the time lag of imperfect heat transfer, and this works to decrease the efficiency of traveling-wave engines. Since heat transfer in the stack is dependent on pore size, one would want to size a standing-wave stack such that the pores are large enough to shift the pressure and velocity waves by another 90° , resulting in 180° phasing and thus maximum work output. In contrast, the pores in a traveling wave stack would ideally be as small as possible in order to minimize the time lag and maintain the phasing as close to 180° as possible [17,22]. Figure 1.3 shows the wave behavior of a standing and traveling wave configuration in a resonator with time.

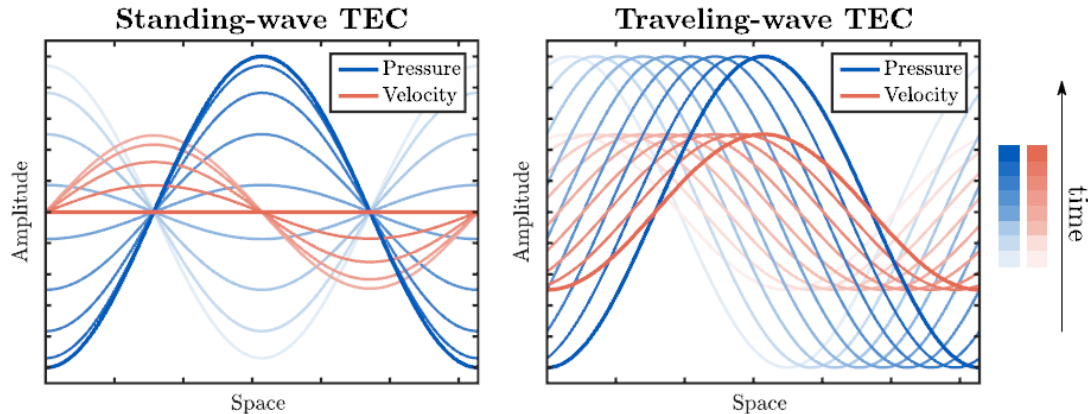


Figure 1.3. model of pressure and velocity waves for a standing-wave configuration (left) and a traveling wave configuration (right). the X-axis represents the axial location in a resonator, and amplitude is the wave amplitude. the color change from light to dark shows the wave behavior with time. TEC stands for thermoacoustic energy converter. From Callanan [22].

Like standing-wave engines, traveling-wave engines can either operate as a heat pump or a heat engine. The mode of operation is dependent of the direction of the fluid. When the working fluid travels from the hot end to the cold end of the stack, the wave is amplified and the system can work as a heat engine. When the fluid travels from the cold end to the hot end of the stack, the wave is attenuated and the device acts as a heat pump [17, 20].

1.2.3 Literature on Energy Extraction

Harnessing thermoacoustic waves for energy extraction is done by utilizing devices which can convert the mechanical energy of the acoustic waves into electrical energy. The most notable devices for achieving this are piezoelectric devices, bi-directional turbines, and linear alternator systems. Additionally, refrigeration is a method of utilizing acoustic energy which will be discussed. While much literature on modelling these devices in a thermoacoustic environment exists, this literature review will focus on experimental setups which have utilized these devices.

Piezoelectrics

A piezoelectric material is one which produces an electric potential from being mechanically strained. Piezoelectrics offer an attractive energy extraction option because they are arguably the simplest energy conversion method. Piezoelectrics require no dynamic sealing, and have no moving or rotating parts. The disadvantage is that piezoelectrics offer relatively low efficiencies compared to other options [23]. When introduced to a vibration, piezoelectrics operate at their maximum efficiency when they are vibrating at their resonant frequency [24]. Thus, when placed in a thermoacoustic device, the piezoelectric element needs to be sized so its resonant frequency matches the frequency of the resonator. because they offer energy conversion from mechanical strain, a piezoelectric device would ideally be placed in the location of highest pressure amplitude. In a standing-wave device, this occurs at the zero-velocity node, on either end of the resonator. Currently no work has been done on putting a piezoelectric energy converter in a traveling wave engine.

The only experimental attempt to utilize piezoelectrics in standing-wave engines has been made by Smoker et al.. They utilized low-pressure air oscillating at 388 HZ and were able to harvest .128 mW, achieving a peak thermal-to-electric efficiency of 9.7% [25].

Bi-Directional Turbines

A bi-directional turbine, also known as a self-rectifying turbine, is a device which can harvest energy in the presence of irregular fluid flow. Self-rectifying turbines were originally used for applications in energy harvesting of ocean waves, such as in oscillating water columns. In recent time, the application has spread to be applied to thermoacoustic devices [23]. Several types of self-rectifying turbines have been studied, including "Wells" turbines, and "impulse" turbines. Impulse and wells turbines consist of a rotor, which rotates to collect mechanical energy, and two sets of guide veins. Guide veins are placed on either end of the rotor to redirect incoming flow

in the direction which impinges on the rotor blades regardless of fluid direction [26]. The difference between Wells and impulse turbines are that Wells turbine blades are symmetric airfoils and impulse turbine blades are crescent-shaped. These types of turbines can have variations, such as biplane wells turbines, where there are two sets of airfoils instead of just one. Additionally, the guide vanes can be fixed, or self-pitch controlled. Self-pitch controlled guide vanes improve turbine efficiency while adding complexity in the form of a controller system and additional moving parts. A schematic for impulse and wells turbines are given in Figure 1.4.

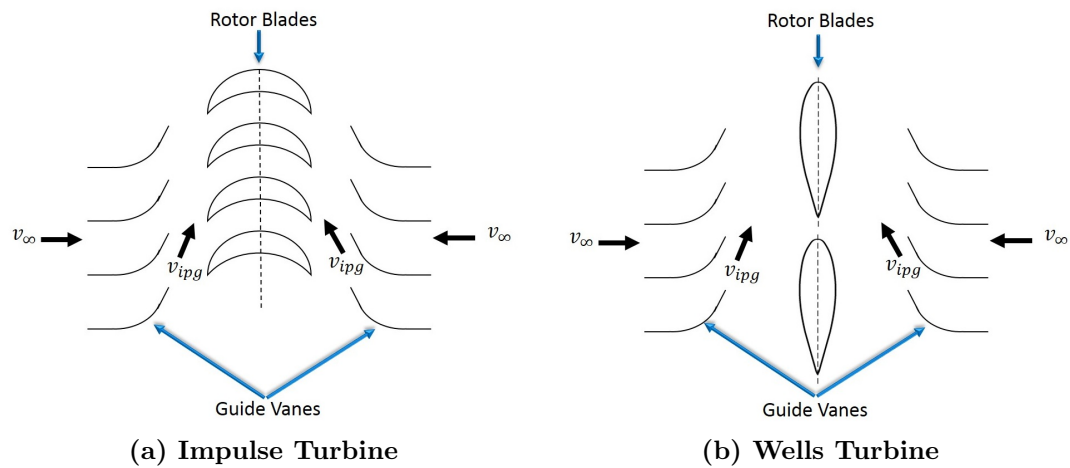


Figure 1.4. Diagram of impulse and Wells turbines, showing geometry and velocity parameters. v_∞ is the incoming fluid velocity and v_{ipg} is the impinging fluid velocity on the rotor.

Figure 1.5 shows numerically obtained turbine efficiencies as a function of air flow coefficient for several different types of Wells and impulse turbines used in OWCs. Air flow coefficient is defined as the ratio of axial flow velocity of circumferential velocity.

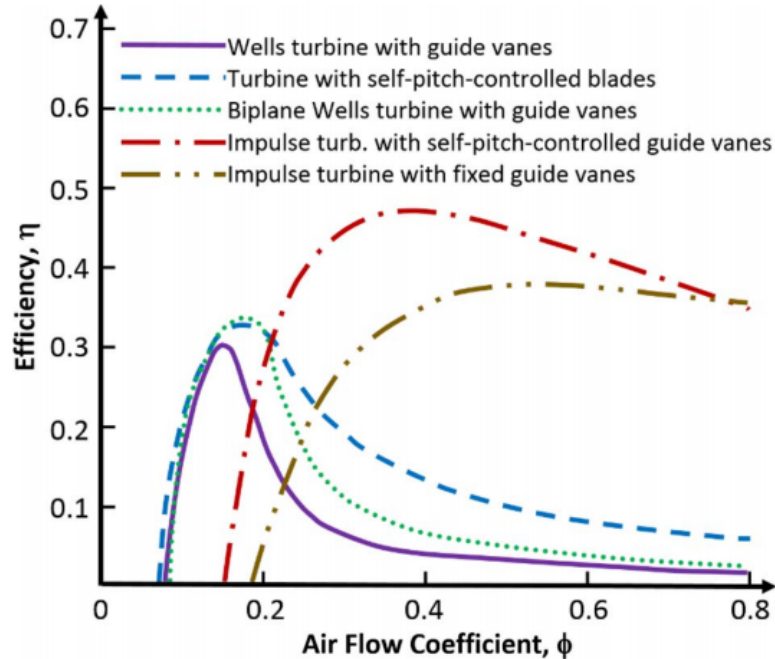


Figure 1.5. numerical evaluation of turbine efficiency for different types of self-rectifying turbines used in OWCs. Airflow coefficient is computed as the ratio of axial flow velocity to circumferential velocity of the turbine. Data from [27], adapted from [28].

Figure 1.5 shows that Wells turbines offer better performance at lower airflow coefficients, while impulse turbines offer better performance at higher airflow coefficients. This is because Wells turbines will stall at higher axial velocities [27–29].

The rotor torque is dependent on fluid velocity, and because of this, it is desired to place the turbine in the location of highest velocity. In a standing wave engine, this occurs in the middle of the resonator at the pressure node.

The work of de Blok et al. in 2014 [30] was the first study to apply a bi-directional turbine system to an acoustic device. In their device, they used a loudspeaker to provide acoustic power to air at atmospheric pressure, which turned an 84 mm diameter rotor. Their device is shown below in Figure 1.6.

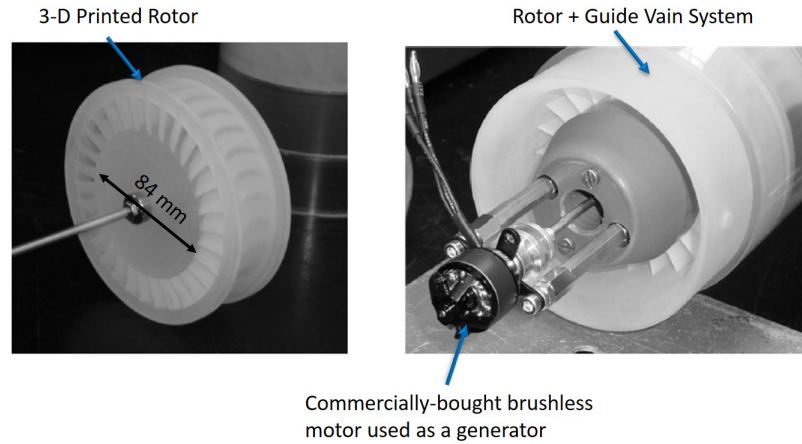


Figure 1.6. Experimental setup of bi-directional turbine with alternator. Turbine operates with air at atmospheric pressure at various operating frequencies, ranging from 20-50 Hz. from de Blok et al. [30]

The highest rotor efficiency obtained with this study was 31% (Figure 1.7) at a frequency of 20 Hz, and the experimental results of this study are shown below.

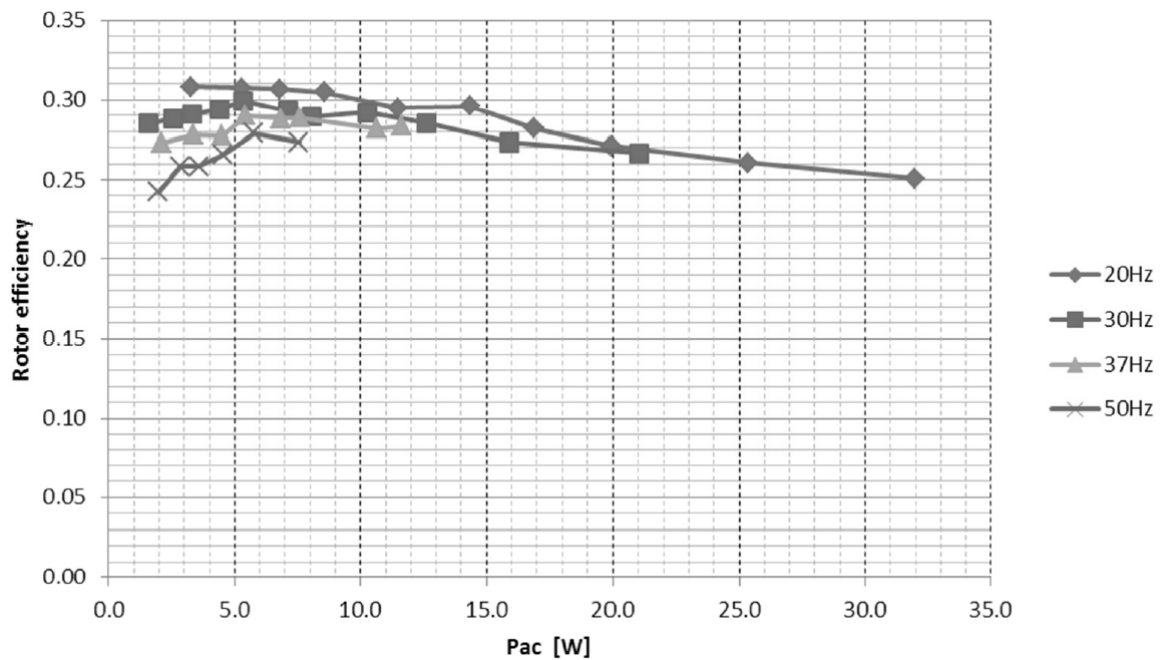


Figure 1.7. Experimental results obtained for rotor efficiency as a function of acoustic input power, from de Blok et al. [30].

Following this study, the authors conducted a scaled-up test in which the rotor diameter was increased from 84 mm to 300 mm and air was pressurized to 1 MPa (having a density of approximately 12 kg/m^3 at room temperature). The power source was changed from a loudspeaker to a thermoacoustic power generator with a thermal input power of 100 kW and an operating frequency of 16 Hz. They attained a rotor efficiency of 76% with this setup [30, 31]. The significant increase in rotor efficiency was attributed to the increase in density at higher pressure. Considering that the density of R-218 as a liquid is 1380 kg/m^3 , the results of this study show a promising potential for impulse turbines to be applied to a thermoacoustic device utilizing R-218.

The efficiency of the energy extraction can be divided into the acoustic-to-rotational conversion, which is done by the turbine, and the rotational-to-electric conversion, which is done by an alternator. Rotary alternators, most famously used for powering electric systems in cars, are a seasoned technology and are typically bought commercially for energy extraction in oscillating fluids [23]. The efficiency of rotary alternators for automotive applications is heavily dependent on rotational speed and peaks at 65% (Figure 1.8).

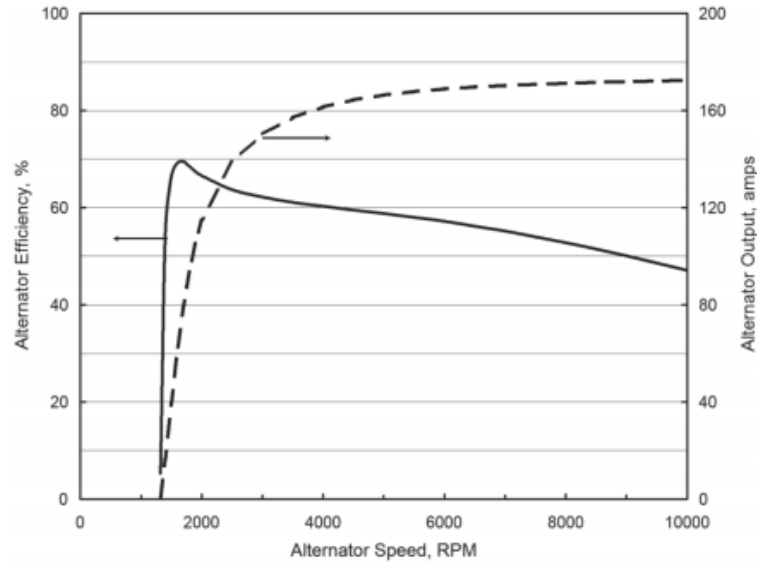


Figure 1.8. Alternator efficiency as a function of rotor rotational speed in automobiles, from Remy Inc.

A report from Remy Inc. [32] shows that after a steep increase in efficiency to reach the peak operating speed, the alternator efficiency decrease with increasing rotor speed. Because there is little focus on the efficiency of alternators in literature regarding energy extraction in oscillating fluids, it is unclear if this efficiency would remain consistent in a thermoacoustic application. While not yet proven, the impulse turbine and rotary alternator system have the potential to provide an acoustic-to-electrical efficiency of up to 62%, and it can be concluded that there is potential for future work in utilizing this setup.

Linear Alternators

A linear alternator system is one which uses a moving piston to drive electromagnetic inductance. Most commonly, the piston is attached to a magnet, or is a magnet, that moves back and forth through a coil to induce a current. Advantages of linear alternators are that they have been tested in thermoacoustic engines by several different sources, and they offer relatively high acoustic-to-electric efficiencies (51%-75%

has been reported). Disadvantages are that they may require dynamic sealing, adding frictional losses and increasing complexity. To combat dynamic sealing, "frictionless pistons" utilizing flexure bearings have been used [33]. Flexure bearing pistons are capable of having a seal gap of less than $10\mu m$. However, this seal gap can cause problems including streaming losses and a mean pressure difference between the front and back of the piston [34].

While low-impedance, or "ultra-compliant" linear alternators have been explored [34], the majority of testing has been done with high-impedance pistons. To extract energy with a high-impedance piston, it is necessary to place the piston at the location of high pressure fluctuations and for the resonance of the alternator and piston to match the frequency of the resonator [35]. Because of their high impedance and requirement to match the resonator frequency, linear alternator systems are advantageous in low-frequency high-amplitude devices.

Linear alternator systems have been the most tested form of energy extraction for thermoacoustic devices. Timmer et al. [23] compiled a list of successfully conducted research on thermoacoustic-linear alternator systems [33, 36–43]. The list consists of eight moving magnet alternators and one moving coil alternator, achieving thermal-to-electric efficiencies ranging from 12%-20%. A typical setup of a thermoacoustic-linear alternator engine shown in Figure 1.9. In this setup, a torus-shaped feedback tube is attached to a linear resonance tube, with the alternator system extracting energy at the intersection of the feedback tube and resonator.

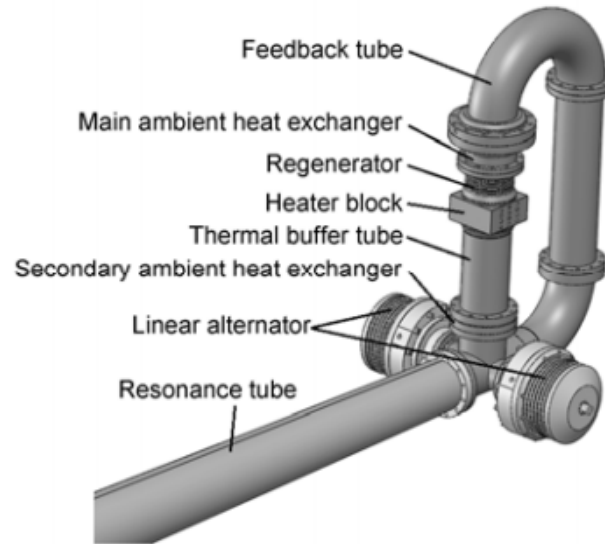
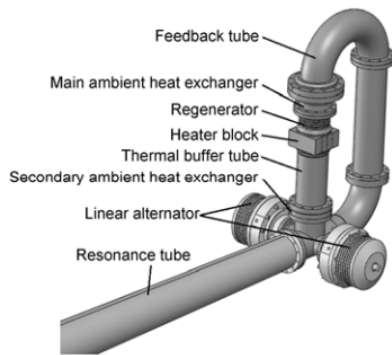
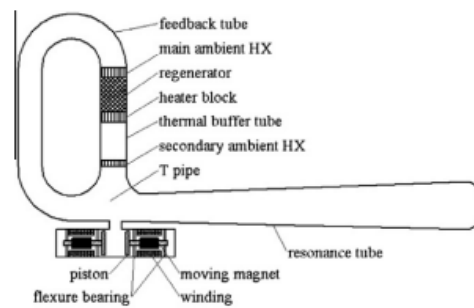


Figure 1.9. CAD model of a typical looped-tube thermoacoustic engine utilizing linear alternators, from Wu et al. [36].

Many variations in this design exist, and the experimentally-tested concepts can be seen below in Figure 1.10.



(a) 2011, $\eta = 15\%$, 451 W electric power [36]



(b) 2012, $\eta = 15\%$, 481 W electric power [37]

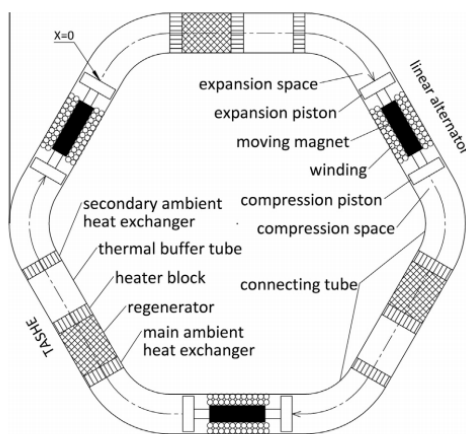
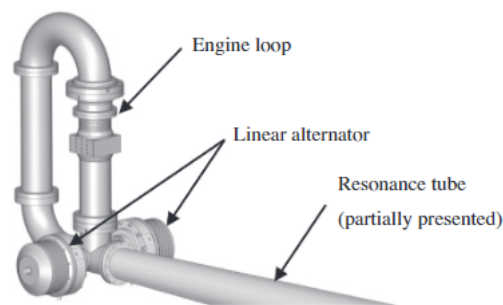
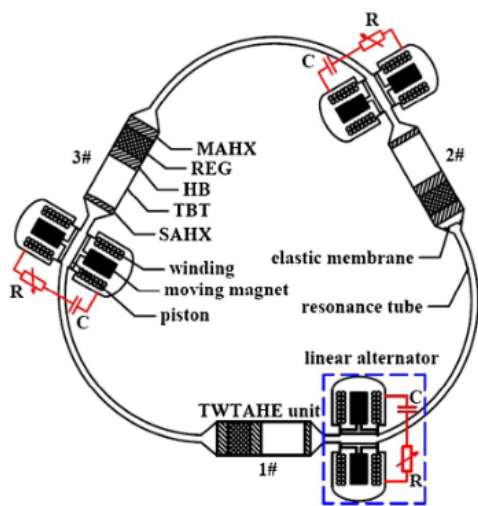


Fig. 1. Schematic of DATASEG.

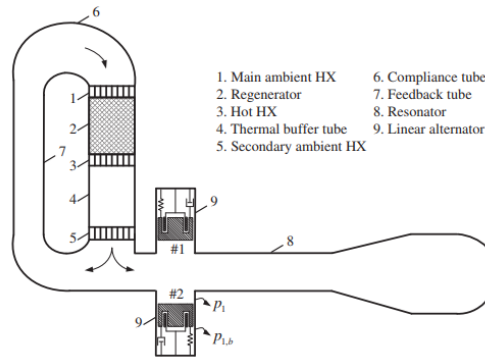
(c) 2014, $\eta = 17\%$, 1570W electric power [39]



(d) 2014, $\eta = 20\%$, 790W electric power [38]

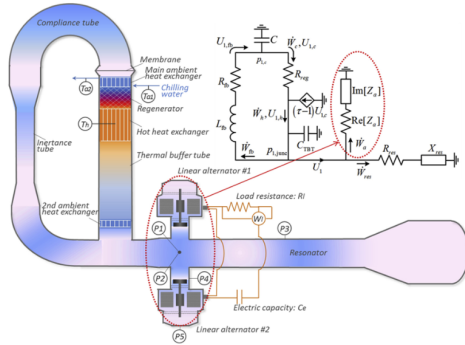


(e) 2015, $\eta = 18.4\%$, 3460W electric power [40]



(f) 2013, $\eta = 12\%$, 321W electric power [41]

Figure 1.10.



(g) 2016, $\eta = 16\%$, 750W electric power [42]

Figure 1.10. Diagrams of experimental setups for various thermoacoustic engines utilizing linear alternators for energy extraction. The efficiencies cited refer to thermal-to-electric efficiency. The electric powers cited refer to electric power produced at peak efficiency, although many of these experiments demonstrated larger maximum power outputs at lower efficiencies. All experiments shown used helium as the working fluid.

To conclude the review of energy extraction, all the experimental results discussed have been summarized in table 1.1.

Table 1.1.: Summary of Previous Experimental Energy Extraction Methods

Method	Author	Engine Type	$P_{in}(W)$	$P_{elec}(W)$	$f(Hz)$	$P_{bulk}(MPa)$	Fluid	η
piezoelectrics	Smoker et al. [25]	standing wave	1.32E-03	1.28E-3	388	0.1	air	9.70% thermal-to-elec.
Bi-Directional Turbine	de Blok et al. [30]	standing-wave	3	N/A	20	0.1	air	31% acoustic-to-rot.
	de Blok et al. [30]	traveling-wave	100000	N/A	16	1	air	76% acoustic-to-rot.
Linear Alternator	Wu et al. [36]	traveling-wave	3001	451	74	3.54	He	15.03% thermal-to-elec.
	Wu et al. [37]	traveling-wave	3200	481	74	3.5	He	15.03% thermal-to-elec.
	Wu et al. [39]	traveling-wave	9345	1570	86	5	He	16.80% thermal-to-elec.
	Wu et al. [38]	traveling-wave	4899	970	64	4	He	19.80% thermal-to-elec.
	Bi et al [40]	traveling-wave	18804	3460	70	6	He	18.40% thermal-to-elec.
	Sun et al. [41]	traveling-wave	2612	322	65	3	He	12.33% thermal-to-elec.
	Wang et al. [42]	traveling-wave	4601	750	65.5	3.16	He	16.30% thermal-to-elec.

1.2.4 Previous Work with R-218

While the vast majority of experiments presented in this literature review thus far have used helium as a working fluid in TAEs, the work presented in this thesis will use the refrigerant octafluoropropane (R-218) as the working fluid, operating in its transcritical region. In 2018, Alexander et al. [2] was the first study to utilize transcritical fluids for thermoacoustic exploitation. They conducted a numerical and experimental investigation on a standing-wave thermoacoustic device with R-218 as the working fluid. Transcritical fluids offer a unique research opportunity because fluids undergo dramatic property changes when they cross the critical region. Thus, a fluid held near its critical pressure, with a temperature gradient that crossed its critical temperature, would undergo large density and therefore pressure fluctuations. Additionally, fluids experience a sharp increase in specific heat capacity when crossing the critical region, allowing for more heat absorption in the stack. The plots for density, ρ , and specific heat at constant pressure, C_p , are shown in Figure 1.11. Additionally, the critical pressure (P_{cr}) and critical temperature (T_{cr}) for R-218 are given in Table 1.2. As bulk pressure in relation to the critical pressure will be a key parameter in this thesis, it will be reported as the ratio of bulk pressure to critical pressure, P/P_{cr} .

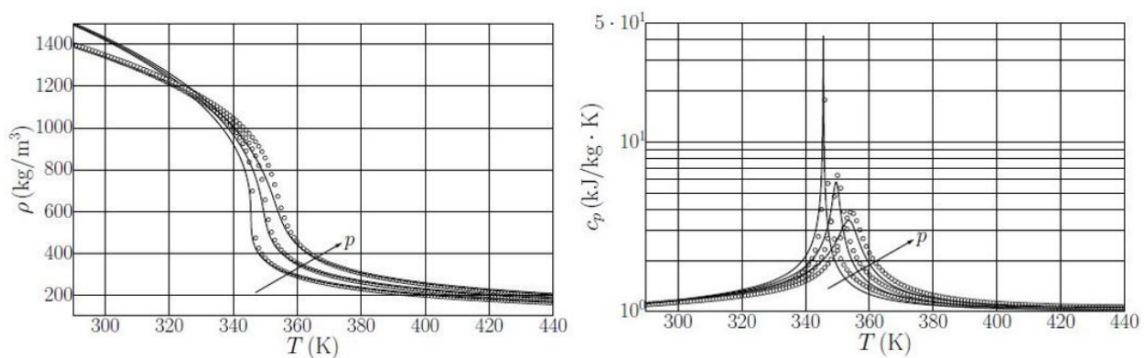


Figure 1.11. Plots showing density (left) and specific heat (right) of R-218 in its transcritical region, from Alexander et al. [2].

Table 1.2.: Critical Conditions for R-218

Critical Temperature (T_{cr})	345.02 K
Critical Pressure (P_{cr})	2.640 MPa

A range of working fluids to test in the transcritical region was considered by the team at Purdue. R-218 was identified as a viable working fluid by Steve Hunt, and the decision was made to test with this fluid because R-218 has a critical temperature and pressure feasible for testing in a laboratory setting. However, using this fluid comes with tradeoffs in its material properties. When comparing R-218 to helium, R-218 will have a much smaller thermal penetration depth. In their Nature publication, Backhaus and Swift cite an average thermal penetration depth of $300\mu m$ [19] with helium, and Alexander et al. cite an average thermal penetration depth of $13.7\mu m$ with R-218. In their work, and in this work, a stack porosity that matched the thermal penetration depth for R-218 was not achieved due to manufacturing constraints, as the smallest pore diameter was $210\mu m$ [4]. This would lead to a reduction in thermal-to-acoustic efficiency. However, acoustic power output is proportional to coefficient of thermal expansion, α_p , and R-218 has a significantly higher coefficient of thermal expansion compared to helium. At the operating temperatures of Backhaus and Swift, coefficient of thermal expansion peaks at $.0021\ 1/k$. At operating conditions about its critical point, R-218 achieves a thermal expansion coefficient nearly two orders of magnitude higher than helium (see Figure 1.12).

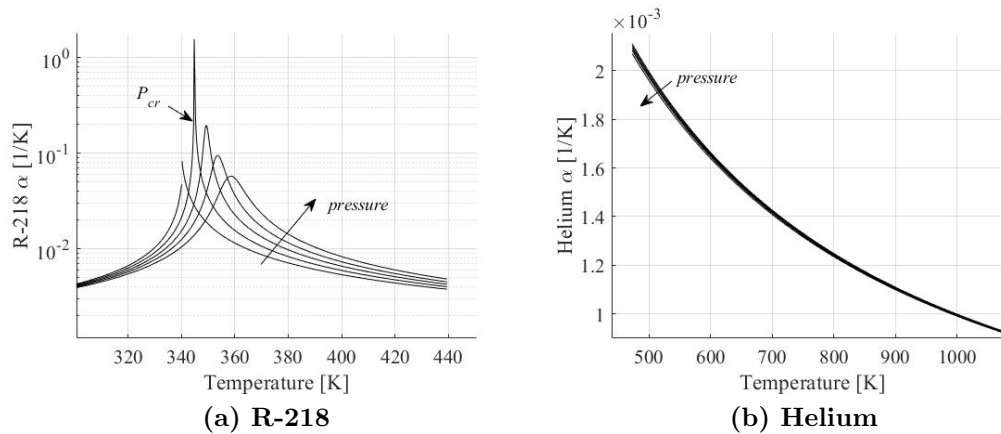


Figure 1.12. Plots showing Coefficient of thermal expansion for R-218 at pressures varying about the critical point (2.37-3.49 MPa) and helium for pressures ranging from 0.69-6.89 MPa and the operating temperature range cited in Backhaus and Swift.

The numbers in Figure 1.12 were computed by Equation 1.5 [2] with values from Nist Chemistry Webbook.

$$\alpha_p = -\left(\frac{1}{\rho}\right) \frac{\partial \rho}{\partial T} \quad (1.5)$$

Thus, it could be hypothesized that a TAE using R-218 could achieve a significantly higher acoustic power output with a potential reduction in thermal-to-acoustic efficiency when compared to an equivalent system with helium. However, when comparing the two fluids for energy extraction, R-218 offers further benefits because of its significantly higher density. In Section 1.2.3, it was shown that rotor efficiency increases with increasing density for bi-directional turbines. Additionally, a denser fluid will provide a higher total impulse in one cycle, at the expense of a lower frequency. This makes R-218 more ideal for linear alternators as well, due to the inertia required to move a piston, combined with frictional forces associated with pistons. In piezoelectric systems, helium is likely to be better-suited because piezoelectrics are capable of responding to extremely small pressure fluctuations, and thus the higher frequency and lower pressure amplitude of helium would act as a benefit.

Alexander et al. constructed a simple standing-wave device which consisted of a resonator, a stack, and a cartridge heater to provide thermal input. The resonator was pressurized by a bladder accumulator, which had a flexible membrane attached to nitrogen supply on one side of the bladder, and a feedline leading to the resonator on the other side of the bladder. The device did not include a hot side cavity or a cooling source, and it was assumed that natural convection from the air would provide a temperature gradient along the stack. A schematic of their rig is shown in Figure 1.13

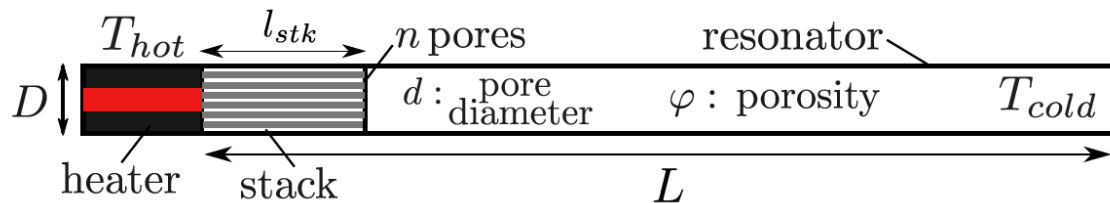


Figure 1.13. Schematic of rig constructed and modeled in work by Alexander et al. [2].

With this configuration, three different stacks with varying porosities were tested. The first stack (Figure 1.14a) was a 3-D printed Inconel stack, containing hollow parallel channels as its pores. This stack had a pore diameter of $580 \mu m$ and porosity of 24.7%. The second stack (Figure 1.14b) was a stainless steel microtube bundle, providing an average pore diameter of $210 \mu m$ and porosity of 57.2%. The final stack (Figure 1.14c) was a graphite foam, with an average pore diameter of $810 \mu m$ and a porosity of 55.3%. Each stack had the same length of 10 cm and diameter of 2.4 cm.

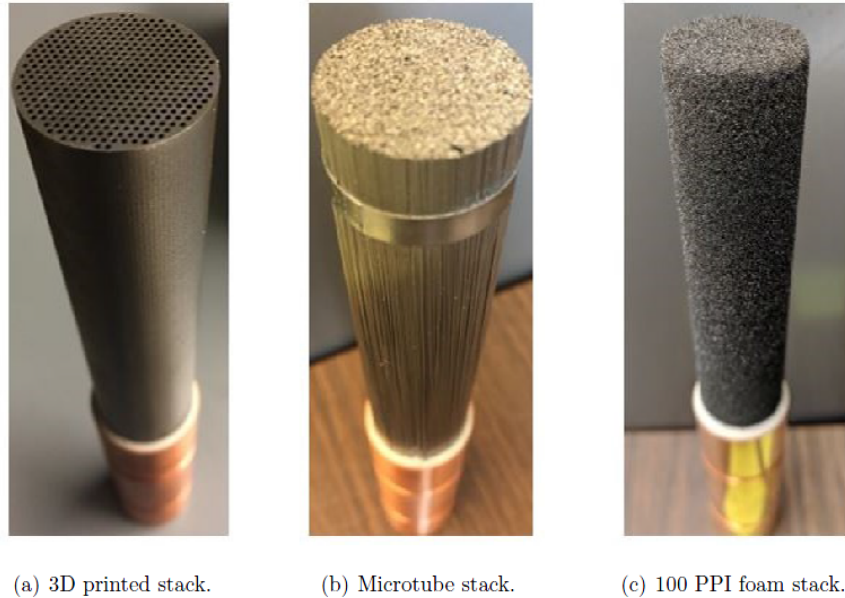


Figure 1.14. Stacks used in experimentation from Alexander [4].

Of these stacks, only the microtube stack was able to produce a thermoacoustic response because of its small pore diameter. From there, the effect of resonator length and bulk pressure were tested. It was found that the length of the resonator (except for slight changes in frequency) had little effect on the response. However, if the feedline was too long, the wave would attenuate due to losses in the line. Trends in the pressure amplitude as a function of bulk pressure were inconclusive because of hardware degradation, but the highest pressure amplitude reported occurred at bulk pressure of $1.02 P/P_{cr}$ (2.7 MPa), yielding a pressure amplitude of 5.3 kPa and a frequency of 4.8 Hz. The findings of this research is what has inspired the team at Purdue to continue and expand upon testing with this fluid, with improvements that will be detailed in Chapter 2.

1.2.5 Linear Stability and Navier-Stokes Models

Migliorino and Scalo constructed fully compressible Navier-Stokes simulations of a thermoacoustically unstable transcritical fluid inside a duct with a stack. This was

compared to a linear stability model and shown to be in good agreement. This model was published in [44] with CO_2 applied as the working fluid. For this research, this same linear stability model was used with R-218 applied as the working fluid, and the results were used to size hardware as well as compare to experimental results. A summary of the key points of the models is given in this section.

The model setup is shown in Figure 1.15.

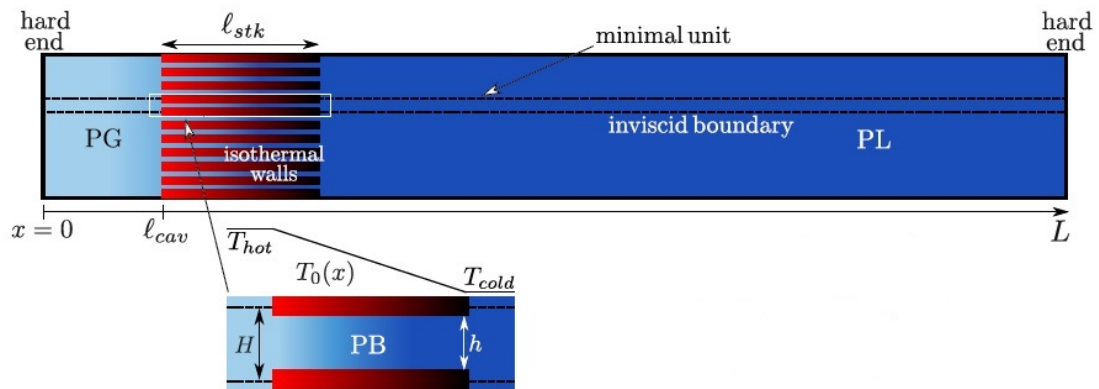


Figure 1.15. Computational modeling setup of Migliorino and Scalo [44].

The Navier-Stokes equations detailed in [44] were applied to the setup of Figure 1.15 to obtain predictions for optimal hot side cavity length, l_{cav} , stack length, l_{stk} , and resonator length, L (Figure 1.16). Optimal geometries were selected to be geometry that resulted in the largest growth rate, α . ΔT is defined as $T_{hot} - T_{cold}$ where T_{hot} occurs at $x = l_{cav}$ and T_{cold} occurs at $x = l_{cav} + l_{stk}$.

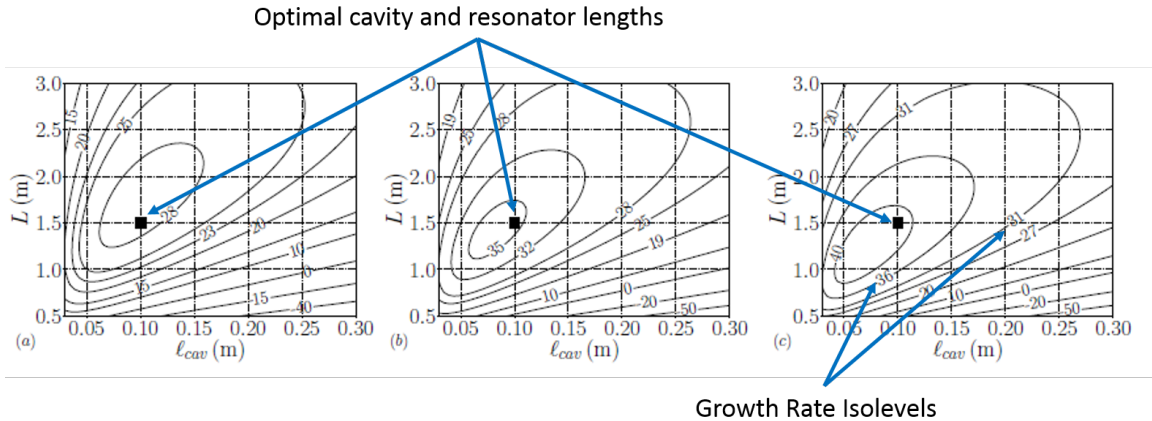


Figure 1.16. Modeling results of Migliorino and Scalo showing optimal geometry based on growth rate Isolevels for various temperature differences. These results apply to CO_2 as the working fluid, with a bulk pressure of 10 MPa, $\Delta T = 100K$ (a), $\Delta T = 125K$ (b), and $\Delta T = 150K$ (c).

For a given geometry, the linear stability model and the Navier-Stokes model have the capability to predict frequency, f , and growth rate as a function of ΔT and bulk pressure.

Behavior of pressure and flow rate were modeled axially (Figure 1.17). At each wall ($x = 0$ and $x = L$), the boundary condition of zero mass flow rate is set. Thus, the maximum pressure occurs at the wall and the minimum pressure occurs in the resonator. Conversely, minimum mass flow rate occurs at the walls and maximum mass flow rate occurs in the resonator. Pressure amplitude and mass flow rate cannot be explicitly computed from modeling, but behavior can be predicted. Figure 1.17 shows the non-dimensionalized pressure amplitude, $|\hat{p}|/|\hat{p}|_{max}$, and non-dimensionalized mass flow rate, $\rho_0|\hat{U}|/(\rho_0|\hat{U}|)_{max}$, where $|\hat{U}|$ is the volumetric flow rate and ρ_0 is the fluid density.

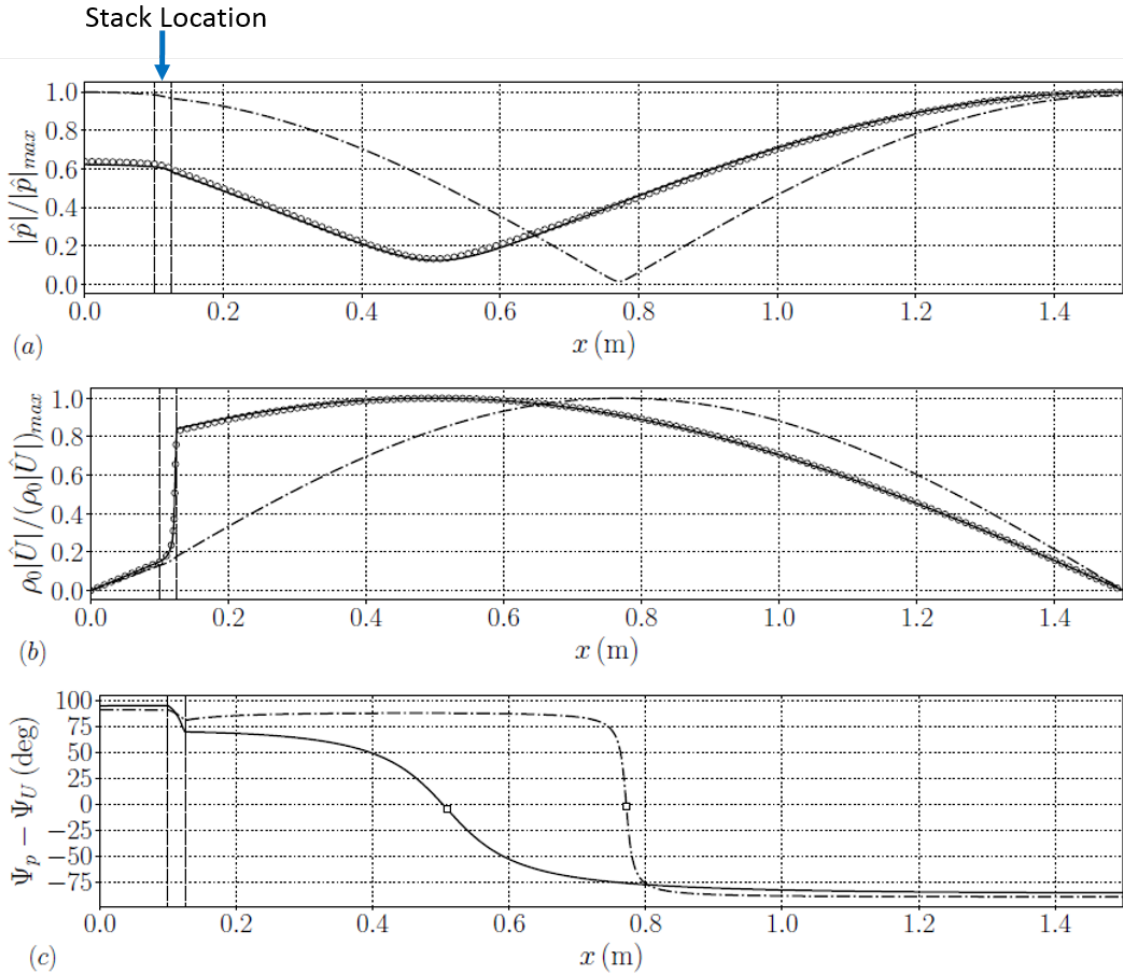


Figure 1.17. Axial Distribution of Pressure (a), mass flow rate (b), and phasing (c) computed from predictive models by Migliorino and Scalo. The solid line shows linear stability model results and circles show Navier-Stokes model results.

From axial pressure and volumetric flow rate, predicted acoustic power at an axial location, $\overline{\dot{W}}(x)$, can be computed by Equation 1.6.

$$\overline{\dot{W}}(x) = \frac{1}{2} \Re\{\hat{p}(x)\hat{U}(x)^*\} \quad (1.6)$$

The acoustic power output is the power produced by the stack, \dot{W}_{stk} , which is given by Equation 1.7.

$$\overline{\dot{W}}_{stk} = \overline{\dot{W}}(l_{cav}) - \overline{\dot{W}}(l_{cav} + l_{stk}) \quad (1.7)$$

The acoustic power is proportional to the square of the pressure amplitude, meaning that there is a constant, K , where:

$$\dot{W}_{stk} = K|P|_{max}^2 \quad (1.8)$$

This constant can be solved for with the linear stability analysis for a given bulk pressure, ΔT , and internal geometry. K can then be applied to an experimentally determined pressure amplitude to solve for experimentally determined acoustic power output, \dot{W}_{exp} , by:

$$\dot{W}_{exp} = K|P|_{max,exp}^2 \quad (1.9)$$

With no losses in the model, the growth rate remains constant and the pressure amplitude continues to grow exponentially. In the real system, losses eventually reduce the growth rate to zero and the pressure amplitude reaches a limit cycle. Migliorino and Scalo were able to predict limit cycle amplitudes by incorporating a nonlinear dissipation term into the model. The source of losses came from vortex shedding due to area change, and coils in the resonator section.

This concludes the introduction for which the experimental test campaign was based. The research detailed in this thesis focuses on exploiting the thermoacoustic effect utilizing R-218 in its transcritical region. The goal of this research is to fully characterize the thermoacoustic response of R-218 and assess its feasibility for energy extraction and waste heat removal. A modular test article has been constructed and tested at the Combustion Lab of Purdue University's Maurice J. Zucrow Laboratories. The design for this test article was based on the predictive model provided by Dr. Mario Tindaro Migliorino, and experimental data will be used to validate this predictive model.

2. EXPERIMENTAL FACILITY

A test article was designed, fabricated, and tested at Zucrow Labs to characterize the thermoacoustic response of R-218 in its transcritical region under several different operating conditions. This chapter will outline the design, construction, and analysis of the test article, instrumentation, and supporting hardware used for this test campaign. First, the experimental objectives will be stated, followed by a description of the hardware. Then, the preliminary analyses of the test article and an uncertainty analysis of the instrumentation will be presented.

2.1 Experimental Objectives

The objective of this test campaign was to explore the feasibility of utilizing transcritical R-218 for energy extraction and waste heat removal. This was achieved by first characterizing the waveform with the goal of maximizing limit-cycle amplitude in order to design an energy extraction device and/or recirculation system. This was of interest to Rolls-Royce as a means to remove waste heat produced in aircraft engines. Several lessons learned from the work of Alexander, whose experimental setup will be referred to as the "Gen. 1 Rig", provided the core driving forces in the design decisions for this test campaign. First, it was determined that microtubes exhibited the best performance and posed the best option as a stack. It was also clear from previous work that both a heating source and a cooling source was necessary to provide an adequate temperature gradient along the stack. It was also determined that the rig needed to have a large reservoir with a hard wall. The reason for this was that closing off heated refrigerant in a small volume led to over-pressurization, while opening the rig to a flexible membrane led to absorption of acoustic energy and therefore attenuation of the wave. Finally, higher-accuracy pressure measurements

were desired for characterization of the waveform [4]. Further requirements were derived from the following desired test objectives:

1. Characterize the waveform by taking pressure measurements along the resonator
2. Characterize the temperature gradient along the stack by taking temperature measurements
3. Determine power input and power output to determine system efficiency
 - (a) Provide capability to measure mass flow rate of heating and cooling fluids
 - (b) Provide capability to measure temperature drop across the stack
4. Test the effect of temperature difference, ΔT_{HC} , between the hot and cold side on the waveform
5. Test the effect of bulk pressure on waveform
6. Test the effect of resonator length on waveform
7. Assess energy Extraction capabilities
8. Have the capability to interface system with energy extraction device

Finally, requirements for the internal geometry needed to be decided. For consistent comparison, it was decided that the internal diameters of the rig would be the same as the system designed by Alexander [4]. Thus, the rig would have several sections to mimic the main resonator section, the feedline, and the bladder accumulator. Additionally, it would have a hot side cavity to improve performance. With the internal diameters fixed, the lengths of each section were designed to optimize the growth rate. Optimal lengths were predicted by the linear stability model [44] constructed by Dr. Mario Tindaro Migliorino for this project.

2.2 Test Article Design

All design decisions were made based on the experimental objectives listed above. The following sections will detail the rig design.

2.2.1 System Overview

The system consists of the following components: Hot side cavity, stack, hot side heat exchanger, cold side heat exchanger, recirculation line, and three resonator sections of varying length and diameter. They are configured as shown in Figure 2.1.

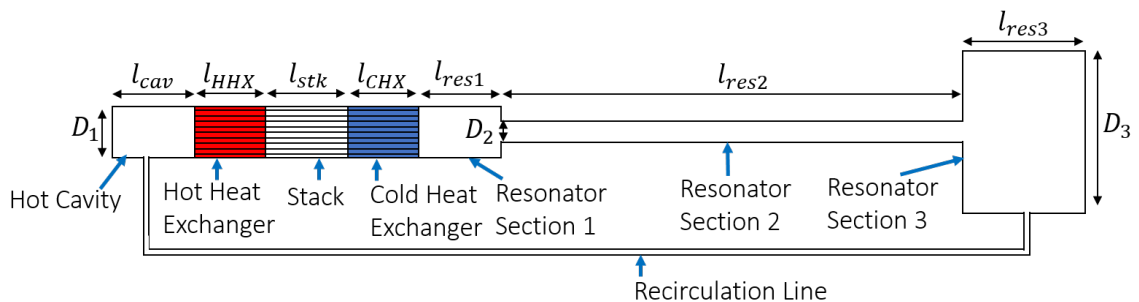


Figure 2.1. Diagram of major components in thermoacoustic device.

Table 2.1 gives the diameter of each major component and the length predicted by the linear stability model. Resonator Section 1 mimics the Gen. 1 resonator, resonator section 2 mimics the Gen 1. feedline, and Resonator Section 3 mimics the bladder accumulator.

Table 2.1.: Major Rig Dimensions

Component	Length (cm)	Diameter (cm)
Hot Cavity	5.080	2.352
HHX	2.030	2.352
stack	6.100	2.352
CHX	2.030	2.352
Res 1	5.080	2.352
Res 2	203.2	.4572
Res 3	15.24	10.67

From these baseline dimensions, the rig shown in Figure 2.2 was designed using computer-aided design (CAD).

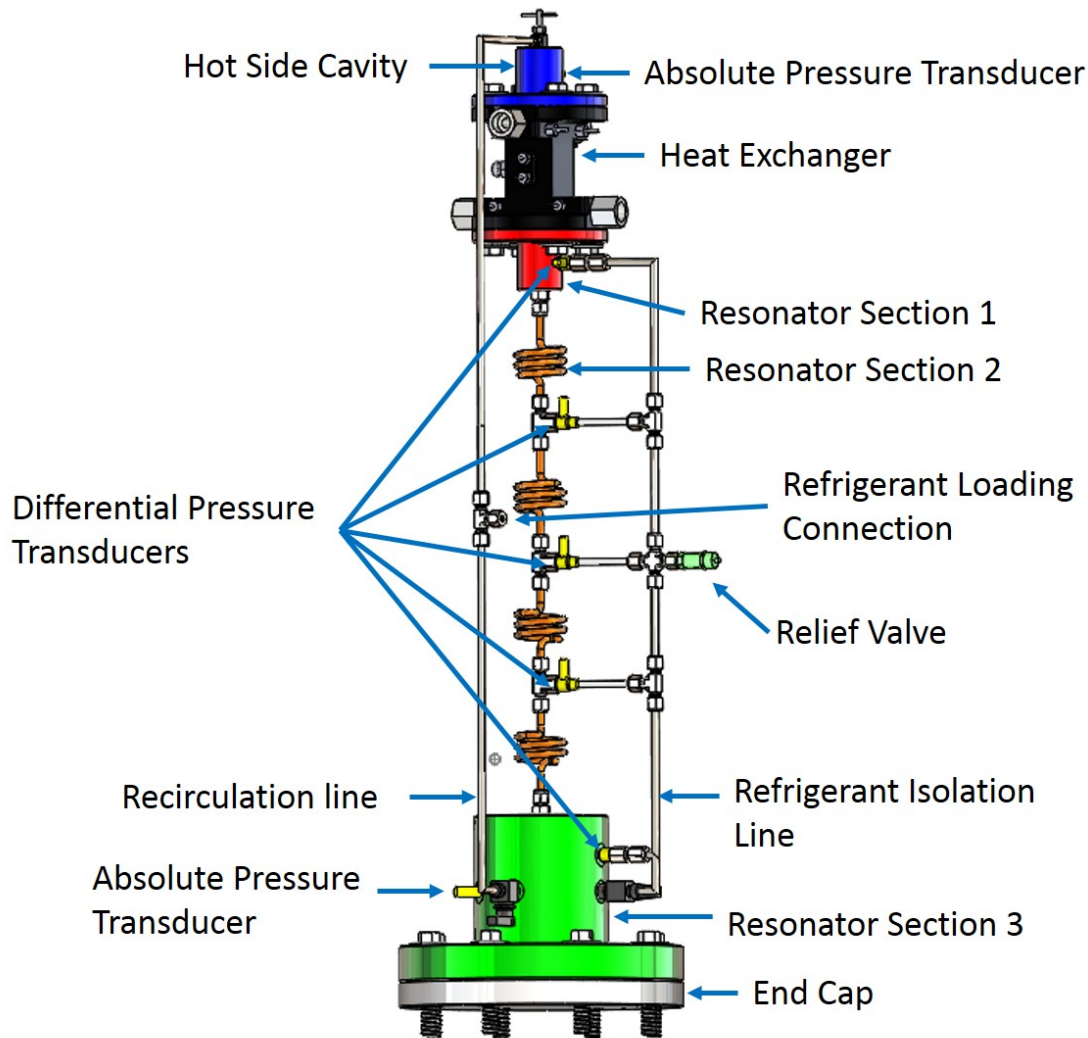


Figure 2.2. CAD of Test Article.

In addition to the major components outlined in Figure 2.1, the rig has a differential pressure transducer system to measure amplitudes down the resonator with high accuracy, two absolute transducers to measure bulk pressure, and relief valves to prevent overpressurization. Each component of the test article will be described in detail in the subsequent sections.

2.2.2 Instrumentation

To measure the temperature gradient in the stack, as well as the inlet and outlet heating and cooling fluids, Omega type-K thermocouples (GKMQSS-062G-6) were placed at strategic locations in the stack (discussed in Section 2.2.3). To measure pressure, there are five Unik 5000 300 psid differential pressure transducers used along the resonator (PMP50E6-TD-A3-CA-H0-PG, 0 to 300 psid, w/w).

Because these are differential pressure transducers, a portion of the refrigerant in the rig is re-routed to one side of the transducers, and that portion of refrigerant is closed off with a valve once the rig reaches the desired bulk pressure. This way, one side of the differential pressure transducer has the bulk pressure with no oscillations, and the other side can measure the fluctuation in pressure solely from thermoacoustic response. The differential transducers were predicted and confirmed from the uncertainty analysis (Section 2.3.6) to give higher resolution in measuring the thermoacoustic response than using absolute transducers.

Differential pressure measurements are taken in resonator section 1 (one transducer), resonator section 2 (three transducers), and resonator section 3 (one transducer). Additionally, one absolute pressure measurement is taken on the test article in the hot side cavity using a Kulite pressure transducer (ETL-GTS-B-190-2000A). A Kulite was selected to go in the hot side cavity because Kulites are capable of withstanding higher temperatures than Unik 5000 transducers, at the expense of having lower accuracy. A second absolute pressure measurement is taken in Resonator Section 3 using a Unik 5000 (PMP50E6-TB-A3-CA-H0-PE-1000PSIA). Temperature measurements are only taken in the heat exchanger as it is assumed that the resonator sections will be at room temperature.

Finally, a Coriolis flow meter was used to measure the mass flow rate for refrigerant in the recirculation line during travelling-wave tests. A Plumbing & Instrumentation diagram (P&ID) is shown below in Figure 2.3, where purple represents refrigerant

pathways, green represents nitrogen pathways, red represents oil pathways, and blue represents water pathways.

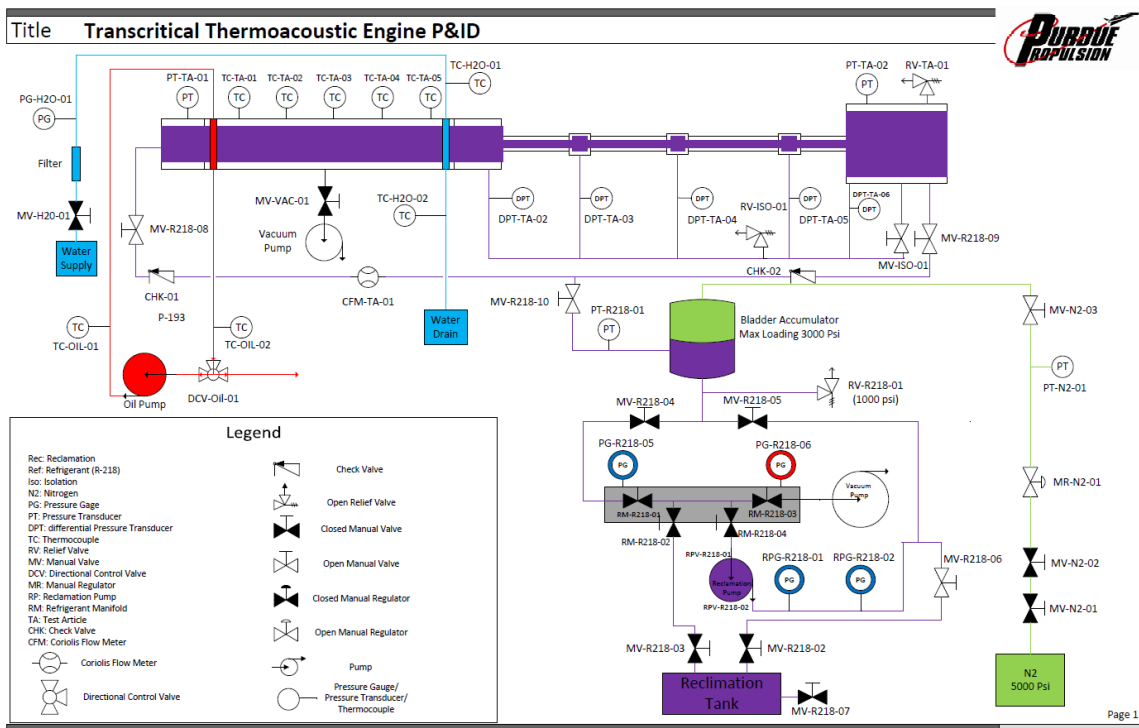


Figure 2.3. Plumbing & Instrumentation Diagram of thermoacoustic test article.

2.2.3 Heat Exchanger

The heat exchanger used for this study was designed in collaboration with and manufactured by Mezzo Technologies, who specialize in microtube heat exchangers. A diagram of the heat exchanger is shown below in Figure 2.4.

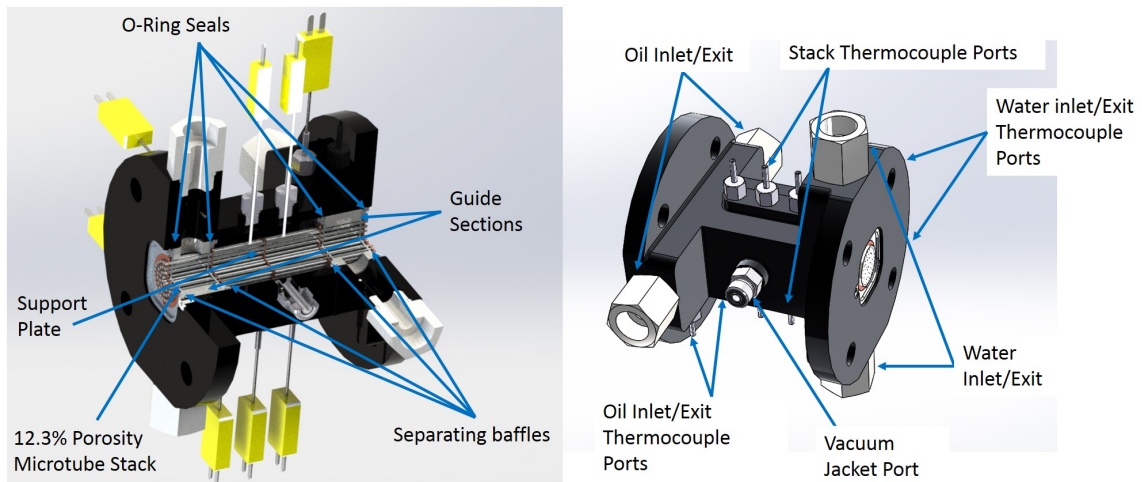


Figure 2.4. CAD Model of heat exchanger used in test campaign, designed with the help of Mezzo Technologies Engineers. Microtube bundle is 12.0 cm long and 2.35 cm in diameter.

The heat exchanger consists of a stack of microtubes aligned in the axial direction inside of an aluminum shell. Refrigerant is allowed to flow axially through the microtubes, while heating and cooling fluid flow radially over the microtubes on either end of the stack. The hot and cold pathways are blocked off by four baffles, which allow for a temperature gradient to form in the region between the hot and cold end. Because a linear temperature gradient maximizes thermoacoustic performance [44], a vacuum port was added. This allows the temperature gradient section of the stack to be insulated with vacuum, eliminating convection around the microtubes and improving linearity of the temperature gradient.

Thermocouples

Five evenly-spaced thermocouples were put in the temperature gradient portion of the stack to measure the temperature gradient. They were placed so that the tip of the thermocouple probe was making contact with the microtube stack, and secured with Swagelok fittings. Additionally, a thermocouple was put at the inlet

and outlet of the hot flow and cold flow so that the energy balance on the system can be computed. The placement of the thermocouples is shown in Figure 2.5.

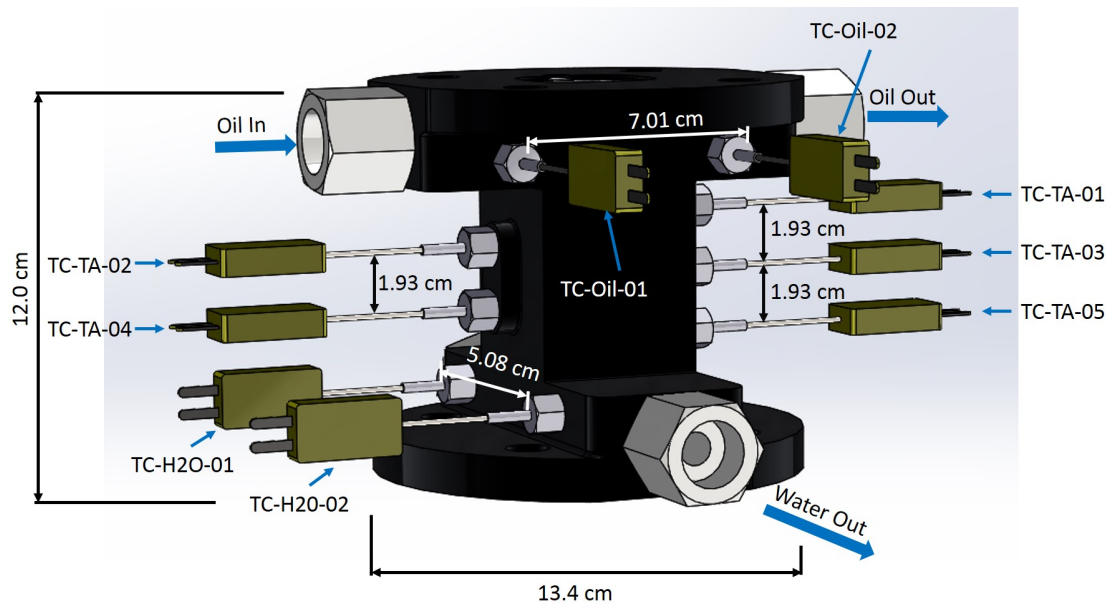


Figure 2.5. CAD Model of heat exchanger showing thermocouple placement

Microtube Stack

The microtubes provided by Mezzo Technologies are stainless steel and have an outer diameter of .3124 mm (.0123”) and an inner diameter of .2108 mm (.0083”). By taking the average thermal penetration depth for R-218 for several points around its critical region, the average thermal penetration depth assuming 5 Hz oscillations is approximately .0355 mm, which means that the ideal inner diameter would be .0709 mm. Since this diameter was not achievable, the design goal was to maximize porosity (given by Equation 1.3) by spacing the tubes as densely as possible. The limiting factor on maximizing porosity was machinability, and the maximum porosity that could be achieved was 12.3%. A scaled visual of the stack is shown below in Figure 2.6.

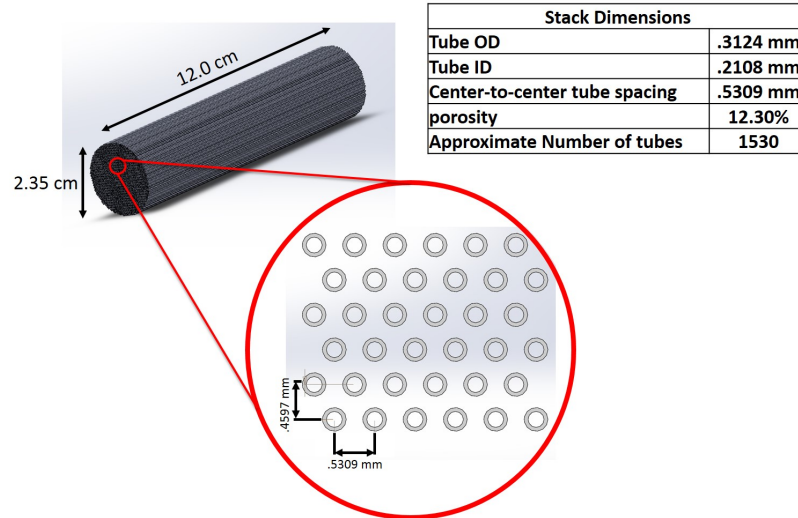


Figure 2.6. Scale CAD of microtube stack showing tube spacing.

The microtubes were secured to the separating baffles by placing epoxy around each microtube. The epoxy is rated to withstand 180°C before being at risk of degradation, and this temperature limit played a role in deciding test conditions for this testing campaign.

2.2.4 Resonator Sections

The Hot Side Cavity, Resonator Section 1, and Resonator Section 3 were all machined out of aluminum by technicians at Zucrow. The completed technical drawings for these parts are documented in A.1-A.4 Resonator Section 2 was constructed out of stainless steel tubing and used Seal Lok fittings to secure it.

Hot Side Cavity

The hot side cavity is bolted to the heat exchanger through an ANSI class 300 flange for 1-1/4 pipe size and is sealed using a 2-228 viton O-ring. It includes an SAE port to attach a manual ball valve (Parker 4F5-4LO-B6L-PKR-LT-SSP). The purpose of the ball valve is to allow a path for fluid loading as well as provide the

capability to operate as either a standing wave or traveling wave system. It also has a straight thread port for the Kulite pressure transducer. The hot side cavity is shown below in Figure 2.7.

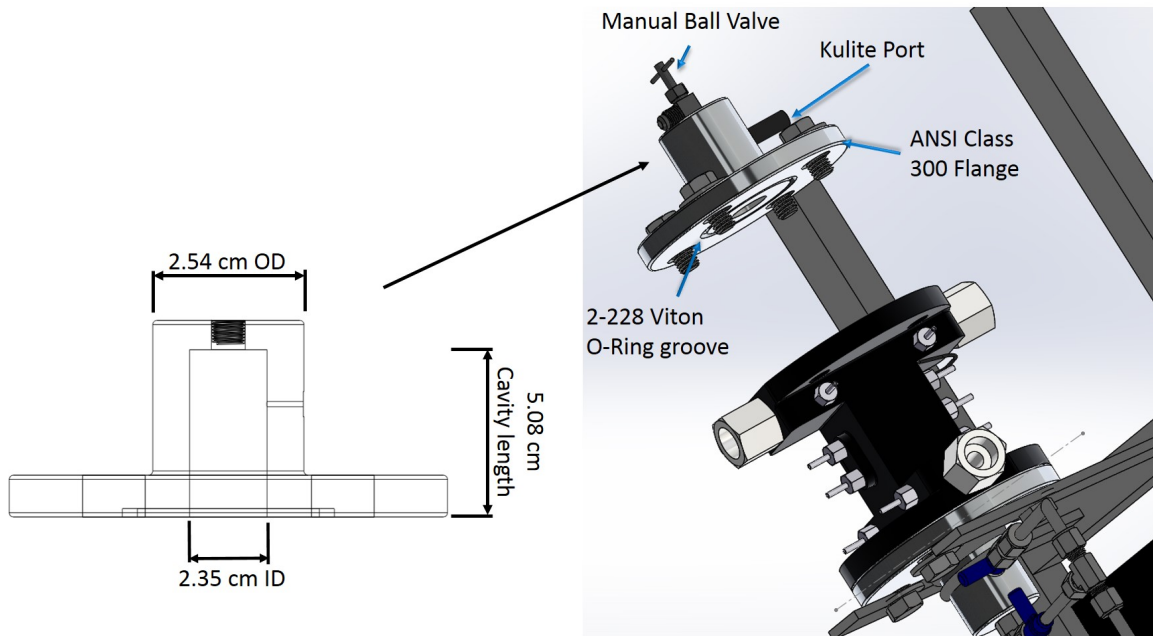


Figure 2.7. Features and dimensions of hot side cavity.

Resonator Section 1

The first resonator section is identical to the hot side cavity in diameter and length, while having different porting features for varied instrumentation. It is a hollow cavity attached to an ANSI class 300 flange for 1-1/4 pipe size. The interface between the heat exchanger and the flange is sealed with a 2-228 viton O-ring. Additionally, the resonator section has a port for direct connection with a differential pressure transducer, as well as a port for connecting to Resonator Section 2 with a Seal Lok fitting. As with the hot side cavity, the wall thicknesses were determined so that instrumentation and fittings would be flush with the inner wall when screwed in. Resonator Section 1 is shown below in Figure 2.8.

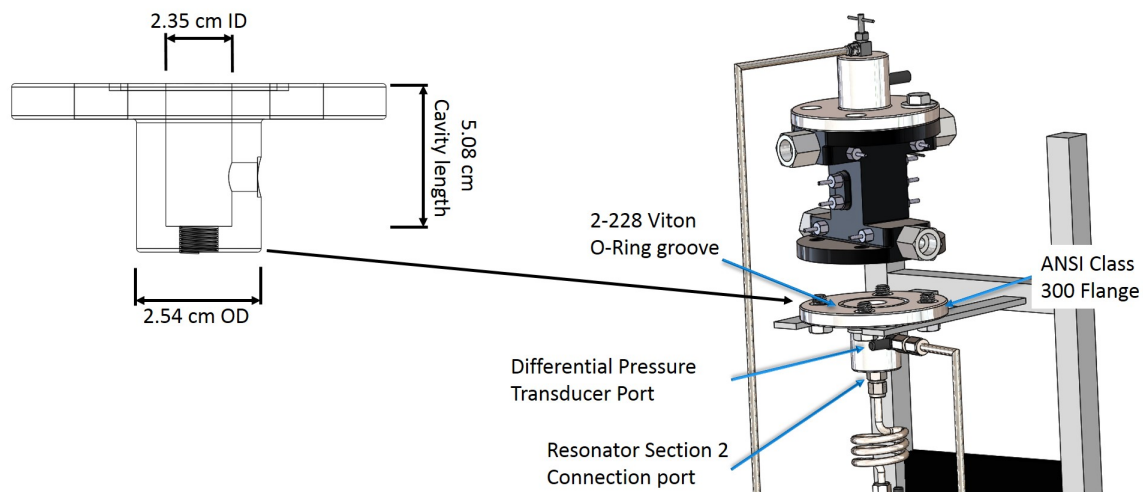


Figure 2.8. Features and Dimensions of Resonator Section 1.

Resonator Section 2

The middle resonator section was constructed out of .25" OD x .035" wall thickness stainless steel tubing. Tubing was divided into four sections to allow for differential pressure transducer readings down the resonator, as well as to allow for varied-length sections.

To read the differential pressure, an isolation line was constructed out of .25" stainless steel tubing with an isolation valve located in the third resonator section. Before heat was introduced to the system at each test, the test article was pressurized to near the desired bulk pressure with the isolation valve open. The isolation valve was then closed to isolate a portion of pressurized refrigerant from the thermoacoustic response.

The pressure transducers were interfaced to the resonator with T-fittings, where one side of the transducer was exposed to the oscillating fluid in the resonator, and the other side was exposed to the static fluid in the isolation line so that pressure amplitudes could be measured. A pressure relief valve (Swagelok SS-4R3A5) with a 5.17 MPa (750 psi) limit was placed in the isolation line in case of overpressurization. Resonator Section 2 is shown below in Figure 2.9.

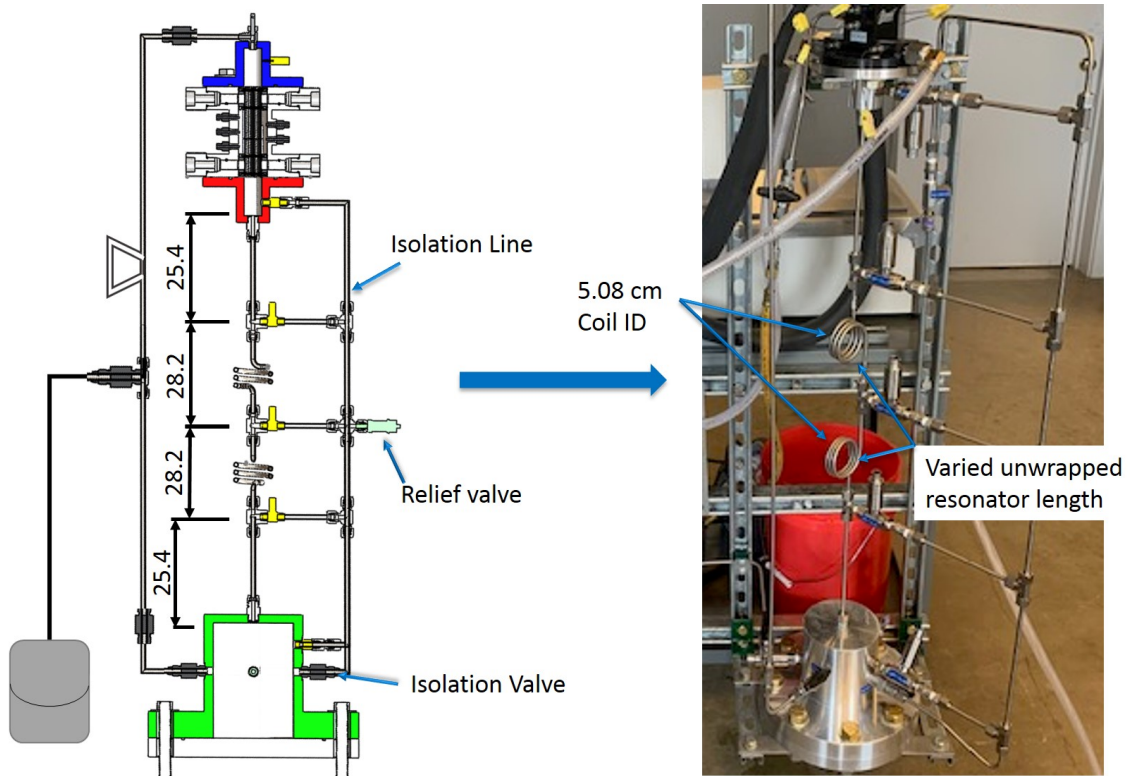


Figure 2.9. CAD image showing features and dimensions of Resonator Section 2 (left) and image of resonator construction showing features and dimensions of Resonator Section 2 (right). Dimensions are in cm.

The resonator sections were coiled around a 5.08 cm diameter rod for compactness, although the coils provide minor losses in thermoacoustic response. These losses were computed by Dr. Migliorino using the methodology detailed in [45] and taken into account in the predictive model.

Resonator Section 3

Resonator Section 3 is bolted to an end cap using a class 300 ANSI flange for 5" pipe. The end cap is made of 2.54 cm thick aluminum. The purpose of the end cap is to be removable to allow for the possibility of an energy extraction device, such as a piston or piezoelectric device, to be interfaced with Resonator Section 3.

The resonator section is sealed with a 2-263 viton O-ring in the end cap. At the top, the resonator section has an SAE port to connect it to Resonator Section 2. On the sides, the resonator section has two ports for ball valves (Parker 4F5-4LO-B6L-PKR-LT-SSP) connecting it to the recirculation line and the isolation line. The resonator section also has a port for an absolute pressure transducer (GE measurement PMP50E6-TB-A3-CA-H0-PE-1000PSIA) and a pressure relief valve (Swagelok SS-4R3A5) with a 5.17 MPa (750 psi) limit. Resonator Section 3 is shown below in Figure 2.10.

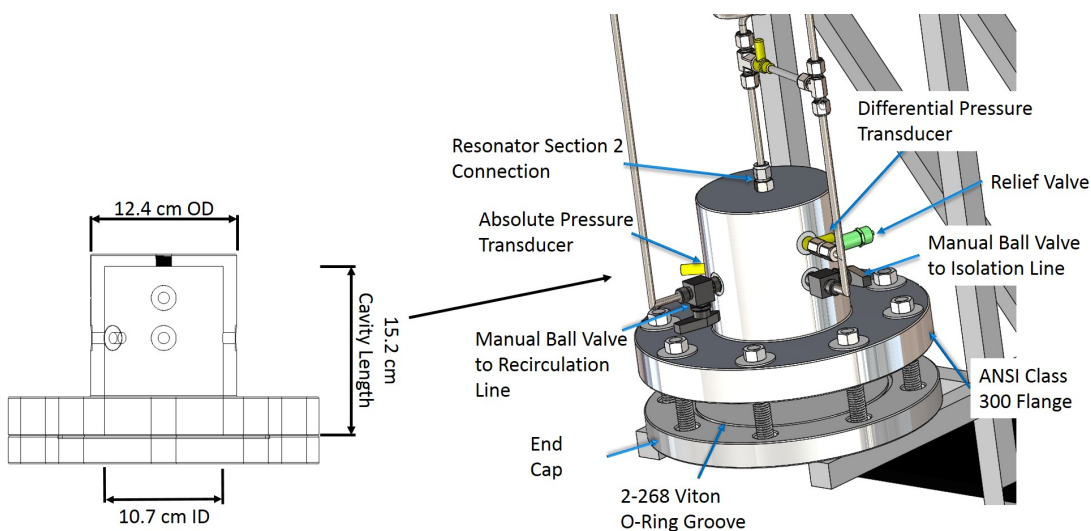


Figure 2.10. Features and Dimensions of Resonator Section 3.

Recirculation Line

The recirculation line was constructed of .25" stainless steel tubing. One end of the line connects to the ball valve on the hot side cavity and the other end connects to the ball valve on Resonator Section 3. A T-fitting was placed along the recirculation line to connect to the bladder accumulator. A manual ball valve (Parker 4LO-B6LJ2-LT-SSP) was connected to the T-fitting to allow the test article to be closed off from the bladder accumulator. Two check valves (Parker 4LO-C4L-1/3-SS) were installed in the recirculation line to force the refrigerant to travel in one direction, creating a

”pump” from the oscillating fluid. The mass flow rate generated from the circulation was measured using a Coriolis Flow Meter (Emmerson CMFS015M323N2BAECZZ). The recirculation line is shown below in Figure 2.11.

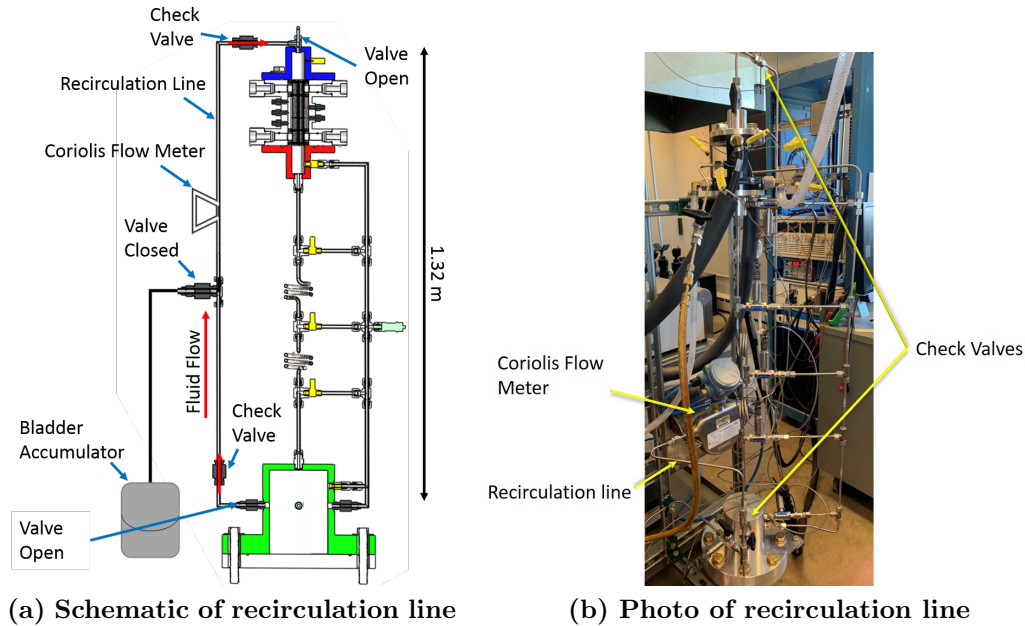


Figure 2.11. Features and dimensions of recirculation line.

2.2.5 Supporting Hardware

The supporting hardware required for testing consisted of equipment needed to flow heating and cooling fluids, refrigerant handling equipment, and a data system to monitor and record pressure and temperature measurements.

Heating Fluid Equipment

Oil was heated and circulated through the heat exchanger using a Thermo Scientific Heated Oil Bath (Thermo Scientific EW-12143-55). Heating on this device is controlled by a microprocessor proportional integral derivative (PID) controller. Circulation is controlled by a force and suction pump [46]. This allowed the oil temperature to be preset for each test, and provided a constant and precise heating fluid

temperature and flow rate. The heating fluid used was Duratherm G heat transfer oil. This fluid was selected because of its low viscosity at higher temperatures (7.6 cSt at 100°C), in an effort to reduce stresses placed on the microtubes. The technical data sheet for Duratherm G is given in A.5. Viton fluorelastomer tubing was used for its compatibility at high temperatures (McMaster Carr 5119K95), and High-Temperature Silicone Foam Insulation was placed around the tubing to reduce heat loss (McMaster Carr 45295K56).

The oil bath has three pump settings to control the mass flow rate (high, medium, and low). The oil mass flow rate was measured using a catch-and-weigh method. This required a three-way directional control valve (McMaster Carr 4467K43) to re-route flow for measurement. The process and results of this are detailed in the Preliminary Analysis (Section 2.3.5). An image of the oil system is shown in Figure 2.12.

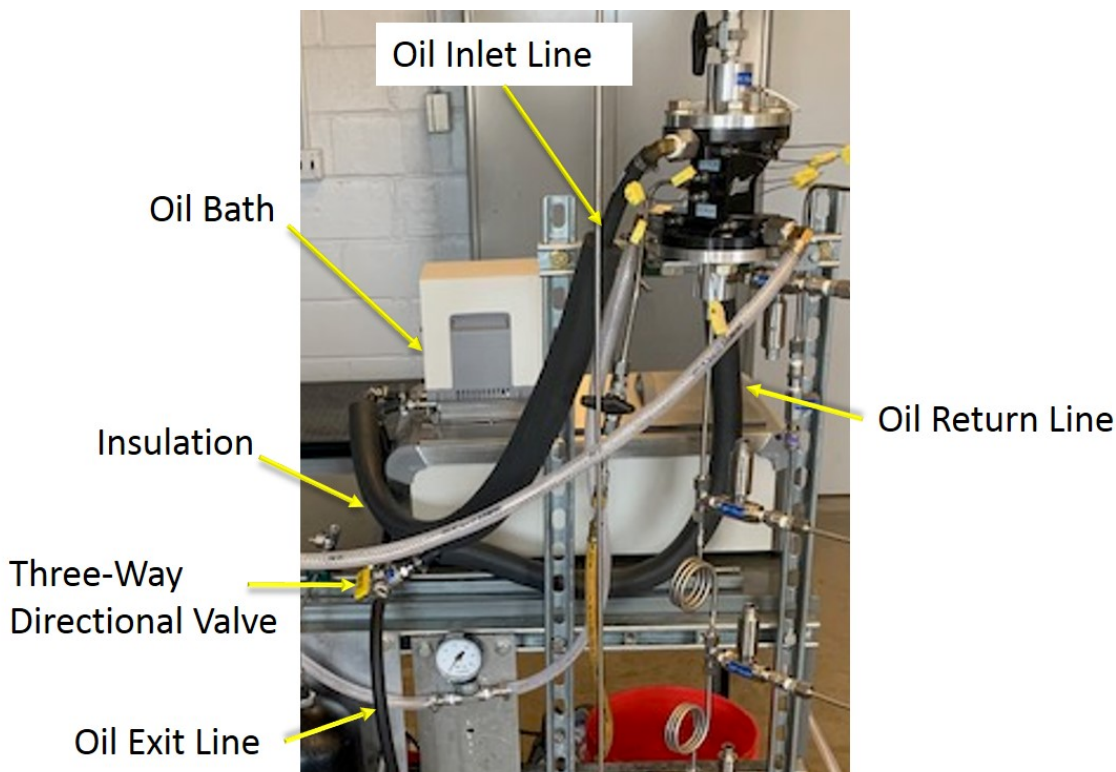


Figure 2.12. Image of Oil Heating and Circulation System.

Cooling Fluid Equipment

The heat exchanger was cooled using chilled tap water from the lab facility. The water was run through a filter (OMNIFilter 20" Heavy-duty Granular Carbon Filter) to reduce particulate buildup in the stack. The water pressure was monitored using a pressure gauge (McMaster Carr 4089K64) upstream of the heat exchanger. The pressure gauge allowed a visual confirmation that water flow rate was being held constant through a test and confirmation that water pressure was not exceeding the limit of the heat exchanger. At the exit of the heat exchanger, the water was routed to a drain where it was expelled. Tygon tubing was used to route the water. The flow rate of the water was controlled by partially opening or closing the water supply manual valve. Before each test series, the volumetric flow rate of water was measured using a catch-and-weigh method, where the water exit line was fed into an Erlenmeyer flask and the amount of time it took the water to fill 2,000 mL was measured with a stopwatch. The desired volumetric flow rate of water for each test was approximately 3.8 L/min (1 GPM), and the rationale for this flow rate will be discussed in the preliminary analysis (Section 2.3). The volumetric flow rate of water was recorded with each test. An image of the water system is shown below in Figure 2.13.

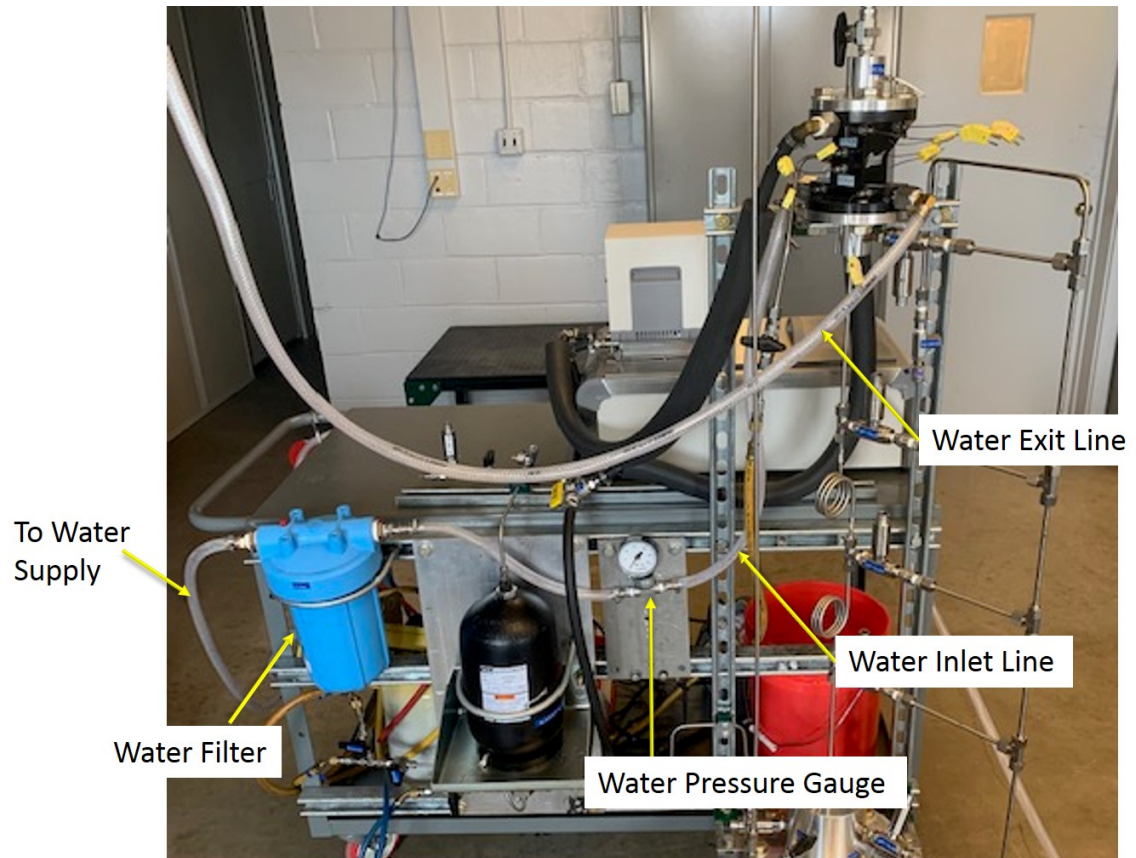


Figure 2.13. Image of Water Cooling System.

Refrigerant Handling System

The refrigerant loading, pressurizing, and storage equipment and operating procedures were inherited from Alexander [4]. The refrigerant is pressurized using a bladder accumulator (Parker 59595K12). The bladder accumulator, shown in Figure 2.14, has a flexible Buna membrane which separates nitrogen from the refrigerant. The nitrogen, which is supplied from the 5,000 psi nitrogen supply source, is pressurized with a manual regulator, and in turn pressurizes the refrigerant in the test article. The accumulator is then closed off from the test article with a manual valve (Parker 4LO-B6LJ2-LT-SSP) before testing so that the accumulator does not absorb acoustic energy produced by the thermoacoustic response. The complete technical drawing for the bladder accumulator is given in A.6.

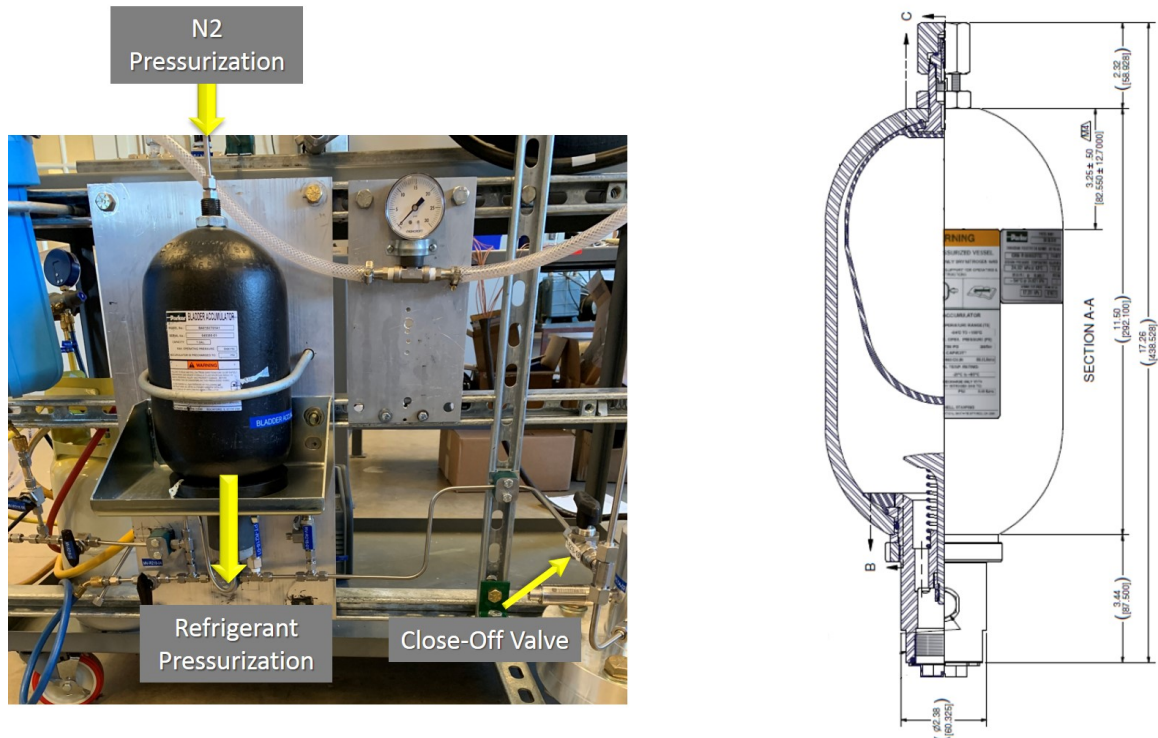


Figure 2.14. Image of Bladder Accumulator (left) and Technical Drawing of Bladder Accumulator showing internal structure (right).

Because R-218 is a greenhouse gas and because it was not available in large quantities, it was necessary to have equipment that could pump the refrigerant from the test article into a storage tank during test article modifications without releasing any fluid. It was also necessary for the fluid to be pumped back into the test article without contaminating the refrigerant. To accomplish this, the fluid is pumped in and out of a refrigerant tank (Robinair 40153) using a reclamation pump (Robinair RG3). A refrigeration manifold (Yellow Jacket 42216), which consists of 4 manual valves, is used to control the direction of refrigerant into or out of the refrigerant tank. To ensure no contamination of the refrigerant with air, the test article and all refrigerant lines are vacuumed using a vacuum pump (Robinair 15150). The refrigerant supporting hardware is shown in Figure 2.15.

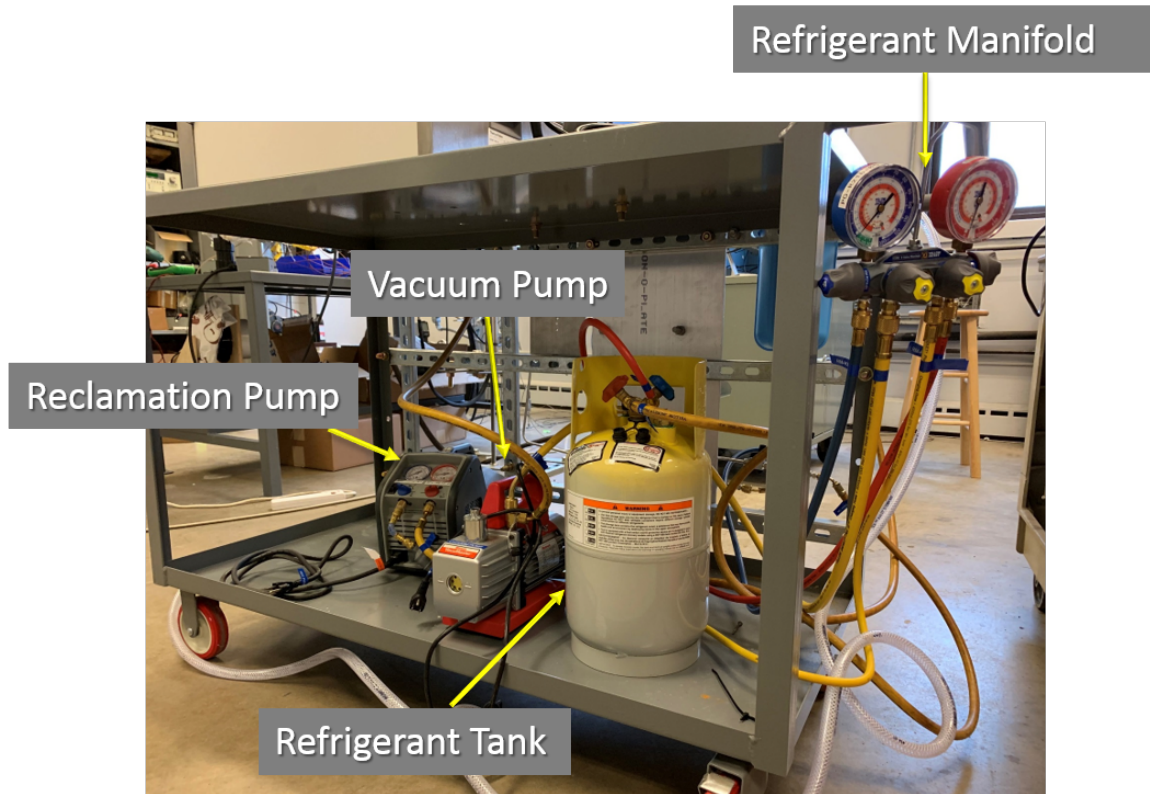


Figure 2.15. Image of supporting hardware used for refrigerant loading, reclaiming, and storage.

The comprehensive procedures for refrigerant loading are given in A.7 in accordance with the P&ID in Figure 2.3.

Data System

Pressure, temperature, and mass flow rate measurements were observed and recorded using an NI Max Data Acquisition System (DAQ). A labview program was developed on the DAQ to control the recording of data. The labview program developed to display and record data is shown in Figure 2.16.

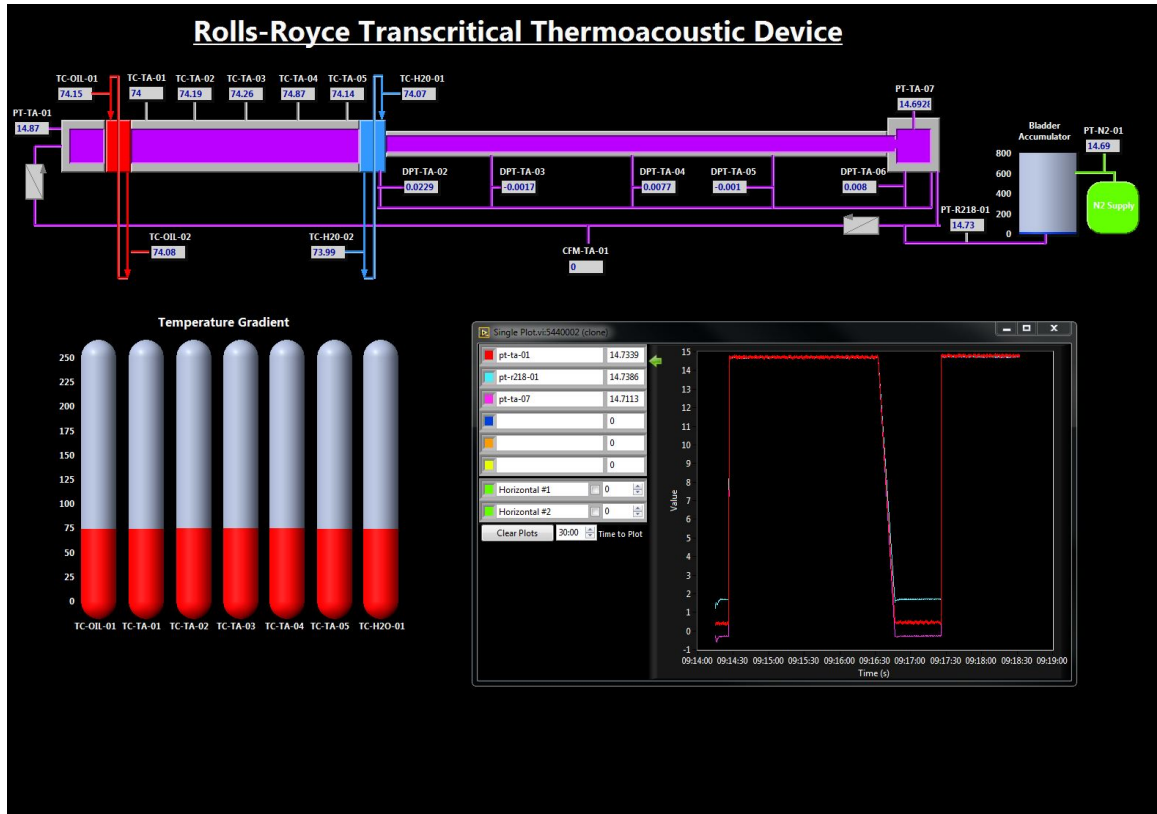


Figure 2.16. Data acquisition system used for monitoring and recording data.

2.3 Preliminary Analysis

Several preliminary Analyses were conducted on the hardware detailed above to ensure that the equipment would operate as expected, as well as to form a better understanding of desired test conditions. First the structural analysis on the hardware will be explained. Then the heat transfer analysis and a structural analysis on the microtubes will be presented, with a conclusion of desired heating and cooling fluid mass flow rates. Finally, an uncertainty analysis on the instrumentation will be presented.

2.3.1 Resonator Structural Analysis

All tubing, valves, and instrumentation exposed to high pressure had pressure ratings significantly higher than the expected operating pressure. Because the resonator sections were designed and fabricated at the lab, it was necessary to conduct a structural analysis on the resonator sections to ensure the wall thicknesses were sufficient to hold the required operating pressures. As previously stated, the wall thicknesses were determined so they would match the length of fittings interfacing with instrumentation, allowing instrumentation to be flush with the inner wall of the resonator sections.

An internal pressure analysis was conducted in ANSYS at 2x the maximum expected operating pressure (MEOP). The MEOP for this experimental campaign is 3.45 MPa (500 psi). The analysis was conducted for Resonator Section 3 with the end plate, and separately for the hot side cavity, heat exchanger, and Resonator Section 1. Because the hot side cavity and Resonator Section 1 have identical diameters and wall thicknesses, the structural analysis is symmetrical. The results of the analysis are shown below in Figures 2.17 and 2.18.

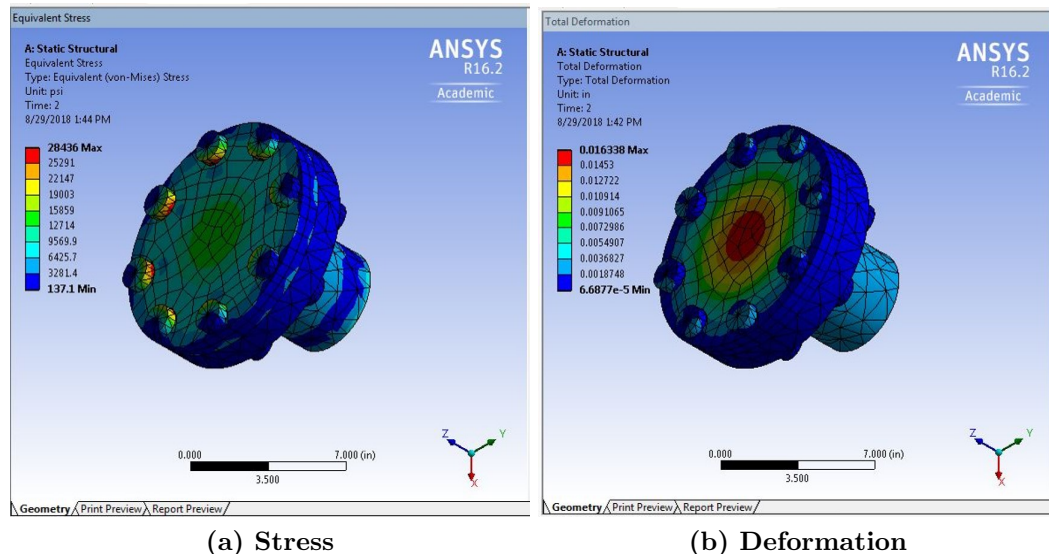


Figure 2.17. Results of ANSYS structural analysis conducted on Resonator Section 3 at 6.9 MPa (1000 psi).

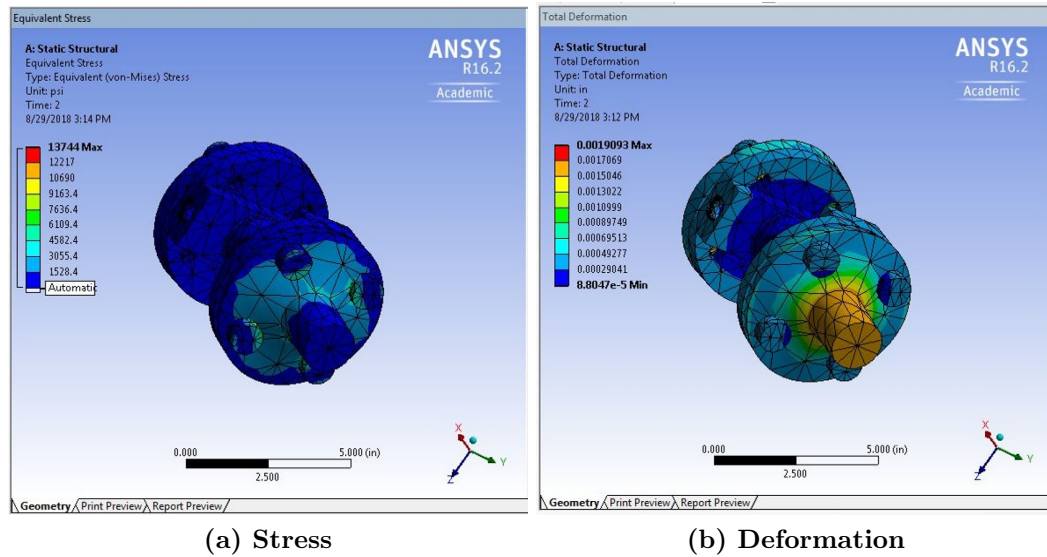


Figure 2.18. Results of ANSYS structural analysis conducted on Resonator Section 1 and Hot Side Cavity at 6.9 MPa (1000 psi).

The tensile strength for aluminum is 279 MPa [47]. At 2X MEOP, the hot side cavity and Resonator Section 1 are expected to see a maximum stress of 42 MPa, which is 15% of the yield strength. In Resonator Section 3, the end plate experiences a maximum stress of 109 MPa, which is 40% of the yield strength. The bolts experience a larger stress of 196 MPa, but the bolts are made of steel and have a yield strength of 1034 MPa (150,000 psi).

Additionally, the maximum deformation on the end plate is .4 mm (.016”), and this is less than the difference in height between the O-ring groove and the O-ring (0.97 mm height difference). This means that the pressure vessel will remain sealed. The same is true for the hot side cavity/Resonator Section 1. They will experience a maximum deformation of .04 mm (.002”), and the difference in height between the O-ring and the O-ring groove is also 0.97 mm.

2.3.2 Heat Transfer Analysis

To estimate the thermal power requirements of the heating and cooling fluids, a preliminary heat transfer analysis was performed in MATLAB for a bank of tubes in

crossflow, with the methodology given by Incropera and DeWitt [48]. In this analysis, the hot heat exchanger and cold heat exchanger are two separate systems analyzed using the same methodology, with the assumption of 1-D flow at steady state and the setup shown in Figure 2.19.

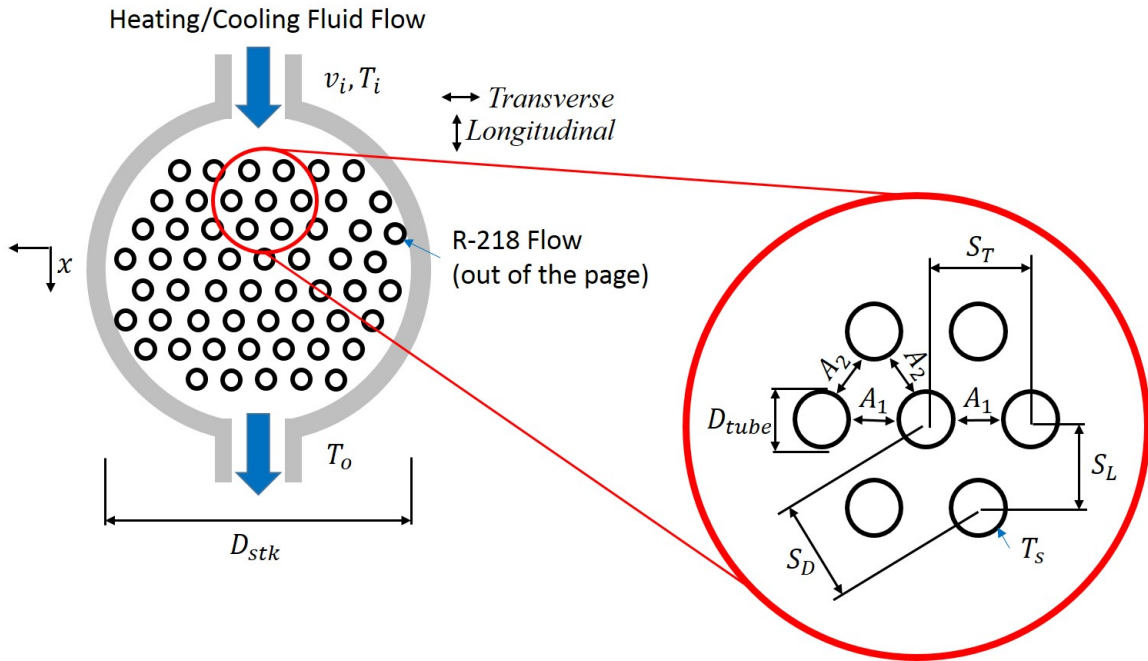


Figure 2.19. Schematic of Heat Transfer Analysis for a bank of tubes in crossflow.

The heat transfer fluid is flowing over a bank of tubes with some initial velocity, v_i , and temperature, T_i . The tubes contain R-218 flowing out of the page. The purpose of this analysis was to determine the required mass flow to provide a given heat transfer in/out of the R-218. The tube geometry is determined by the center-to-center tube spacing, given by the manufacturer to be .5309 mm. It is assumed that the tubes are in a staggered formation and evenly spaced such that $S_T = S_D =$ center-to-center tube spacing. The number of tubes in the stack is estimated by

$$N_{tubes} = \frac{\pi}{4} \left(\frac{D_{stk}}{S_T} \right)^2 \quad (2.1)$$

To begin, a freestream temperature is set and a freestream velocity is guessed, so that the following procedure can be iterated until the desired heat transfer rate is reached. It should be noted that for testing, the cold side temperature will be approximately constant for all tests, but the hot side tests will vary in temperature. This will cause the viscosity of the and therefore the mass flow rate of oil to vary significantly with temperature. For this analysis, a hot side temperature of 392 K was selected, which is near the middle of the range of temperatures we plan to test.

The Reynolds number is based on the maximum velocity, v_{max} , that occurs down the heat exchanger. Depending on the geometry of the tubes, the maximum velocity can occur either in the plane A_1 or A_2 , shown in Figure 2.19. If the rows are spaced such that

$$2(S_D - D_{tube}) > (S_T - D_{tube}) \quad (2.2)$$

Then the maximum velocity will occur at A_1 , otherwise the maximum velocity will occur at A_2 . For equilaterally spaced tubes $S_T = S_D$, so the maximum velocity will always occur in A_1 . The maximum velocity is thus given by:

$$v_{max} = \frac{S_T}{S_T - D_{tube}} v_i \quad (2.3)$$

The Reynolds number is computed using this maximum velocity. Since both heat transfer fluids are liquids, density, ρ , will remain constant at all locations. Because this analysis is done at one temperature, the viscosity, μ , also remains constant, although the viscosity of heat transfer oil will vary significantly with temperature. The Reynolds number at the location of maximum velocity, $Re_{D,max}$, is thus given by:

$$Re_{D,max} = \frac{\rho v_{max} D_{tube}}{\mu} \quad (2.4)$$

Several models to determine the Nusselt number for fluid in crossflow over a bank of tubes is available [48]. The model proposed by Khan et al. [49, 50] was selected

because it was applicable to the range of Prantl numbers, Reynolds numbers, and geometry used in this analysis. The correlation for Nusselt number is given by

$$Nu_D = C_1 Re_D^{1/2} Pr^{1/3} \quad (2.5)$$

where C_1 is obtained for a staggered arrangement by

$$C_1 = \frac{0.61 \mathcal{L}_T^{0.091} \mathcal{L}_L^{0.053}}{1 - 2e^{-1.09 \mathcal{L}_L}} \quad (2.6)$$

where \mathcal{L}_T and \mathcal{L}_L are nondimensionalized geometry parameters, given by

$$\mathcal{L}_T = \frac{S_T}{D_{tube}} \quad (2.7)$$

$$\mathcal{L}_L = \frac{S_L}{D_{tube}} \quad (2.8)$$

Equations 2.5 and 2.6 are valid for laminar flows ($40 < Re_D < 1000$), fluids with $Pr \geq 0.71$, and geometries where $1.05 \leq \mathcal{L}_T \leq 3$ and $1.05 \leq \mathcal{L}_L \leq 3$. The average heat transfer coefficient, \bar{h} , is then calculated by

$$\bar{h} = \frac{k_{th} Nu_D}{D_{tube}} \quad (2.9)$$

where k_{th} is the thermal conductivity of heat transfer fluid. The heat transfer rate, \dot{Q} , is given by

$$\dot{Q} = N_{tubes} \pi D_{tube} L_{HX} \bar{h} \Delta T_{lm} \quad (2.10)$$

where L_{HX} is the length of tube which comes in contact with the heat transfer fluid. $N \pi D_{tube} L_{HX}$ is the total surface area of tubes where heat is transferred. Here, ΔT_{lm} is the log mean temperature difference between the microtube surface and the heat transfer fluid bulk temperature. ΔT_{lm} is given by Equation 2.11.

$$\Delta T_{lm} = \frac{(T_s - T_i) - (T_s - T_o)}{\ln\left(\frac{T_s - T_i}{T_s - T_o}\right)} \quad (2.11)$$

where T_s is the temperature at the microtube wall, and T_o is the outlet fluid temperature. This method for determining the approximate temperature difference in the heat exchanger is employed because the temperature of the heat transfer fluid will vary with location. In Equation 2.11, both T_s and T_o are unknowns. T_s is dependent on conduction along the stack, the thermal penetration, and the thermoacoustic response. This makes an estimation of T_s using analytical methods difficult. However, these equations can be evaluated for a range of wall temperatures which are reasonable. To size the heating and cooling fluid supply, a temperature difference, $|T_i - T_s|$, between 1K and 10K was evaluated. Thus, T_o can be solved for using Equation 2.12.

$$\frac{T_s - T_o}{T_s - T_i} = e^{\frac{-\pi D_{tube} N_{tube} \bar{h}}{\rho v_i N_T S_T C_p}} \quad (2.12)$$

where N_t is the number of tubes in the transverse direction. Additionally, the pressure drop across the tube bundle can be computed by

$$\Delta P = N_L x \left(\frac{\rho v_{max}^2}{2} \right) f_f \quad (2.13)$$

where N_L is the number of tubes in the longitudinal direction, x is the correction factor based on geometry, and f_f is the friction factor based on Reynolds number. Charts for x and f_f based on Reynolds number and geometry are given in [48]. Because the tubes are assumed to have equal spacing, $x = 1$ in this analysis. The friction factor was curve-fitted to each Reynolds number used in this analysis. For Duratherm G and water, the properties given in Table 2.2 and the geometric parameters given in Table 2.3 were used for the heat transfer analysis.

Table 2.2.: Heat Transfer Fluid Properties

	$T_i(k)$	$\rho(kg/m^3)$	$Cp(J/kg * k)$	$\mu(Pa * s)$	$k(W/m * k)$	Pr
Water	287	999	4190	.0017	.587	8.22
Duratherm G	392	897	2062	.00471	.173	56.63

Table 2.3.: Heat Exchanger Geometric Parameters

$D_{tube}(mm)$	$D_{shell}(mm)$	$A_{in}(mm^2)$	$L_{HX}(mm)$	N_{tubes}	N_t	N_L
.31	23.5	126.7	20.3	1542	28	28
$S_T(mm)$	$S_L(mm)$	$S_D(mm)$	\mathcal{L}_T	\mathcal{L}_L	C_1	
.53	.46	.53	1.70	1.47	1.09	

Based on these results, a range of mass flow rates was computed for a heat transfer rate of 350 W, 500 W, and 1000 W. The predicted mass flow rates as a function of $|T_i - T_s|$ is shown in Figure 2.20.

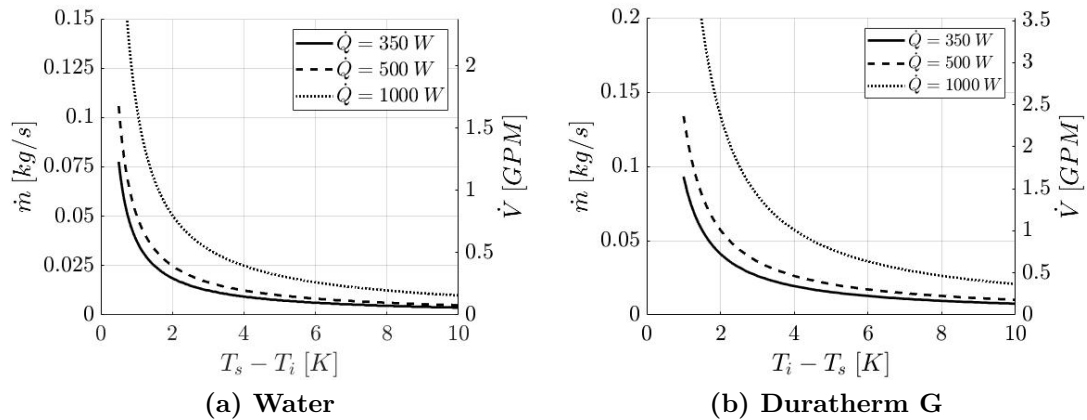


Figure 2.20. Heating and cooling fluid predicted mass and volumetric flow rate requirements as a function of $|T_i - T_s|$.

Additionally, the computed Reynolds numbers, friction factors, and pressure drops are shown in Figures 2.21 - 2.23.

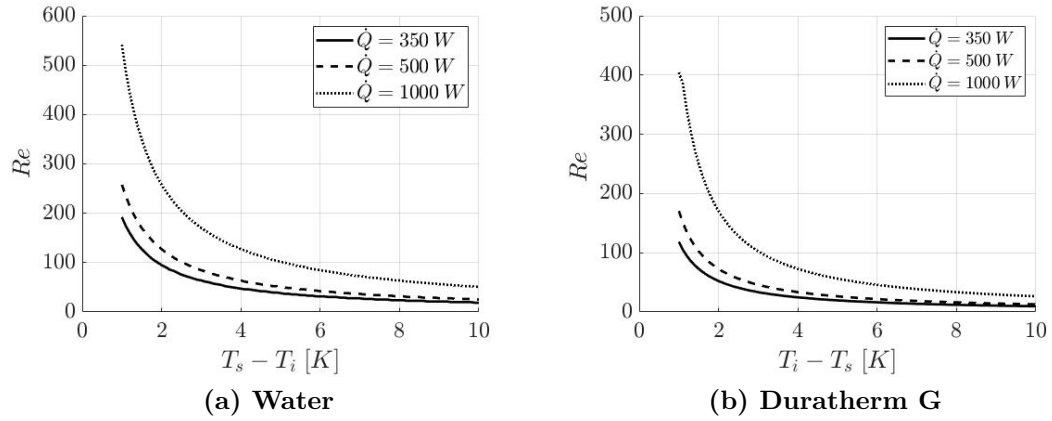


Figure 2.21. Heating and cooling fluid predicted Reynolds number as a function of $|T_i - T_s|$

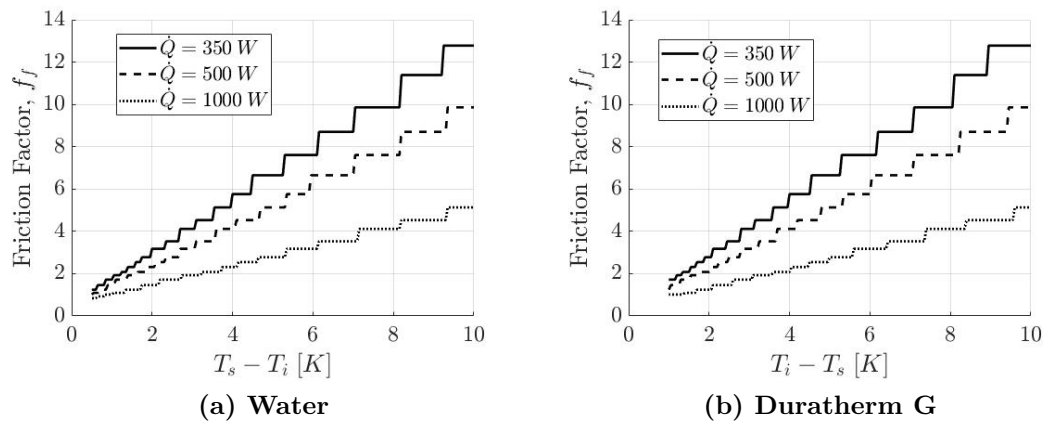


Figure 2.22. Heating and cooling fluid predicted friction factor as a function of $|T_i - T_s|$.

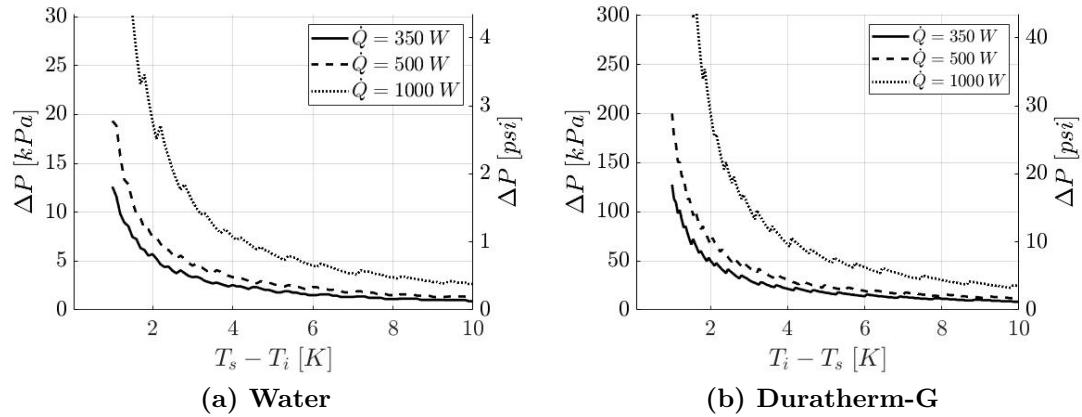


Figure 2.23. Heating and cooling fluid predicted pressure drop as a function of $|T_i - T_s|$.

Figure 2.21 shows that the computation used is valid for the range of expected Reynolds numbers. The results of the pressure drop calculation will be discussed next in Section 2.3.3.

2.3.3 Microtube Structural Analysis

The pressure drop analysis shows that the force on the microtubes has the potential to be substantial, and so it is helpful to estimate the pressure drop the microtubes can withstand. To do this, a single microtube is analyzed as a beam with fixed ends and a uniform distributed load, as shown in Figure 2.24.

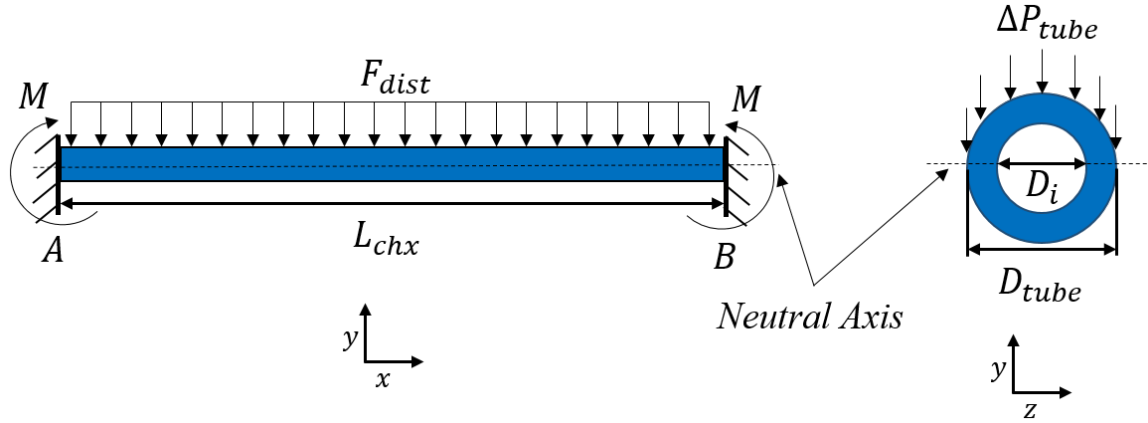


Figure 2.24. Schematic of structural analysis performed on a single microtube acting as a doubly-fixed beam.

The distributed load, F_{dist} , is approximated as

$$F_{dist} = 1/2\pi D_{tube} \Delta P_{tube} \quad (2.14)$$

where ΔP_{tube} is the pressure drop across a single microtube. This structural setup has a moment, M , at locations A and B (see Figure 2.24), given by Equation 2.15 [51].

$$M = \frac{F_{dist} L_{HX}^2}{12} \quad (2.15)$$

The maximum moment, M_c , at A and B occurs at the location furthest from the neutral axis. The stress, σ , at this location is given by Equation 2.16.

$$\sigma = \frac{M_c}{I} = \frac{M}{s} \quad (2.16)$$

where s is the section modulus and I is the moment of inertia [51]. For a hollow tube, the moment of inertia is given by Equation 2.17 [47], and the section modulus is given by Equation 2.18 [51].

$$I = \frac{\pi(D_{tube}^4 - D_i^4)}{64} \quad (2.17)$$

$$s = \frac{2I}{D_{tube}} \quad (2.18)$$

Stainless steel has a tensile strength of 700 MPa [47]. Changes in tensile strength due to temperature changes were not taken into account in this analysis. If the stress in Equation 2.16 is set to the tensile strength, then Equations 2.14-2.18 can be solved for ΔP_{tube} to determine how much pressure drop a microtube can withstand before deformation. This analysis results in a maximum allowable pressure drop of 98.4 KPa (14.3 psi). If the limit is set such that the pressure drop across the entire tube bundle does not exceed this limit, then an upper bound on the allowable mass flow rate can be set. For water, this limit occurs at .14 kg/s (2.3 GPM). For Duratherm G, the limiting flow rate occurs at .08 kg/s (1.4 GPM).

2.3.4 Water Mass Flow Rate

With this preliminary analysis, a target mass flow rate for testing can be determined. It was desired to maintain a high enough mass flow rate so that the temperature difference, $|T_i - T_o|$, was low enough to assume nearly-constant heating/cooling over all the microtubes. In Equation 2.12, the term on the right is on the order of $10^{-2} - 10^{-6}$ for water at the desired range of conditions, which indicates that T_s is much closer to T_i than it is to T_o . For the purpose of selecting test conditions, one could say that T_s is approximately equal to T_i . To keep the temperature difference within 2 K and still remain within the allowable mass flow limit, a flow rate of .063 kg/s (1 GPM) was selected.

2.3.5 Oil Mass Flow Rate

For the oil bath, the pump only has 3 discrete settings (high, medium, and low) to control flow rate. This required the mass flow rates given by the pump to be measured to determine the desired pump setting.

To measure the volumetric flow rate of the oil, a catch-and-weigh method was used. Because of the significant viscosity change of the oil with temperature, it was necessary to measure the volumetric flow rate at each temperature setting that was used during testing. To do this, a three-way directional control valve was installed in the oil return line (see Figure 2.12). The oil was circulated through the heat exchanger (directional control valve was opened to the oil bath) until it was uniformly at the desired temperature, at which point the flow was re-routed to the exit line, which fed into a 4,000 mL Erlenmeyer flask. The amount of time the oil took to fill 500 mL was measured three times with a stopwatch and the average was recorded for each operating temperature and pump speed. The mass flow rate was then taken by multiplying the density of oil, interpolated from A.5, by the volumetric flow rate. The results of this measurement are shown below in Figure 2.25. These results are shown with error bars, and a discussion on how this uncertainty was obtained is documented in Section 2.3.6.

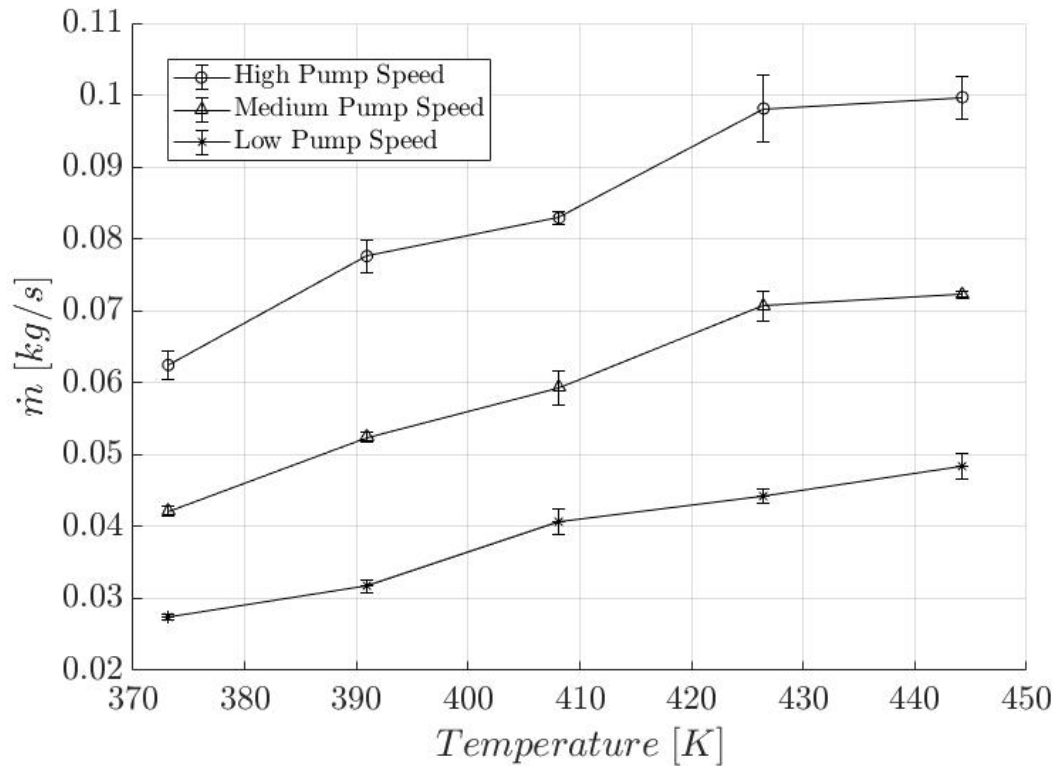


Figure 2.25. Measured oil mass flow rates at varying temperature and pump speed with uncertainty.

Figure 2.25 shows that at the set inlet temperature used in the heat transfer analysis (392 K), the "high" pump speed delivers a mass flow rate that is just under the maximum allowable mass flow rate (.08 kg/s) determined from the structural analysis. The "low" and "medium" pump speeds were tested initially, but conduction along the heat exchanger shell caused the inlet temperature to drift, and so the "high" pump speed was required to maintain a constant inlet temperature. Additionally, the viscosity change of the oil over the temperature range considered will reduce the stress on the tubes substantially, so more mass flow is allowed to flow for the same amount of pressure drop. If the heat transfer analysis is run for oil with the material properties at 444 K, then the allowable mass flow rate for a pressure drop of 98.4 KPa increases to 0.11 kg/s. For these reasons, the oil mass flow rate was decided to be set to the

”high” pump setting, with variable but known mass flow rates for all tests. The oil bath temperature setting used for each tests is documented in Appendix A.8.

2.3.6 Uncertainty Analysis

Mass Flow Rates

The oil and water mass flow rates are computed by Equation 2.19, where \dot{m} is the fluid mass flow rate, ρ is the fluid density, V is the volume the fluid fills in a period of time, and t is the amount of time it takes the fluid to fill that volume.

$$\dot{m} = \frac{\rho V}{t} \quad (2.19)$$

Oil density was determined from linear interpolation as a function of temperature from A.5. Water density was determined from NIST Chemistry Webbook [52]. The uncertainty cited in density for liquid water is .0001% and can therefore be assumed negligible. Because material properties were taken for pure water, and the water used was tap water, there will be a bias error in the material properties. However, this bias error will be assumed negligible. The uncertainty of oil density was computed to be $\pm .71 \text{ kg/m}^3$ based on three trials provided by Duratherm Heat Transfer Fluids. For each catch-and-weigh test, volume was constant (500 ml for oil and 2000 ml for water), so the uncertainty for volume, δV , is assumed to be zero. For each data point, three time trials were taken and averaged. Therefore, the uncertainty for time, δt , is given by Equation 2.20, where σ is the standard deviation, and n is the number of trials.

$$\delta t = \frac{2\sigma}{\sqrt{n}} \quad (2.20)$$

The uncertainty for fluid mass flow rate is then computed using:

$$\delta \dot{m} = \sqrt{\sum \left(\frac{\partial \dot{m}}{\partial x_i} \delta x_i \right)^2} \quad (2.21)$$

Applying Equation 2.19 to Equation 2.21, the mass flow rate uncertainty reduces to Equation 2.22.

$$\delta\dot{m} = \sqrt{\left(\frac{V}{t}\delta\rho\right)^2 + \left(\frac{\rho}{t}\delta V\right)^2 + \left(\frac{-\rho V}{t^2}\delta t\right)^2} \quad (2.22)$$

Because the oil flow rate and temperature was controlled with a PID controller, the mass flow rates were measured prior to testing, and the temperature and pump settings are assumed to be consistent throughout testing. The resulting oil mass flow rates with uncertainty is shown in Figure 2.25.

Because the water mass flow rate is controlled by a manual valve, it was measured before each test. The average uncertainty for water mass flow rate was determined to be .0015 kg/s. This was obtained by taking three time measurements for each test, applying Equations 2.20 and 2.22, and taking an average of $\delta\dot{m}$ over 136 tests.

Thermal Power Input

The thermal power input is measured as the difference between the heat put into the system by the oil, \dot{Q}_{in} , and the heat taken out of the system by the water, \dot{Q}_{out} . This is the amount of energy that is available to be converted into acoustic power. thermal power input, $\Delta\dot{Q}$, is given in Equation 2.23

$$\Delta\dot{Q} = \dot{m}_{oil}Cp_{oil}(T_{i,oil} - T_{o,oil}) - \dot{m}_{water}Cp_{water}(T_{o,water} - T_{i,water}) \quad (2.23)$$

where Cp is the fluid heat capacity, and T is fluid temperature, measured by the thermocouple probes in Table 2.4

Table 2.4.: Temperature Measurements

Temp. Measurement	Thermocouple Probe
$T_{i,oil}$	TC-OIL-01
$T_{o,oil}$	TC-OIL-02
$T_{i,water}$	TC-H2O-01
$T_{o,water}$	TC-H2O-02

All thermocouples have an accuracy of $\pm 2.2^\circ C$, given by Omega Engineering. The uncertainty of Cp_{water} is .1% [52]. The bias limit in the oil heat capacity is unknown and is assumed to be equal to the bias limit of the heat capacity of water. The uncertainty of heat in/out of the system is then given by Equation 2.24.

$$\delta\dot{Q} = \sqrt{[Cp(T_i - T_o)\delta\dot{m}]^2 + [\dot{m}(T_i - T_o)\delta Cp]^2 + [\sqrt{2}\dot{m}Cp\delta T]^2} \quad (2.24)$$

By applying Equation 2.24 to the oil and water, the resulting uncertainty for thermal power input is given by Equation 2.25.

$$\delta\Delta\dot{Q} = \sqrt{\delta\dot{Q}_{in}^2 + \delta\dot{Q}_{out}^2} \quad (2.25)$$

Acoustic Power Output

Acoustic power output is given by Equation 2.26

$$\dot{W}_{out} = kP^2 \quad (2.26)$$

where k is a constant determined from the linear stability model (see Section 1.2.5), and P is the pressure amplitude at the limit cycle in KPa. Since k is a theoretically computed value, it does not have an uncertainty. Three different types of pressure transducers are used on the rig: unik 5000 differential transducers, a unik 5000 absolute transducer (0-1000 psi, 0-6.89 MPa), and a kulite transducer (0-3000 psi, 0-20.68 MPa). The differential and absolute unik 5000 transducers both have an accuracy of

$\pm.04\%$ FSO, given by GE Druck. The kulite has an accuracy of $\pm.1\%$ FSO, given by Kulite. The uncertainty of the acoustic power produced is then given by Equation 2.27.

$$\delta\dot{W} = \sqrt{(2kP\delta P)^2} \quad (2.27)$$

Efficiency

The efficiency of the system is the ratio of power output to heat input, given in Equation 2.28

$$\varepsilon = \frac{\dot{W}}{\Delta\dot{Q}} \quad (2.28)$$

The uncertainty given to the system efficiency is then defined by Equation 2.29

$$\delta\varepsilon = \sqrt{\left(\frac{\dot{W}}{\dot{Q}}\right)^2 \left[\left(\frac{\delta\dot{W}}{\dot{W}}\right)^2 + \left(\frac{\delta\dot{Q}}{\dot{Q}}\right)^2 \right]} \quad (2.29)$$

Uncertainty Results

To estimate uncertainty, Equations 2.19 - 2.29 were applied to a sample of data taken at steady state. The pressure amplitude was taken by taking the difference in the minimum and maximum data point of the bandpass filtered data for the entire sample. The precision error in each pressure measurement was then determined by Equation 2.30.

$$\delta P = \frac{2\sigma}{\sqrt{n}} \quad (2.30)$$

Similarly, each temperature was determined by taking an average over the entire sample range and the precision error was determined by Equation 2.31.

$$\delta T = \frac{2\sigma}{\sqrt{n}} \quad (2.31)$$

The elemental error sources are summarized in Table 2.5. The uncertainty for the Coriolis flow meter used to measure the refrigerant circulation mass flow rate is also given in this table. This uncertainty was taken from the manufacturer to be 0.10% of the mass flow rate for accuracy and 0.05% of the mass flow rate for repeatability. The total uncertainty limit is computed by Equation 2.32 , where β is the bias limit and Θ is the precision limit [53, 54].

$$\delta = \sqrt{\beta^2 + \Theta^2} \quad (2.32)$$

Table 2.5.: Uncertainty Limits

Elemental Error Source	Bias Limit (β)	Precision limit(Θ)	Uncertainty Interval(δ)
Oil Density (kg/m^3)	$\pm.71$	0	$\pm.71$
Water Density (kg/m^3)	0	0	0
Time (s)	0	$\pm.023$	$\pm.023$
Oil Cp ($J/kg * k$)	± 2.04	0	2.04
Water Cp ($J/kg * k$)	± 4.20	0	± 4.20
Temperature (k)	± 2.2	$\pm.0011$	± 2.2
Unik Abs. Pressure (KPa)	± 2.76	$\pm.455$	± 2.80
Unik Diff. Pressure (KPa)	$\pm.827$	$\pm.172$	$\pm.845$
Kulite Abs. Pressure (KPa)	± 20.7	$\pm.034$	± 20.7
Coriolis Flow Meter (%)	$\pm.10$	$\pm.05$	$\pm.11$

Applying the uncertainties in Table 2.5 gives the experimental uncertainties in Table 2.6 below.

Table 2.6.: Computed Uncertainty

calculation	Uncertainty	Uncertainty Percent ($\delta x/x$)
Oil \dot{m} (kg/s)	$\pm.002$	$\pm 3.25\%$
Water \dot{m} (kg/s)	$\pm.0005$	$\pm.78\%$
R-218 \dot{m} (kg/s)	-	$\pm.11\%$
\dot{Q}_{in} (w)	± 397	$\pm 105\%$
\dot{Q}_{out} (w)	± 870	$\pm 232\%$
$\delta\Delta\dot{Q}$ (w)	N/A	N/A
$\delta\dot{W}$ (w)	$\pm.003 - .42$	$\pm.83\% - 19.6\%$
$\delta\varepsilon$	N/A	N/A

The uncertainty analysis reveals that the experimental method for measuring thermal power input is not reliable. The reason for this is that the thermocouple bias limit ($\pm 2.2^\circ C$) is a significant percentage of the average temperature drop across the stack (typically between 1-4 K). This was a trade-off incurred between the desire to have a near-constant temperature across the stack, and the desire to measure heat in and heat out. Keeping the inlet and outlet temperatures close together drives the uncertainty up, but ensures an even distribution of heating and cooling in the stack. Therefore, efficiency cannot be accurately measured and is not reported in this thesis.

The measured acoustic power output has varying uncertainty based on transducer location and type. The steady-state power output with uncertainty is plotted as a function of resonator location in Figure 2.26.

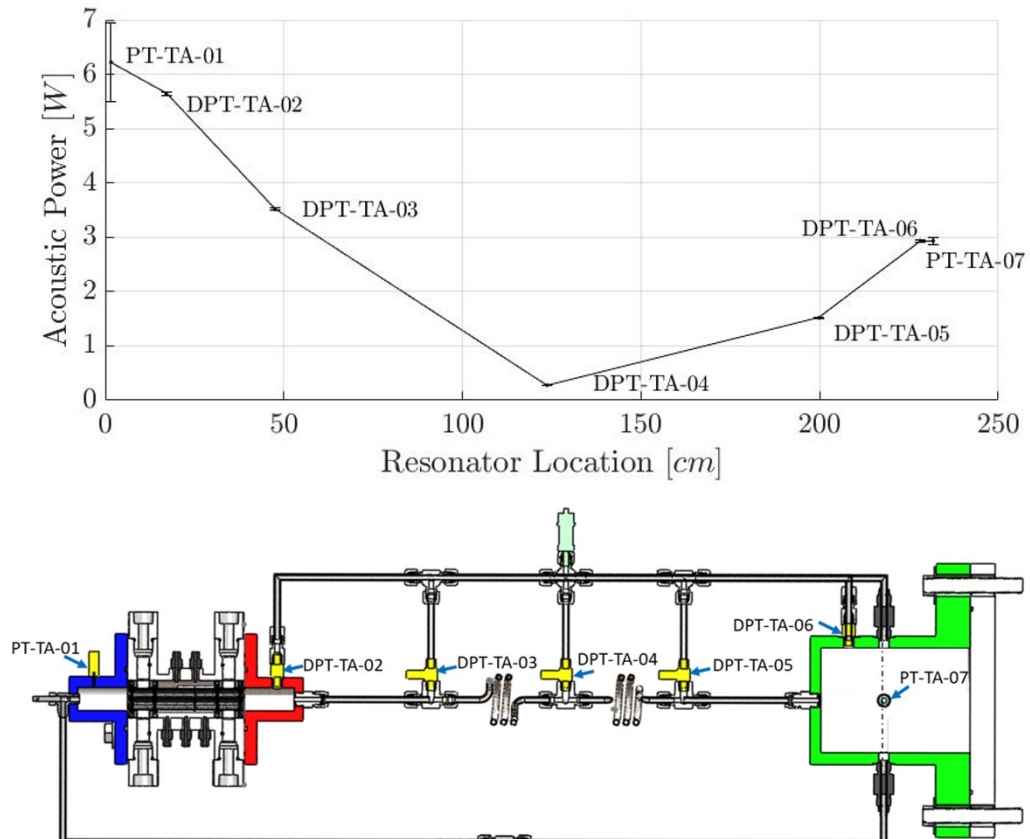


Figure 2.26. Acoustic power of sample data showing uncertainty. The locations of pressure transducers are highlighted in schematic for reference

The data shown in Figure 2.26 is a sample of data taken at a bulk pressure of $1.05 P/P_{cr}$ and a ΔT of 105 K. These results show that the differential pressure transducers offer a near-negligible amount of uncertainty, while the Kulite offers the most uncertainty.

3. EXPERIMENTAL RESULTS

A total of 136 tests were conducted between December 2018 and August 2019 to characterize the thermoacoustic response of R-218 in its transcritical region and assess its feasibility for fluid pumping. The tests were conducted based on the experimental objectives detailed in Section 2.1. A summary of the tests conducted is given in Table 3.1, and a comprehensive table of testing conditions and results is given in Appendix A.8.

First, it was desired to test the improvement in performance provided by the heat exchanger. To do this, the heat exchanger was interfaced with Alexander's resonator section [4] and data was taken to compare the results to previous measurements. Once this set of tests was completed, the heat exchanger was then interfaced to the rig described in Chapter 2.

The second set of tests investigated the bulk pressure effects. This parameter was varied between $0.9 P/P_{cr}$ (2.38 MPa) and $1.3 P/P_{cr}$ (3.43 MPa), and ΔT was varied between 79 K and 150 K. The upper limits on the hot side temperature and the bulk pressure were determined by the structural limits of the heat exchanger. The epoxy securing the microtubes is rated to a maximum temperature of 180 °C. Because the heat exchanger was a custom-designed part, and it was not tested to failure, the pressure limit of the heat exchanger is unknown, and was limited to less than 3.79 MPa (550 psi) based on the manufacturer's recommendation.

The third set of tests evaluated the influence of the length of Resonator Section 2. This length was varied between 203 cm and 102 cm, and data for each length was collected at three different bulk pressures. ΔT was held constant at 116 K for this set of tests.

The final set of tests were conducted to assess the potential to extract energy from the waves by evaluating fluid pumping ability of the rig. In this set of tests,

a recirculation line with check valves and a Coriolis flow meter was installed. The check valves allowed the pressure amplitude to create circulation in the line, which was measured by the flow meter. The tests were conducted by slowly opening a hand valve on the recirculation line at ΔT s ranging from 116 K to 150 K, and bulk pressures ranging from $1.05 P/P_{cr}$ (2.77 MPa) to $1.30 P/P_{cr}$ (3.43 MPa).

Table 3.1.: Test Summary

Test Matrix	Test Numbers	Goal	Variables	Range	Constants
A	1-4	Assess the performance improvement provided by heat exchanger over heating cartridges	P/P_{cr} ΔT	1-1.3 79-89 K	Res. 2 length = 1m Rig Configuration: Gen. 1 rig
B	22-60	Characterize thermoacoustic behavior with varying bulk pressure and ΔT	P/P_{cr} ΔT	0.9-1.3 79-150 K	Res. 2 length= 203 cm Rig Configuration: Gen. 2 rig
C	67-78	Assess the impact of varying resonator length on thermoacoustic response	P/P_{cr} Res.2 Length	1.05-1.2 102-203 cm	$\Delta T = 116K$ Rig Configuration: Gen. 2 rig
D	79-108	Assess fluid pumping capabilities at $\Delta T = 116K$	P/P_{cr} Valve Angle	1.05-1.2 0°- 90°	Res. 2 length = 178 cm Rig Configuration: Gen. 2 with recirculation line
E	110-130	Assess fluid pumping capabilities at $\Delta T = 134K$	P/P_{cr} Valve Angle	1.05-1.3 0°- 90°	Res. 2 length = 178 cm Rig Configuration: Gen. 2 with recirculation line
F	131-164	Assess fluid pumping capabilities at $\Delta T = 150K$	P/P_{cr} Valve Angle	1.05-1.3 0°- 90°	Res. 2 length = 178 cm Rig Configuration: Gen. 2 with recirculation line

3.1 Testing and Data Analysis Methods

Before fluid was transferred into the test article, the rig was leak-checked with nitrogen and then evacuated to prevent the mixture of air with refrigerant. Because R-218 is a greenhouse gas and release into the atmosphere needs to be prevented, the refrigerant was reclaimed into a tank whenever a test article seal needed to be broken. Once refrigerant was transferred into the system, the water and oil supply were turned on and run until they reached steady state temperatures. At the beginning of each testing day, the water supply volume flow rate was measured and adjusted until it was within 10% of 3.79 LPM. The oil bath was preset to the desired hot side temperature and pump setting.

Once steady state temperatures were reached, the test article was pressurized to approximately 1.7 MPa, and the isolation valve was closed to allow for differential pressure readings. The rig was then pressurized further to the approximate desired bulk pressure. To get the correct bulk pressure, the run valves were closed, isolating the test article from the bladder accumulator and causing the pressure to spike, changing the bulk pressure by an unpredictable amount. The average bulk pressure was then estimated using a one-minute time history of live pressure data, and if the bulk pressure was not at the desired test condition, the run valves were opened and the nitrogen pressure was adjusted. The process was repeated until the bulk pressure reached the desired test condition. Once all pressures and temperatures reached a steady state condition, data was recorded at 2000 Hz for approximately 150 seconds. The full set of procedures is located in Appendix A.7.

The thermoacoustic oscillation frequency was determined by applying a Fast-Fourier Transform (FFT) to the raw data taken by each pressure transducer. To obtain the pressure amplitudes, the raw data was put through a 2nd order lowpass Butterworth filter with the frequency range set between 0.5 and 1.5 times the frequency determined by the FFT. The pressure amplitude was then averaged over the

entire steady state interval. The pressure amplitudes reported in this thesis for each test given by PT-TA-01, located in the hot side cavity, using this method.

3.2 Test Matrix A: Gen. 1 Rig Test Results

Previous tests conducted by Dayle Alexander at Zucrow Labs utilized a heating cartridge to heat the R-218 to its critical temperature with no source of cooling [4]. Her rig was labeled the "Gen. 1" rig. Initial testing was conducted using geometry similar to Alexander's in order to demonstrate improvement in performance of the heat exchanger over the heating cartridge. Besides the addition of the heat exchanger, two other changes were made from the previous test setup: a hot side cavity was added to the top of the stack, and the feedline length was increased by 33 cm, giving a total length of 94.6 cm. These two modifications were expected to decrease the frequency of the thermoacoustic response slightly, and this hypothesis was confirmed by experimental results. The first set of tests were conducted using the rig configuration shown in Figure 3.1.

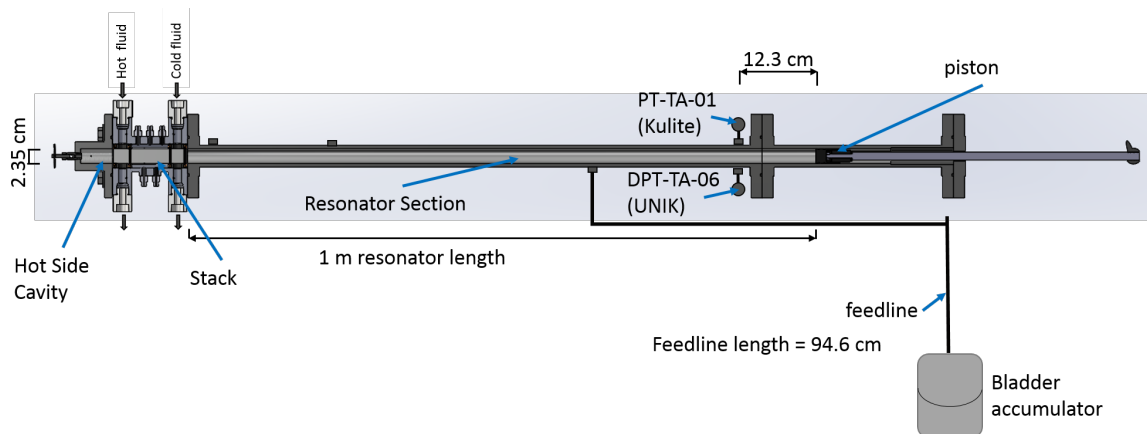


Figure 3.1. Schematic of test article setup for Test 1

Four tests were conducted with this test setup and the results are shown in Figure 3.21.

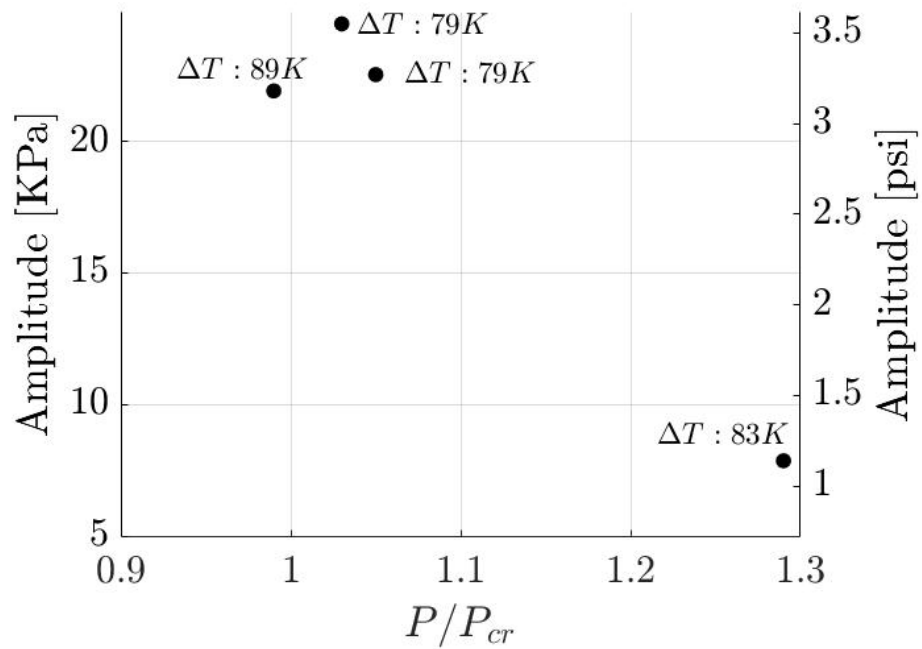
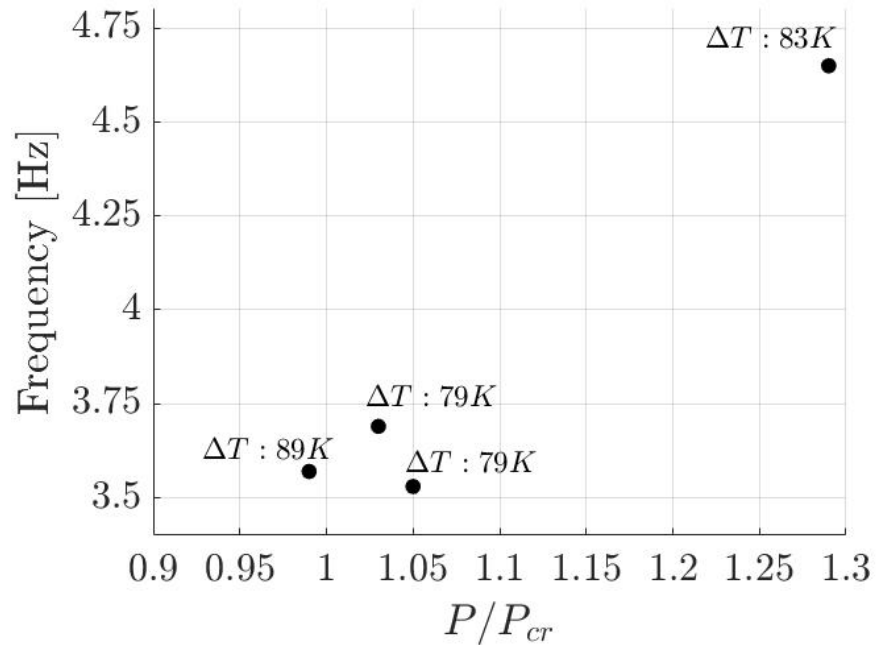
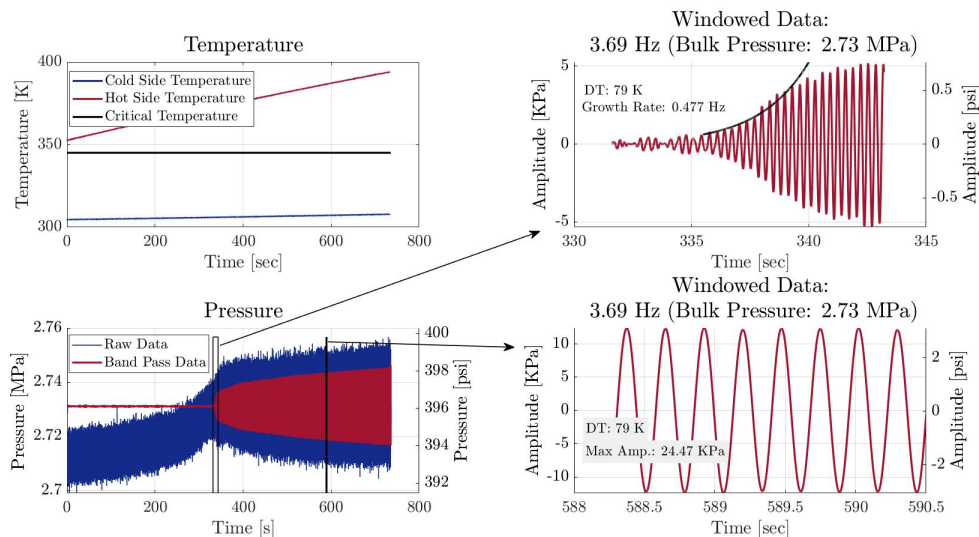
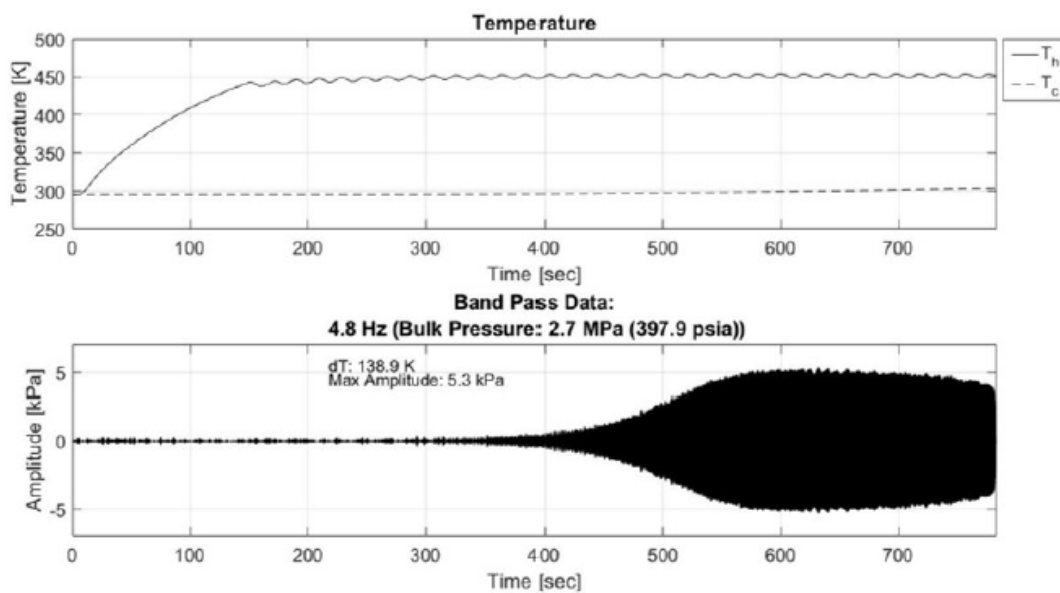
(a) Pressure amplitude with varying bulk pressure and ΔT (b) frequency with varying bulk pressure and ΔT

Figure 3.2. Experimental results obtained from the Gen. 1 rig

These tests gave an assessment of performance increase over the heating cartridge. The largest peak-to-peak amplitude attained was 24.5 KPa (3.55 psid), at a temperature difference of 79 K. This demonstrates a significant performance improvement over tests conducted using the heating cartridge, which at a bulk pressure of 2.74 MPa (398 psi) and a temperature difference of 139 K, provided a peak-to-peak amplitude of 5.3 KPa (.77 psi). Incorporation of the changes described above increased limit cycle amplitudes by 362% when compared with Alexander's results [4]. The comparison of experimental data for a test conducted with the heat exchanger and a test conducted with a heating cartridge at comparable conditions can be seen in Figure 3.3.



(a) with heat exchanger



(b) with heating cartridge

Figure 3.3. Experimental results gathered by Dayle Alexander [4] of a test conducted using the heating cartridge with equal resonator length and similar bulk pressure to Test 1.

3.2.1 Oil and Water Adjustments

The data shown in Figure 3.3a was the first test conducted. Since the temperature drop from the oil to the refrigerant was unknown, the oil heater was operated with a linear temperature increase so that the oil temperature at which thermoacoustic response was incited could be determined. Oscillations were observed when the oil inlet temperature reached 372.9 K. The oil temperature was set to 373.2 K for the remaining Gen. 1 tests.

Additionally, is first test revealed that the water supply needed to be adjusted. Originally, the rig was designed to be cooled by a pump-fed water circulation system, which was the method for cooling used in this test. It can be seen in the temperature plot in Figure 3.3a that the temperature of the water begins to increase slowly, indicating that the water reservoir is too small and mass flow rate, which was measured to be 9.65 LPM for Test 1, is not high enough to keep a constant inlet temperature. For this reason, the water supply was switched from pump-fed recirculating water to water at 288 K from the building water supply in the lab facility.

3.2.2 Phasing of Pressure Amplitude with Axial Location

For the second test, the two pressure transducers that were on the test article were moved to different axial locations to determine if there was variation in phase angle of the pressure amplitude along the resonator. The location of the pressure transducers for Test 2 is shown in Figure 3.4.

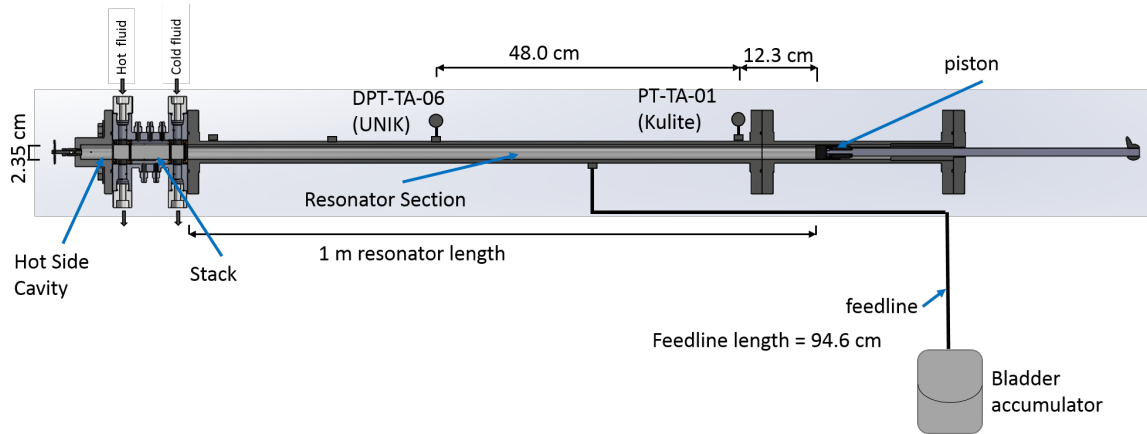


Figure 3.4. Schematic of test article setup for tests 2-4.

It was predicted from Dr. Migliorino's model that the entire resonator section is oscillating in the same phase. This prediction was confirmed as the pressure transducers remained in phase with each other at different axial locations. The data for this can be seen in Figure 3.5

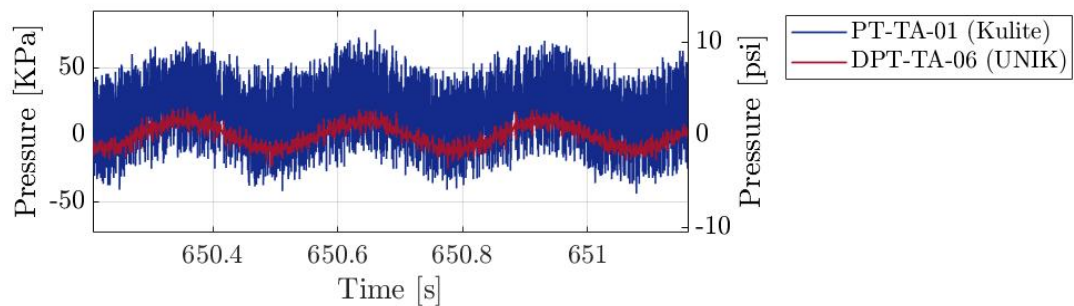


Figure 3.5. Windowed raw data of test 2 showing in-phase pressure oscillations during limit cycle.

3.2.3 Temperatures in the Stack

Five thermocouples were evenly spaced along the stack (see Figures 2.4 and 2.5). The thermocouple probes were placed so that the end of the probe was touching the microtubes in the stack.

The temperature profile along the stack for each test is shown below in Figure 3.6.

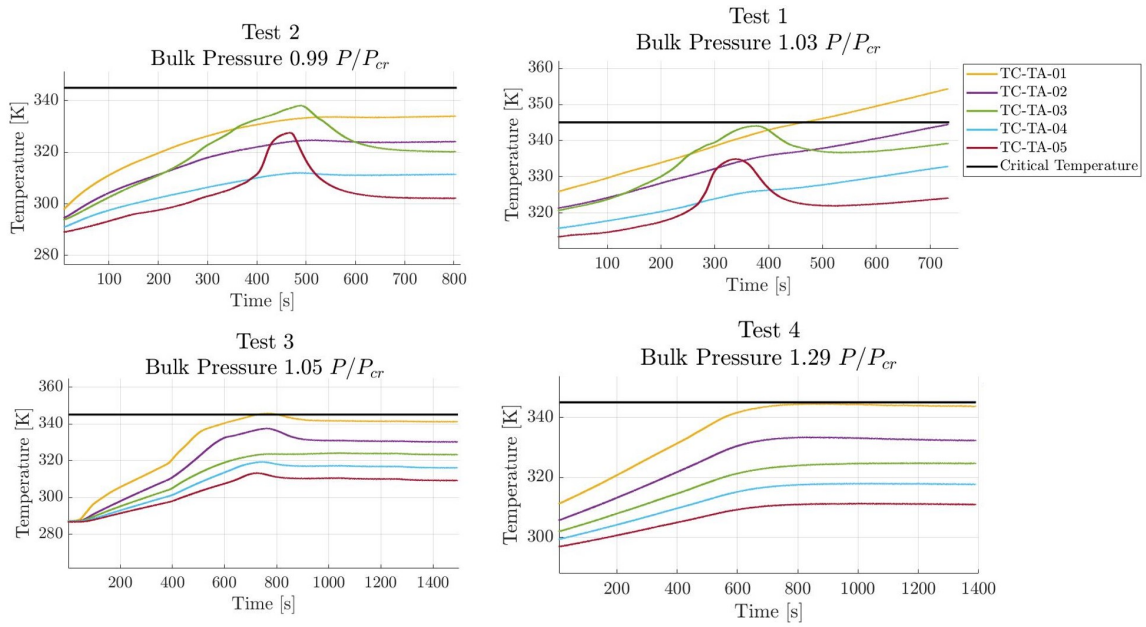


Figure 3.6. Temperature profile in the stack for each test.

It was observed that a "bump" in temperature occurred in some locations during the growth phase of the thermoacoustic response. The size and shape of these "bumps" in temperature appear to be dependent on bulk pressure, as they disappear at higher bulk pressures. It is theorized that temperature increase occurs because of local flash boiling of the working fluid, followed by local compression from the developing thermoacoustic wave. When this behavior was observed in tests 1 and 2, only for probes TC-TA-03 and TC-TA-05, the team contemplated the idea that the observed temperature "bumps" could be the result of instrumentation error, caused by inconsistencies in the contact pressure between the temperature probes and the stack. To test this hypothesis, the temperature probes were switched around for tests 3 and 4. The same behavior was still observed in test 3, indicating that there is a nonlinear temperature gradient along the stack during the growth phase of the thermoacoustic response.

The observed nonlinearity in temperature can be explained by thermodynamic nonlinear effects uncovered by Migliorino and Scalo [44]. Their Navier-Stokes model shows that at bulk pressures near the critical pressure, the density contour in the stack is not symmetric. The fluid in the hot end of the stack, which exists as a gas, pushes on the fluid on the cold end of the stack, which exists as a liquid. As the gas pushes on the liquid, it compresses and increases the local temperature. At bulk pressures away from the critical pressure, it was shown that the gaseous fluid behaves similar to an ideal gas, and produces a symmetric density profile.

3.3 Test Matrix B: Variance of Bulk Pressure and ΔT

Thirty five tests were conducted at steady state conditions in which the bulk pressure was varied from 2.38 MPa ($0.9P/P_{cr}$) to 3.43 MPa ($1.3P/P_{cr}$), and ΔT was varied from 79 K to 150 K. Table 3.2 shows the target test conditions which were conducted. Because the bulk pressure was controlled with a manual valve, the target bulk pressure varied slightly from the actual bulk pressure, and actual bulk pressure for each test condition is recorded in Appendix A.8. For each test matrix presented in this chapter, the numbers inside of the matrix refer to the test number, which are referenced in this document, and in Appendix A.8.

Table 3.2.: Test Matrix # 1: Vary ΔT and Bulk Pressure

		Resonator 2 length: 203 cm							
		0.9	0.95	1	1.05	1.10	1.20	1.30	P/P_{cr}
		2.38	2.51	2.64	2.77	2.90	3.17	3.43	P_{bulk} (MPa)
79	373	48	49	51	52	53	54	55	
105	391	22	23	24	25	26	27	28	
116	408	32	38	33	35	34	36	37	
134	426	39	40	41	42	43	44	45	
150	444	46	47	56	58	57	59	60	
ΔT (K)		T_{hot} (K)							

3.3.1 Predictions on Expected Behavior

The pressure amplitude trend as a function of bulk pressure and ΔT is expected to follow the same trends observed in growth rate by Migliorino and Scalo. Their work predicts that the growth rate as a function of bulk pressure will follow a parabolic trend, where the peak growth rate is dependent on the density gradient, viscous losses, geometrical aspects, and phasing between pressure and velocity [44]. The magnitude of growth rate, and thus pressure amplitude, is expected to increase with increasing ΔT because the increase in thermal energy into the system should increase the acoustic energy in the waveform.

The frequency is expected follow the trend of the sound speed, as the sound speed will dictate how quickly pressure oscillations can travel through the resonator. In the resonator, the fluid is at ambient temperature and is thus a liquid. The sound speed in the resonator is shown in Figure 3.7b. Because it is always at ambient temperature, the sound speed in the resonator is only affected by bulk pressure.

In the hot side cavity and the stack, the temperature is varying with each value of ΔT . The sound speed is also varying with axial location in the resonator due to the temperature gradient. The sound speed in the hot side cavity at the pressure and temperature conditions in Table 3.2 are shown in figure 3.7a. Figure 3.7a shows that the sound speed is decreasing slightly with increasing bulk pressure, and increasing significantly with increasing hot side temperature. Thus, Figures 3.7a and 3.7b together demonstrate that frequency is expected to increase with increasing bulk pressure and with increasing ΔT .

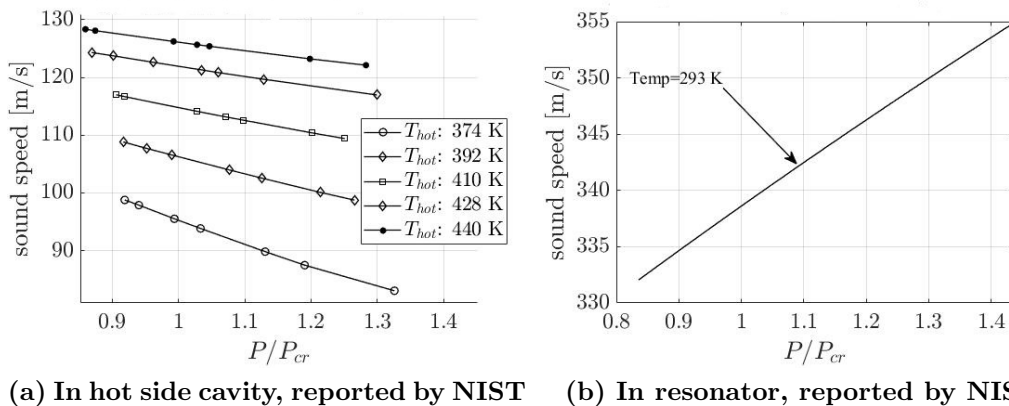


Figure 3.7. Sound Speed at temperatures and bulk pressures used in experimental results

3.3.2 Variance of Bulk pressure and ΔT Results

Figure 3.8 shows the experimental results for frequency and pressure amplitude as a function of bulk pressure and temperature difference. The maximum pressure amplitude achieved was 669 KPa (97 psi) at a bulk pressure of 1.28 P/P_{cr} and ΔT of 150 K. To the author's knowledge, these are the highest amplitude oscillations ever produced in a thermoacoustic instability that did not involve chemical energy release.

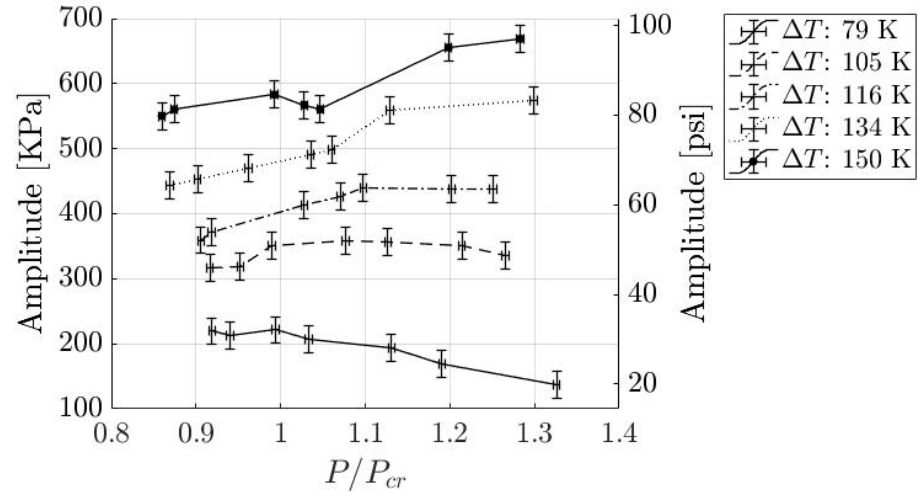
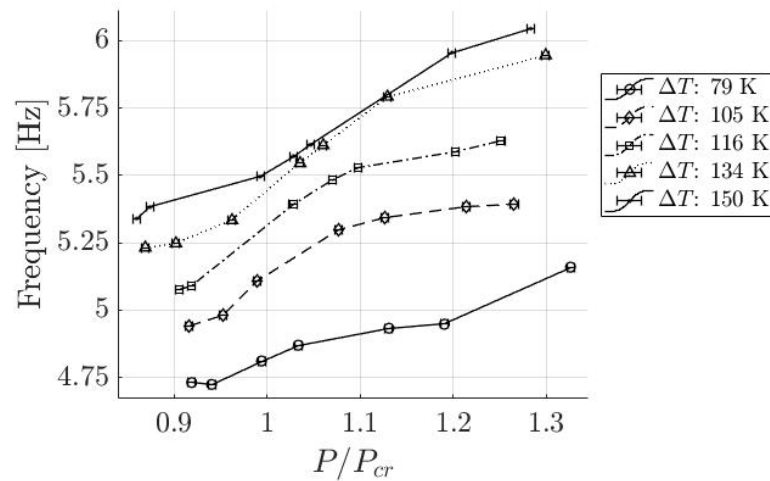
(a) Pressure amplitude with varying bulk pressure and ΔT (b) Frequency with varying bulk pressure and ΔT

Figure 3.8. Experimental Results showing plots of thermoacoustic behavior with varying bulk pressure and ΔT

Figure 3.8 presents insightful information of optimal operating conditions. Figure 3.8a shows that the pressure amplitude is a weak function of bulk pressure and is mostly dictated by the available thermal energy, presented as ΔT . Figure 3.8b shows that frequency increases nearly linearly with bulk pressure, and also increases with ΔT , as expected.

Figure 3.8a suggests that each ΔT contour line has an optimal bulk pressure that produces a peak amplitude. As the ΔT increases, that peak pressure moves away

from the critical pressure. It appears that at ΔT s of 134 K and above, that optimal amplitude is not reached within the operational pressure limits. Equations 1.6 and 1.9 presented in Chapter 1 demonstrate that available acoustic power is proportional to both the pressure amplitude and the frequency, thus showing that higher bulk pressures are likely to allow for higher power extraction.

3.3.3 Modeling Validation

Dr. Migliorino provided modeling support on results obtained in Figure 3.8, based on the linearized tool described in [44]. Figure 3.9 shows a comparison of numeric and experimental results for the test condition at 1.1 P/P_{cr} bulk pressure. To predict pressure amplitude, the viscous losses computed in the model were calibrated by matching a single experimental data point to the model, and extrapolating pressure amplitude for the rest of the range of test conditions.

Figure 3.9 shows that the modelling work is validated by experimental results. Because the waveform shows increasingly nonlinear behavior with increased ΔT , the numerical values are expected to deviate from the experimental values. Figure 3.9a shows that at higher ΔT s, the experimental pressure amplitude is slightly higher than numerical results. A potential explanation for this is that at lower pressure amplitudes, the heat transfer in the stack is dominated by conduction. As the pressure amplitude increases, the velocity increases and it is likely that convection becomes a significant mode of heat transfer in addition to conduction, making the heat transfer in the stack more efficient.

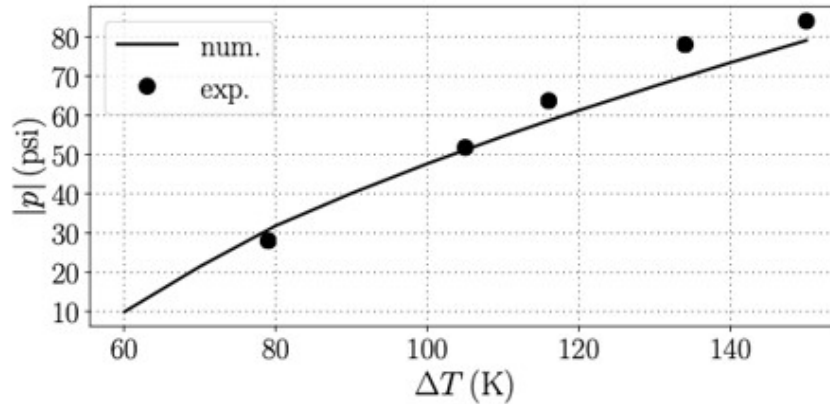
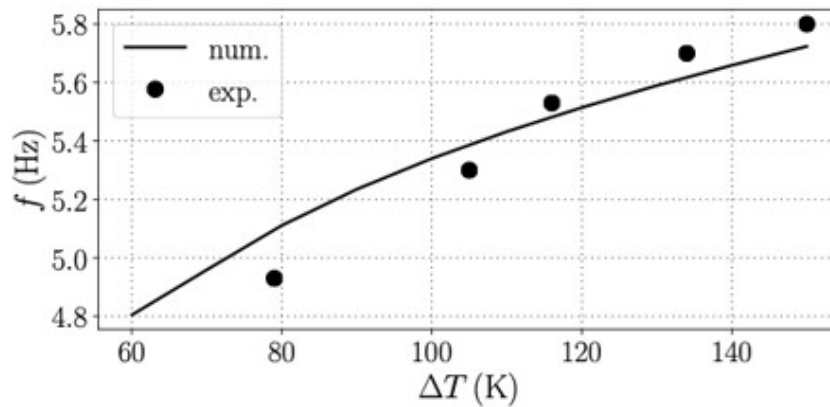
(a) Pressure amplitude vs ΔT (b) Frequency vs ΔT

Figure 3.9. Numerical predictions validated by experimental results for test condition at $1.1 P/P_{cr}$, provided by Dr. Migliorino.

3.3.4 Waveform Shape

There is a noticeable change in the shape of the waveform with varying temperature. Figure 3.11 shows the pressure amplitudes at each pressure transducer along the resonator. While the increase in ΔT increases the pressure amplitude at PT-TA-01 significantly, the pressure amplitude at PT-TA-07 is only increased slightly with increasing ΔT . Additionally, the axial location of the pressure node appears to be moving away from the stack with increasing ΔT . At $\Delta T = 150 K$, the pressure node appears to be closer to DPT-TA-05 than to DPT-TA-04. The test article configu-

ration showing the location of each pressure transducer is shown in Figure 3.10 for reference.

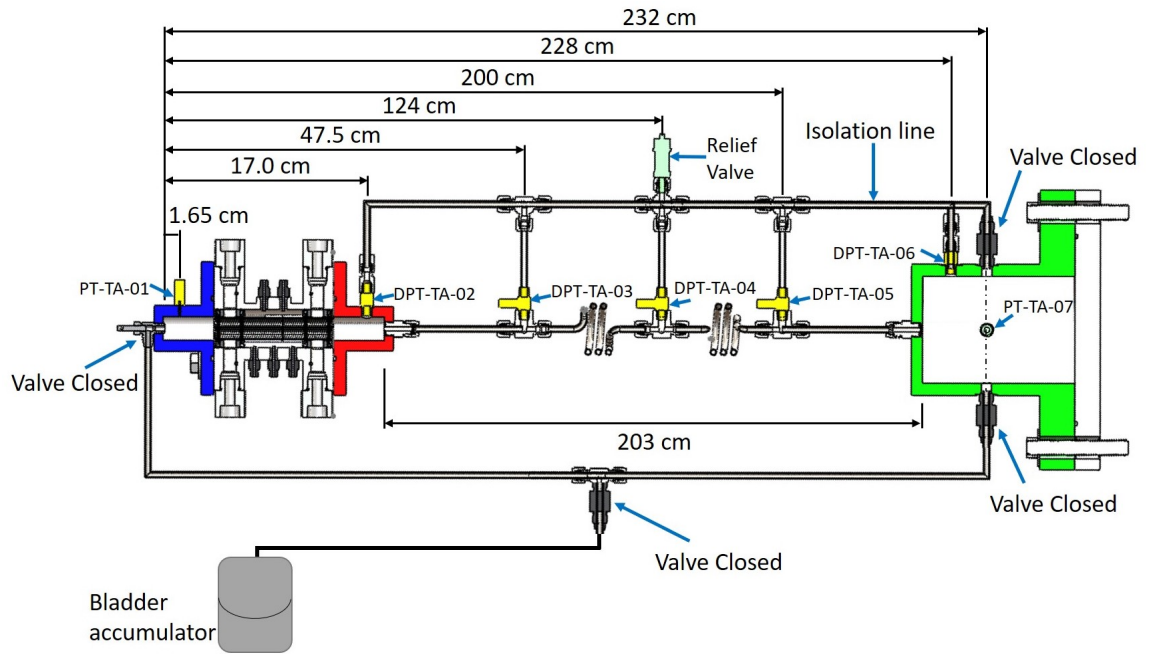


Figure 3.10. Test Article configuration showing location of pressure transducers.

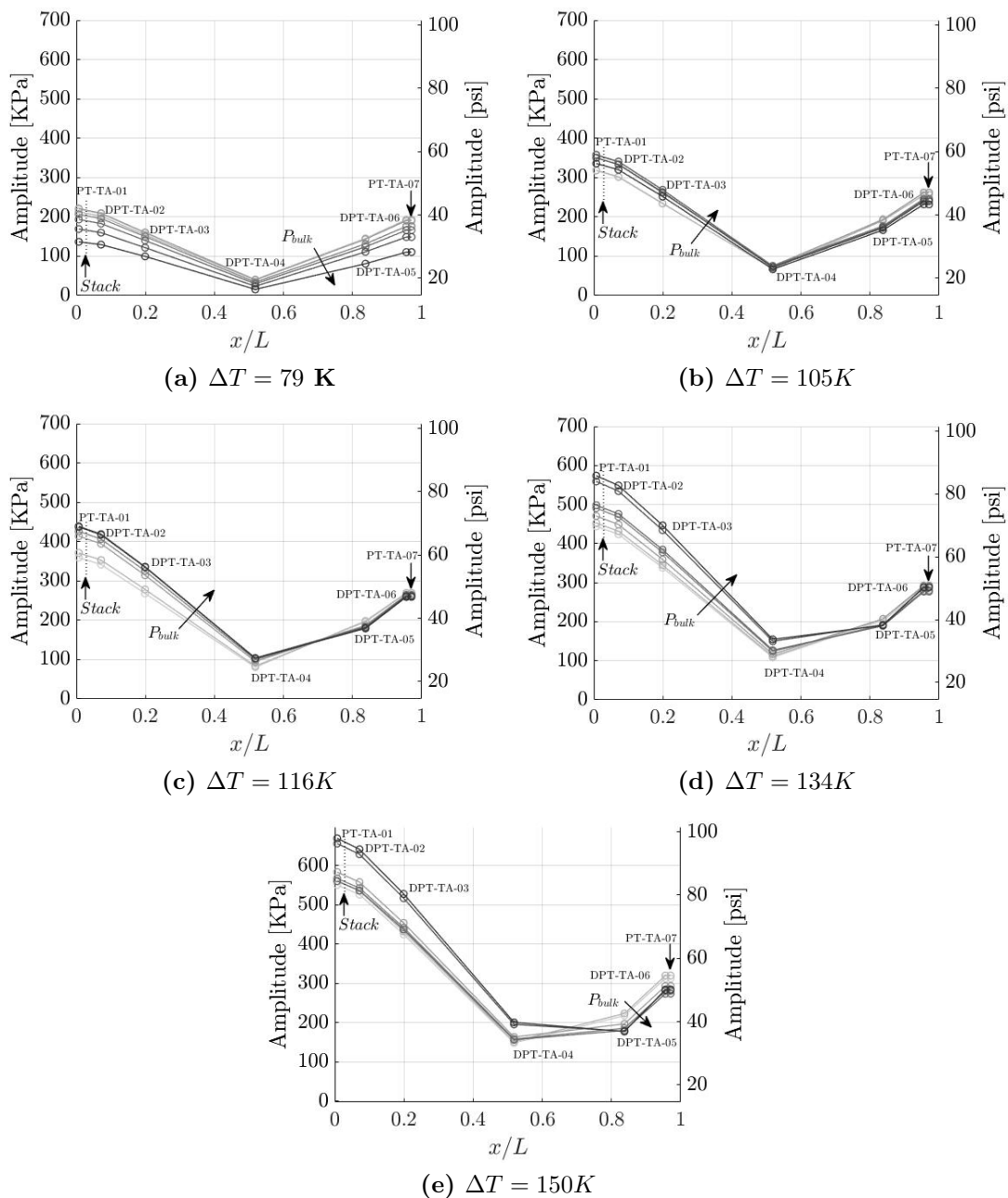


Figure 3.11. Experimental Results showing plots of waveform behavior along the resonator with varying bulk pressure and ΔT . x/L is the relative axial location along the resonator and L is the total resonator length (239 cm).

3.3.5 Time Averaged Pressure Variations

The bulk pressure at PT-TA-01 in the hot side cavity varies significantly from the bulk pressure at PT-TA-07 in Resonator Section 3. The local bulk pressure is obtained by taking a time average of the entire steady-state interval of the raw pressure data for a given pressure transducer. The total bulk pressure reported in this thesis is obtained by taking an average of the local bulk pressure at PT-TA-01 and PT-TA-07. To visualize the behavior, the difference in bulk pressure between PT-TA-01 and PT-TA-07 at each test condition is plotted in Figure 3.12

It is evident that this difference increases with increasing pressure and temperature. This behavior is attributed to the fact that high pressure regions in the waveform are biased toward the heated end of the resonator as noted in Figure 3.11. Fluid in this region spends a larger proportion of the cycle at high pressure and hence the average pressure at these locations is also higher.

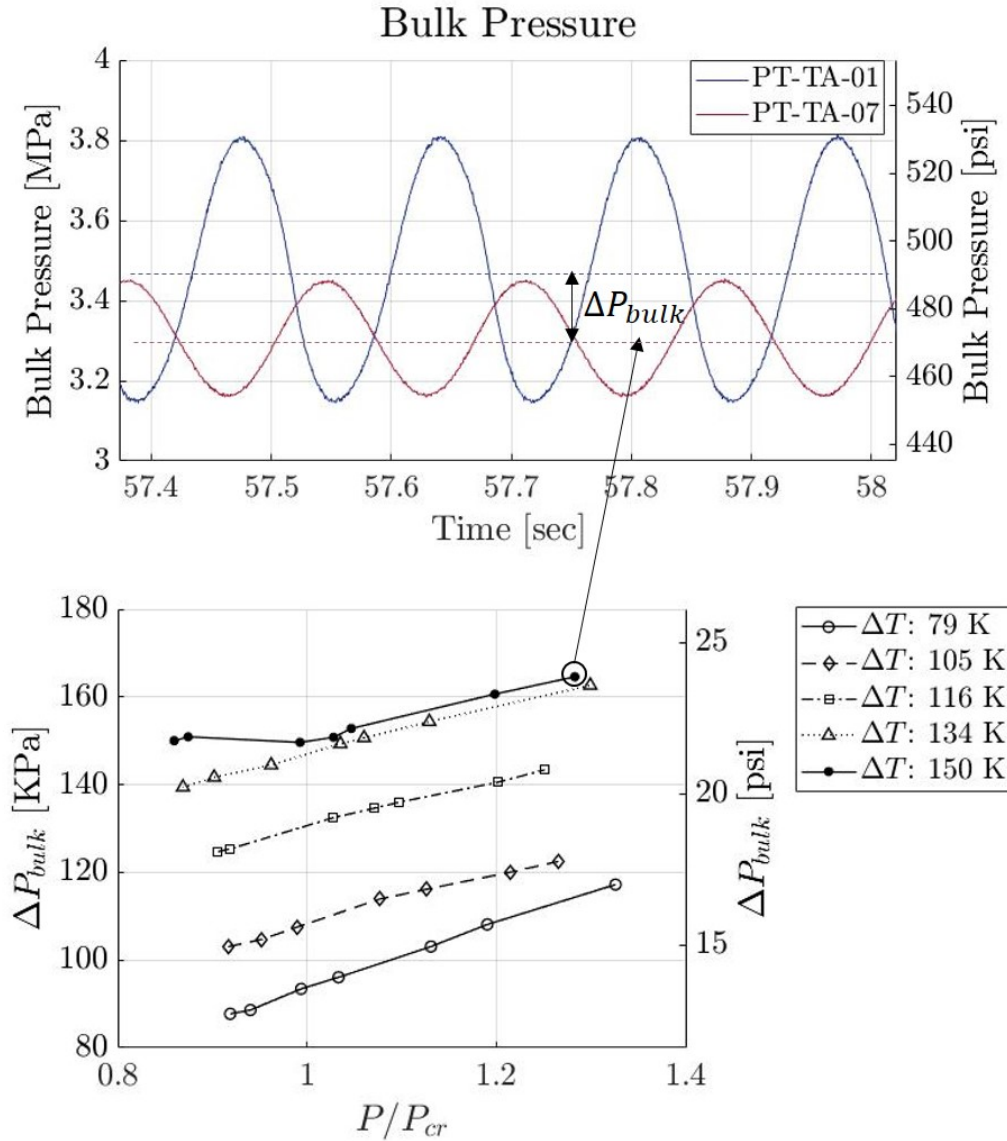


Figure 3.12. Difference in bulk pressure between PT-TA-01 and PT-TA-07 at all test conditions

3.3.6 Investigation of Phase Angle

The phase angle is plotted against relative axial resonator location in Figure 3.13. Little variation in phase angle is observed with varying bulk pressure and with varying ΔT , as the end-to-end phase angle consistently reaches just over 150° . The results show classical standing wave behavior with an end-to-end phasing of 180° . The ob-

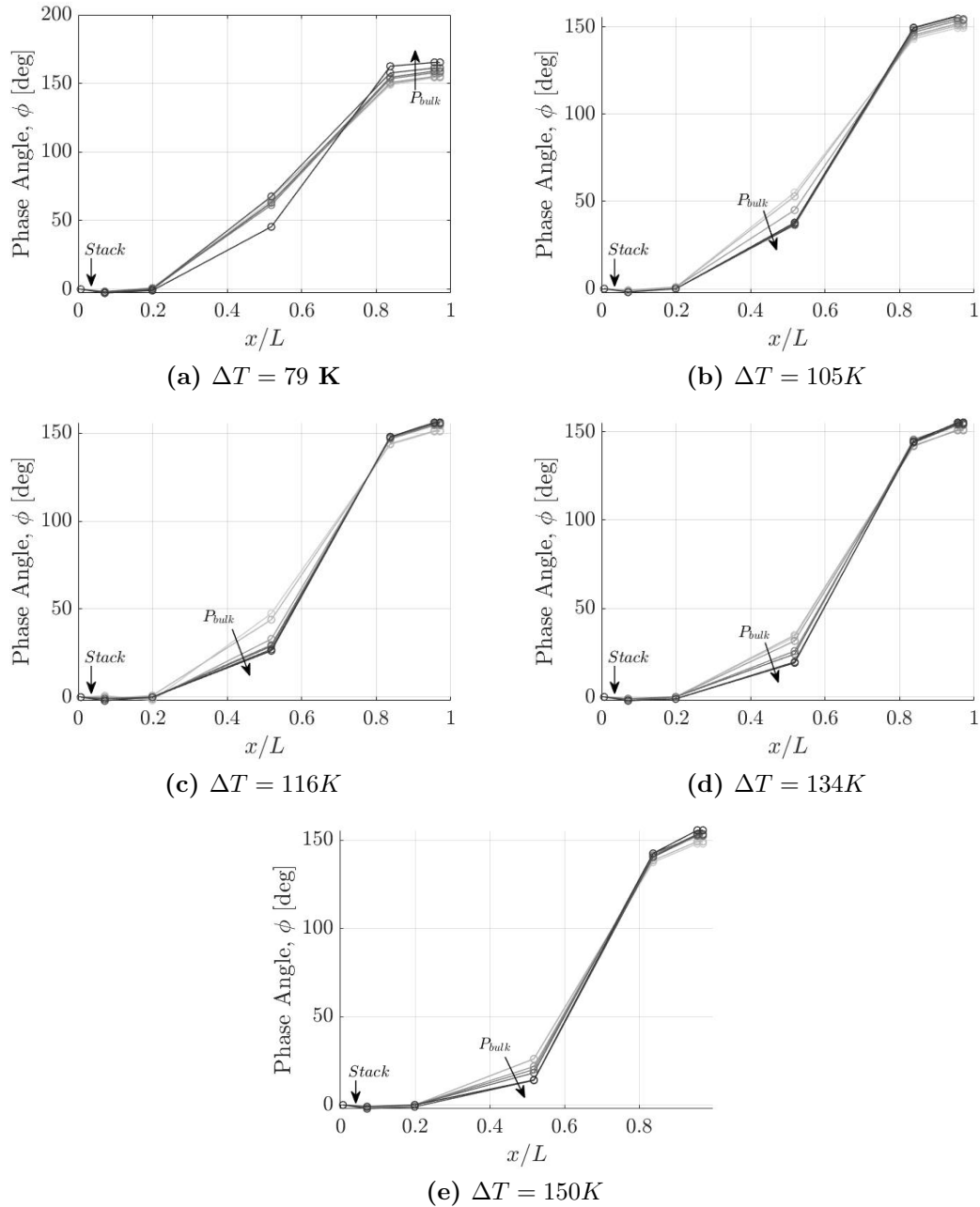


Figure 3.13. Experimental Results showing plots of phase angle along the resonator with varying bulk pressure and ΔT . x/L is the relative axial location in the resonator and L is the total resonator length (239 cm).

served data may vary from expected results because the pressure probes on either end of the rig are several centimeters from the end walls. If the end-to-end phase angle

needed to be confirmed in a future generation, pressure probes could be put on either end wall.

3.3.7 Temperature Gradient Linearity

The temperature gradient consistently appears to be nonlinear in the subcritical region, and then take on a more linear profile in the supercritical region. An example for this change is shown below in Figure 3.15, where the temperature gradient is show for three tests at a ΔT of 116 K and varying bulk pressures.

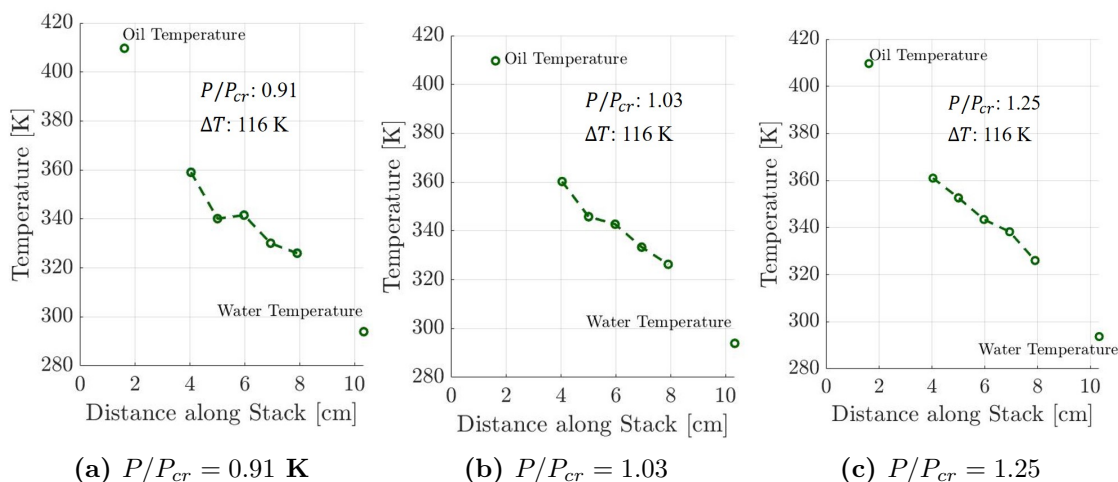


Figure 3.14. Experimental Results showing behavior of the temperature gradient with varying bulk pressure

3.3.8 "Sloshing" Behavior

At the highest ΔT test condition in the subcritical region, a "sloshing" behavior was observed in two tests. This behavior stopped when the pressure was increased into the supercritical range. The "sloshing" occurs at a frequency of approximately .017 Hz in Test 46 and .0068 Hz in test 47. One hypothesis for this is that in the subcritical range, the fluid has a distinct gas and liquid phase. As heat is added, the liquid boils, and this local boiling causes disturbances in the liquid. As the ΔT increases, these

disturbances become increasingly significant, until they are transferring substantial kinetic energy to the liquid, similar to a "rolling boil" in a pot of water. As the pressure is increased into the transcritical range, these disturbances vanish because the fluid no longer has a distinct gas and liquid phase.

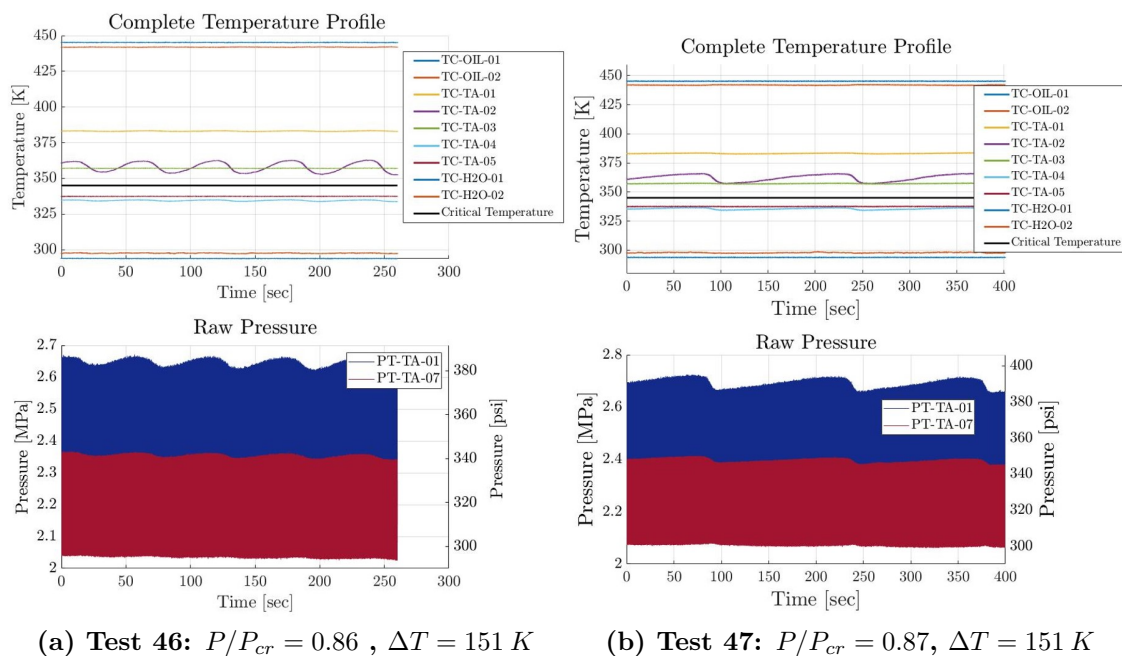


Figure 3.15. Experimental Results showing chugging behavior observed in two tests

3.3.9 Pressure Excursions at high Heating Conditions

While there was not time to do each test multiple times, three tests were conducted again to demonstrate repeatability of the results. In Figure, 3.8a, there is an excursion in the pressure amplitude occurring between $P/P_{cr} = 1$ and $P/P_{cr} = 1.1$. To determine repeatability of those results, three additional tests we conducted in that pressure region. The results of the repeated tests are shown in Figure 3.16. Although the cold side temperature ended up being 2 K colder, the repeated tests are within the uncertainty limits, demonstrating repeatability.

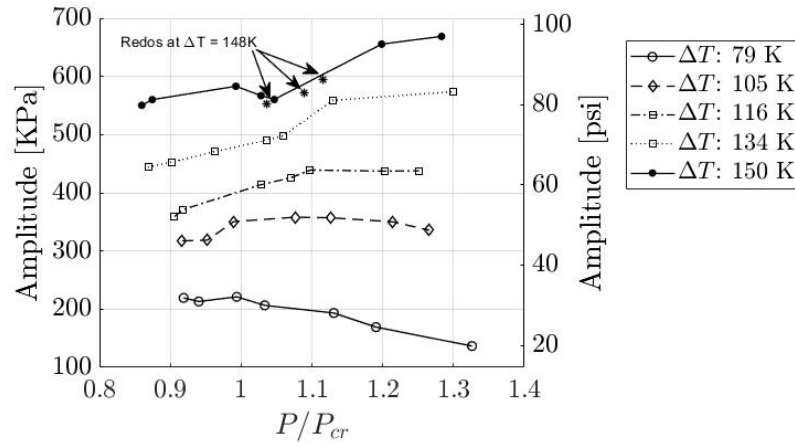


Figure 3.16. Experimental results with additional data to demonstrate repeatability

3.4 Test Matrix C: Variance of Resonator Length

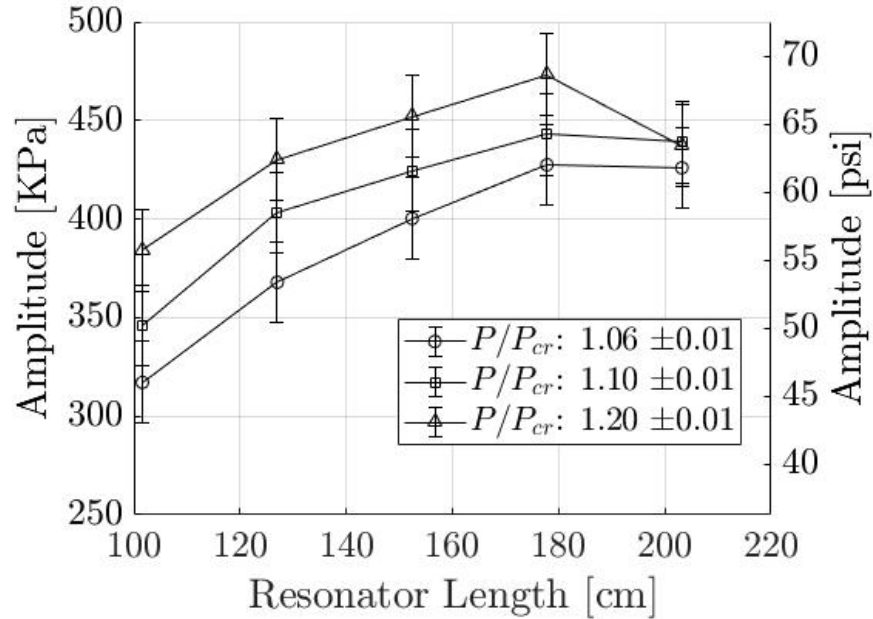
Fifteen tests were conducted at steady state in which the resonator length was varied between 203 cm and 102 cm at three different bulk pressures. The test conditions for each test are shown in Table 3.3.

Table 3.3.: Test Matrix C: Varied Resonator Length

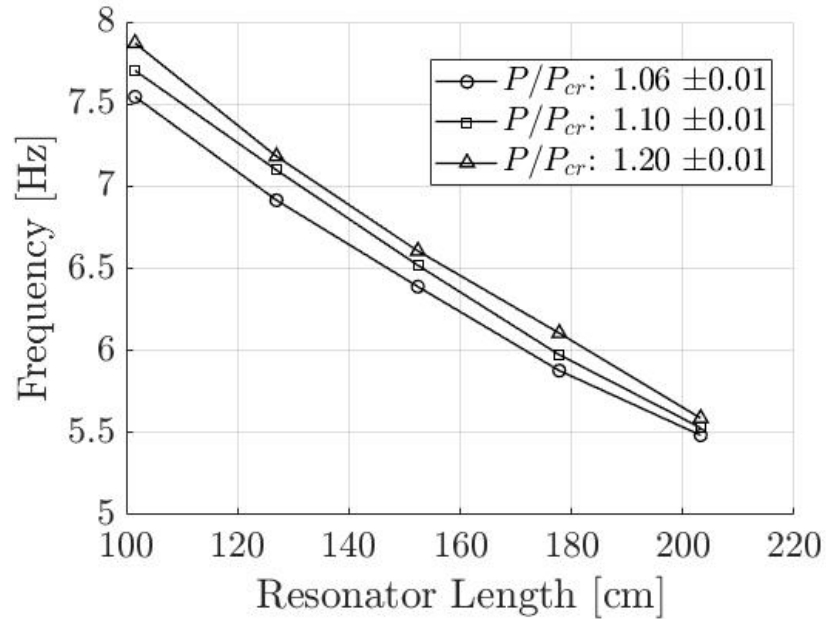
ΔT : 116 K				
	1.05	1.10	1.20	P/P_{cr}
	2.77	2.90	3.17	P_{bulk} (MPa)
203.2 (80)	35	34	36	
177.8 (70)	70	69	71	
152.4 (60)	67	66	68	
127.0 (50)	73	72	74	
101.6 (40)	75	77	78	
Resonator 2 Length, cm (in)				

The resonator length was varied by replacing the two tubing sections above and below DPT-TA-04 (see Figure 3.10) with tubing that varied in length by 25.4 cm increments. The resulting pressure amplitude and frequency with varying resonator length is shown below in Figure 3.17. The amplitudes and frequencies reported in Figure 3.17 were obtained using the same method described to create Figure 2.23.

The ΔT was held constant at 116 K for each of these tests. Currently, the coolant is not temperature-controlled and is therefore subject to fluctuations in ambient temperature. Because of this, tests 34-36 had a lower incoming water temperature (294 K) than tests 66-78 (297 K). To keep the ΔT constant, the hot side temperature was raised from 410 K to 413 K in tests 66-78. It can be seen in Figure 3.17a, that the system performance increases with increasing resonator length. This is because as the resonator length increases, the frequency is lowered, allowing for more thermal diffusion time in the stack, thus increasing the pressure amplitude. The pressure amplitude peaks at 178 cm because as the resonator length increases, the viscous losses also increase. The amplitude peaks because the viscous losses incurred become greater than the benefits of increased thermal diffusion time.



(a) Pressure amplitude with varying resonator length



(b) Frequency with varying resonator length

Figure 3.17. Experimental results showing plots of thermoacoustic behavior with varying resonator length at a constant ΔT of 116 K

3.4.1 Waveform Shape for Various Resonator Lengths

Figure 3.18 shows the waveform shape at three different bulk pressures. The pressure amplitude is plotted as a function of relative axial location along the resonator.

These plots reveal that the waveform shape relative to the resonator length does not vary significantly with changes in resonator length or with changes in bulk pressure.

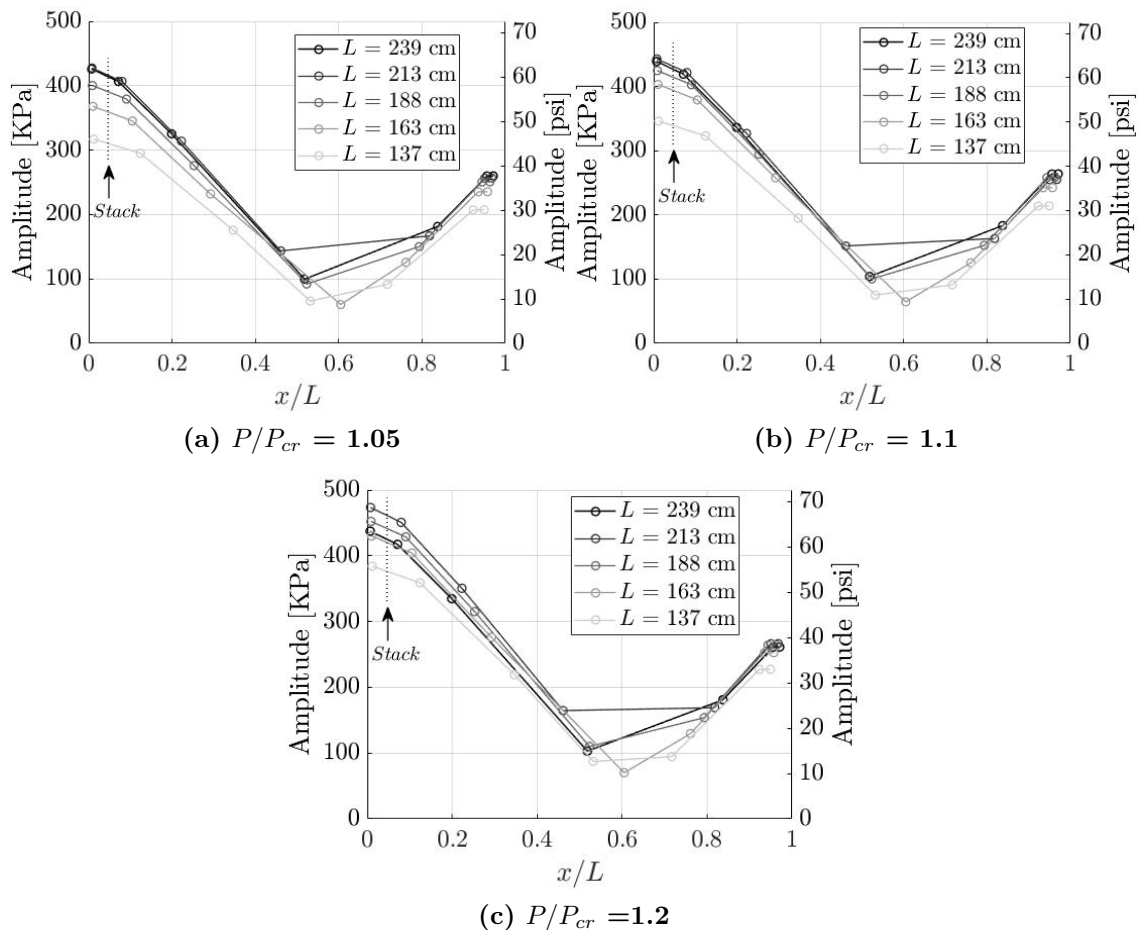


Figure 3.18. Experimental Results showing plots of waveform behavior along the resonator with varying bulk pressure and resonator length

3.5 Assessment of Pumping Characteristics

After characterization of the waveform was concluded, 94 tests were conducted to test the ability for the pressure amplitude to create a sustained, self-induced fluid circulation with the use of two check valves in the recirculation line. The schematic is shown in Figure 3.23.

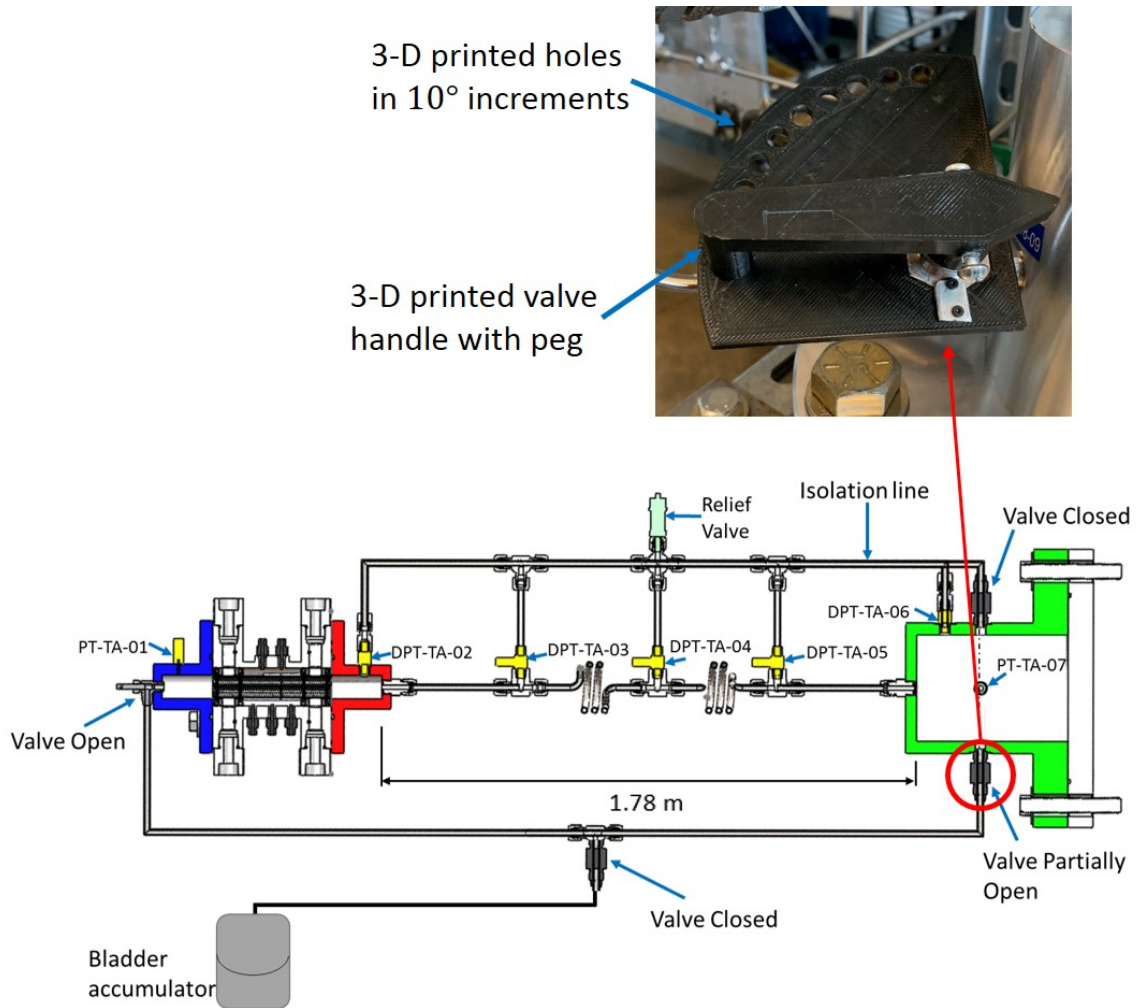


Figure 3.19. Schematic of tests conducted to assess pumping characteristics

Test conditions selected for this set of tests were based on the results of Test Matrices 1 and 2. Because the 178 cm resonator length demonstrated the highest pressure amplitudes, it was selected for the pumping tests. Tests were conducted with bulk pressures of $1.05 P/P_{cr}$, $1.1P/P_{cr}$, $1.2 P/P_{cr}$, and $1.3 P/P_{cr}$, and ΔT s of 116 K, 134 K, and 148 K.

For each of the tests, it was desired to know how much fluid could be taken from the main resonator section and recirculated before the amount of circulating fluid took too much energy out of the acoustic oscillation. When this limit was reached,

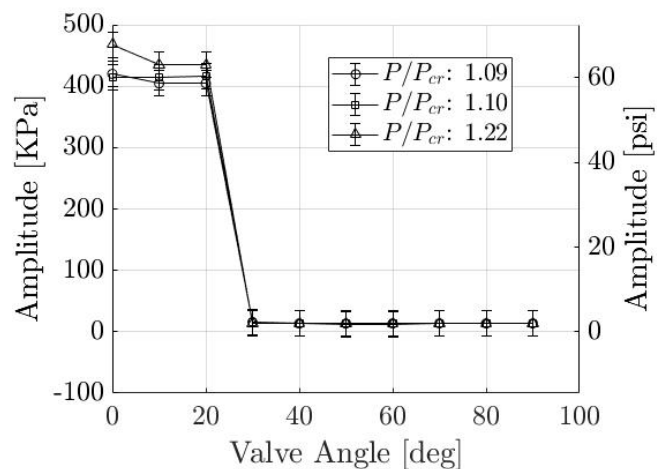
the pressure amplitude would be reduced and in turn the mass flow rate would be reduced. To find this optimal limit, the flow area was metered by adjusting the angle of the hand valve on Resonator Section 3. Initially, the method for controlling the angle on the hand valve was a 3D-printed plate with holes in 10° increments. A handle was printed with a peg such that it would fit into each hole to attain the desired angle (Figure 3.23).

3.5.1 Test Matrix D: Pumping Tests at $\Delta T = 116K$

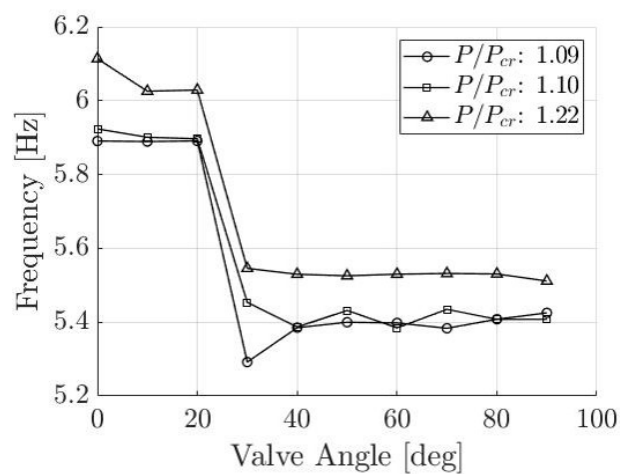
The first set of tests was conducted at a constant ΔT of 116 K. The test matrix for the set of tests conducted is shown below in Table 3.4, and the results are shown in Figure 3.20.

Table 3.4.: Test Matrix D: Pumping Tests at $\Delta T = 116K$

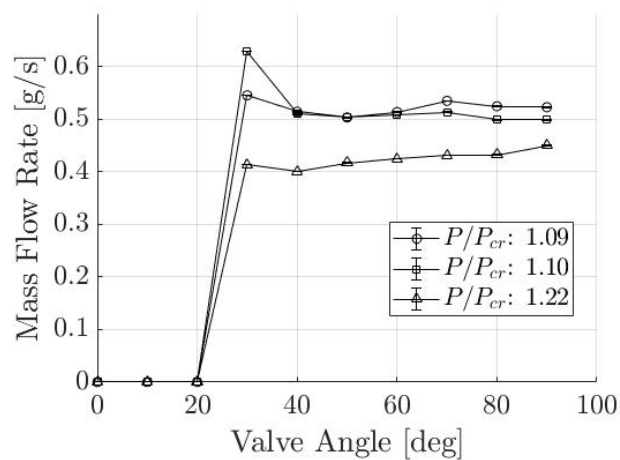
	1.05	1.10	1.20	P/P_{cr}
	2.77	2.90	3.17	P_{bulk} (MPa)
0	99	79	89	
10	100	80	90	
20	101	81	91	
30	102	82	92	
40	103	83	93	
50	104	84	94	
60	105	85	95	
70	106	86	96	
80	107	87	97	
90	108	-	98	
Valve Angle (deg)				



(a) Pressure amplitude with varying valve Angle



(b) Frequency with varying valve Angle



(c) Mass flow rate with varying valve Angle

Figure 3.20. Experimental results obtained from Test Matrix D of pumping assessment

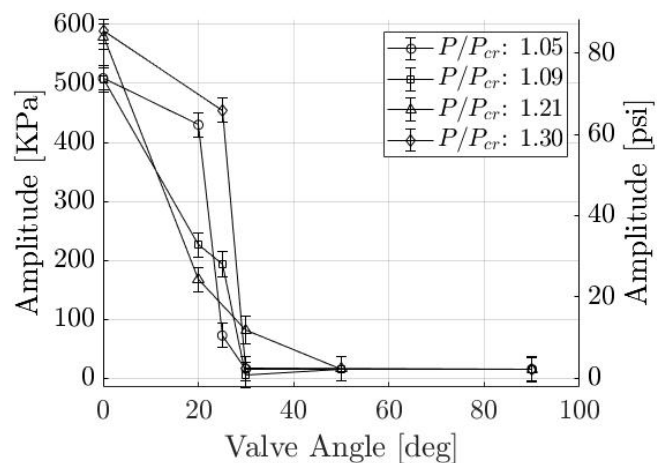
Contrary to expected results, the data shows a binary behavior, where nearly all of the acoustic energy is taken out of the waveform once flow is produced (Figure 3.20a). Once flow starts, it stays relatively constant regardless of the flow area (Figure 3.20c). Additionally, the frequency is decreased because of the volume added to the system by the recirculation line (Figure 3.20b). Upon completing these tests, it became clear that in order to get data where the acoustic energy could be partially tapped off, higher resolution on the valve angles was required. Additionally, these desired conditions could be achieved at higher temperatures and bulk pressures, where the pressure amplitude is higher.

3.5.2 Test Matrix E: Pumping Tests at $\Delta T = 134K$

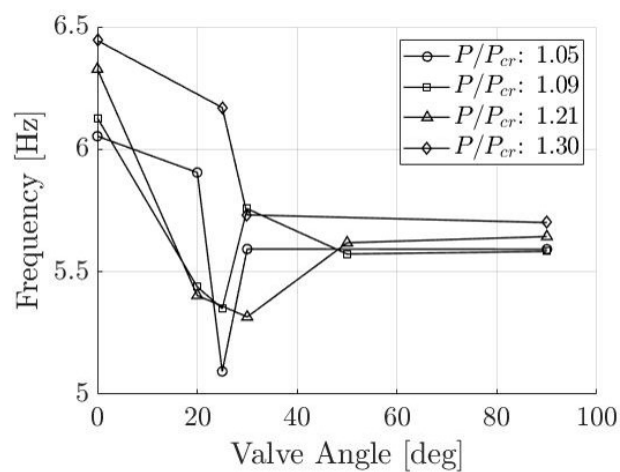
The next set of tests was conducted at a ΔT of 134 K. Test Matrix E is shown below in Table 3.5. Several changes were made for this set of tests. First, since it became clear from Test Matrix D that the response was sensitive in the region of 20 to 30 degrees, data was collected at 0, 20, 25, 30, 50, and 90 degrees. Next, the test condition at 1.3 P/P_{cr} was added because Test Matrix B demonstrated higher amplitudes in this bulk pressure region at higher ΔT s. The results for this set of tests is shown in Figure 3.21.

Table 3.5.: Test Matrix E: Pumping Tests at $\Delta T = 134K$

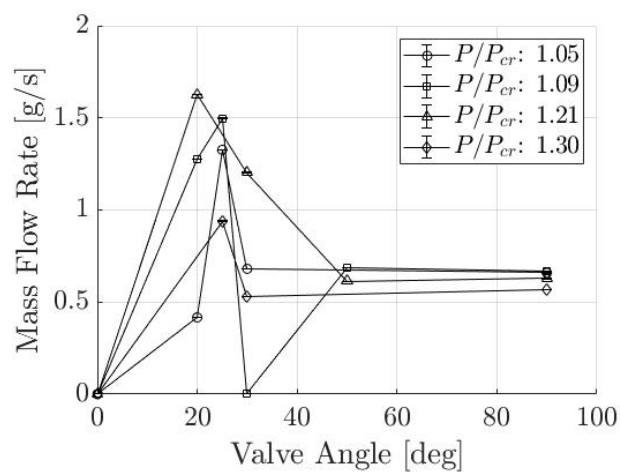
	1.05	1.10	1.20	1.3	P/P_{cr}
	2.77	2.90	3.17	3.43	P_{bulk} (MPa)
0	110	116	122	127	
20	111	117	124	0	
25	115	118	0	128	
30	112	119	123	129	
50	0	120	125	0	
90	113	121	126	130	
Valve Angle (deg)					



(a) Pressure amplitude with varying valve angle



(b) Frequency with varying valve angle



(c) Mass flow rate with varying valve angle

Figure 3.21. Experimental results obtained from Test Matrix E of pumping assessment

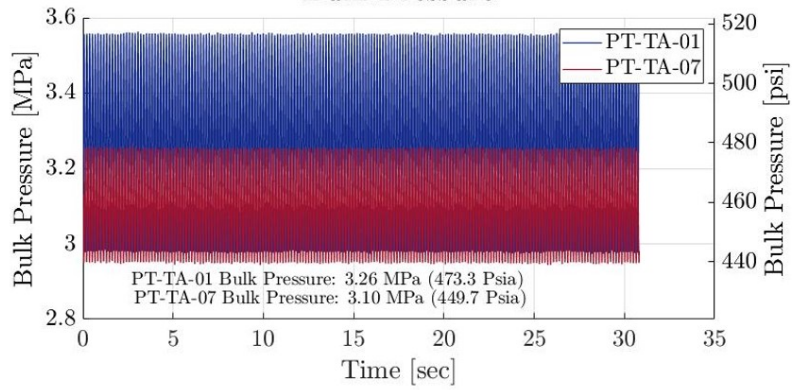
These tests showed that there is an optimal flow area which allows some of the fluid to be tapped off without taking away all of the acoustic energy (Figure 3.20c). This showed promising results, and demonstrated that there are four distinct regions of operation.

First, the valve is closed (Figures 3.22a & 3.22b) and demonstrates the same thermoacoustic behavior seen in Test Matrices B and C. When the valve is opened slightly (Figures 3.22c & 3.22d), the system generates a self sustained flow while still maintaining a significant pressure amplitude. The PSD plots show that a low-frequency response of approximately .06 Hz begins to emerge, as there is more "noise" in the PSD plot in the frequencies lower than the thermoacoustic frequency when the valve is opened. As the valve is opened further, there is a specific flow area where there is just enough acoustic energy tapped off such that the flow is periodically quenching the thermoacoustic response and then starting up again. This creates a cycle of pressure and mass flow rate spikes, deemed a "chugging" response.

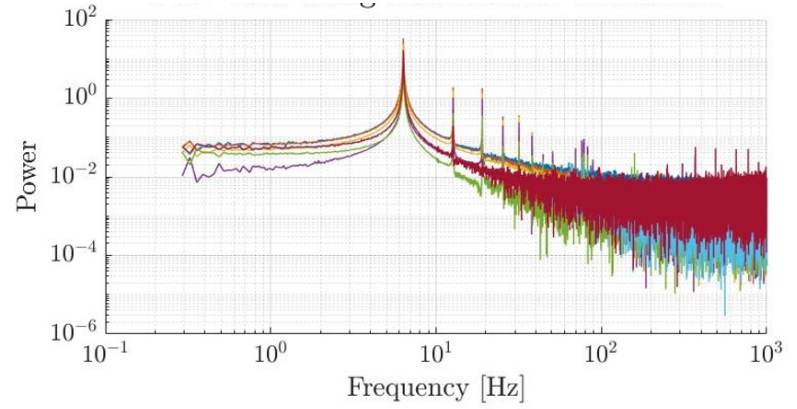
In this mode of operation, the PSD plot (Figure 3.21e) shows that this .06 Hz frequency is stronger than the 5 Hz thermoacoustic frequency. In this mode of operation, there are also temperature spikes in the stack due to the fact that there is a jet of fluid periodically issuing into the hot side cavity. Figure 3.22 compare the temperature histories and mass flow rate histories of tests 123 and 124.

It is possible that this periodic injection of cold fluid could actually be helping the heat transfer in the stack and allow a higher mass flow rate. When comparing the mass flow rate histories of Tests 124 and 123, Test 123 has a significantly higher peak mass flow rate, but a lower average mass flow rate. This demonstrates that the region of sustained mass flow rate is optimal for energy extraction.

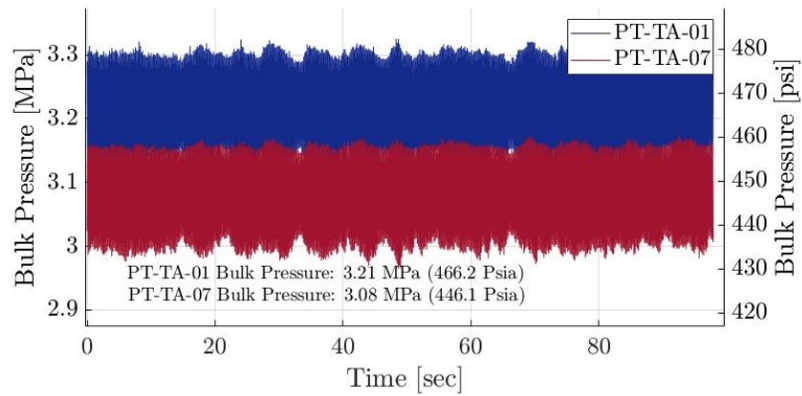
When the "chugging" response is achieved, any increase in flow area beyond this point will produce a poor thermoacoustic response (Figure 3.21g & 3.21h). In this region of operation, the flow area is high enough such that the mass flow takes away too much energy from the thermoacoustic response, and the pressure amplitude is dropped significantly, thus dropping the mass flow rate.



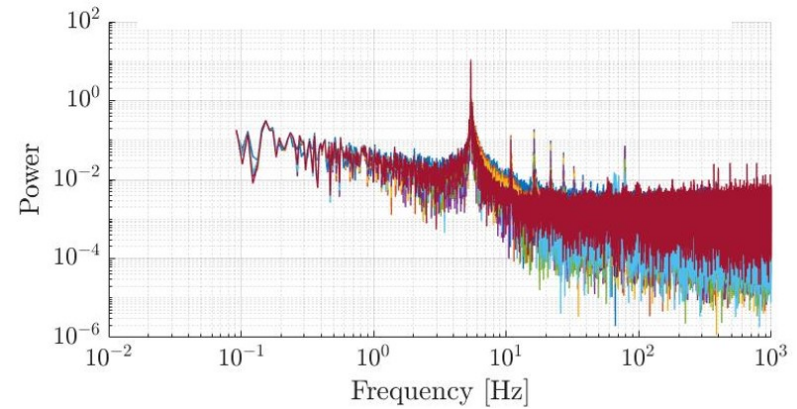
(a) Valve Closed - Bulk Pressure



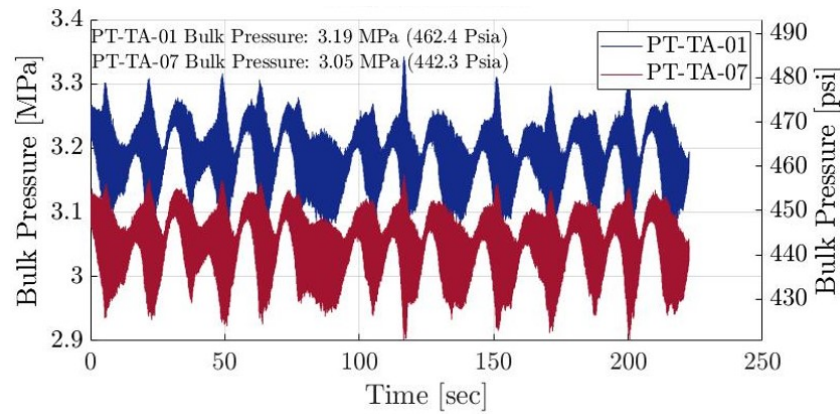
(b) Valve Closed - PSD Plot



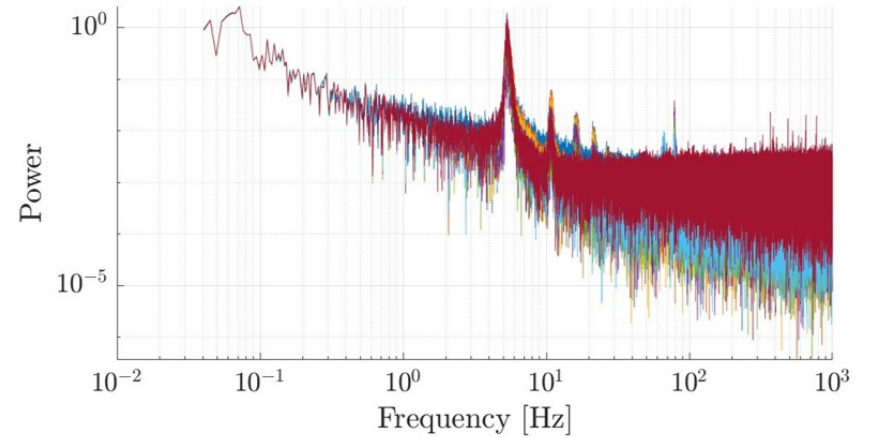
(c) Sustained Thermoacoustic Response - Bulk Pressure



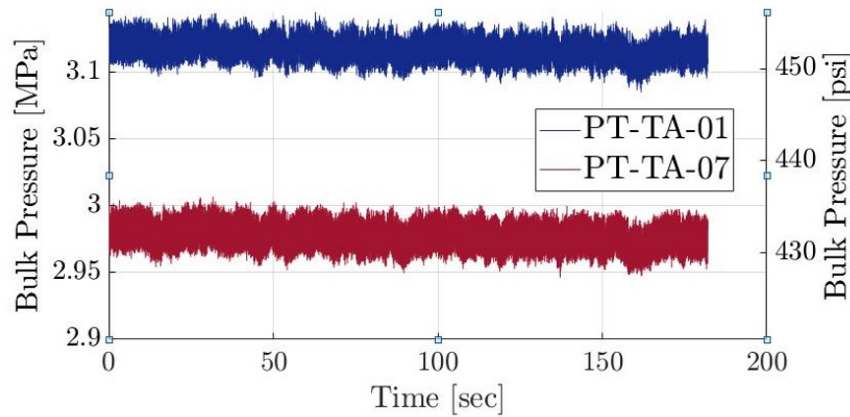
(d) Sustained Thermoacoustic Response - PSD Plot



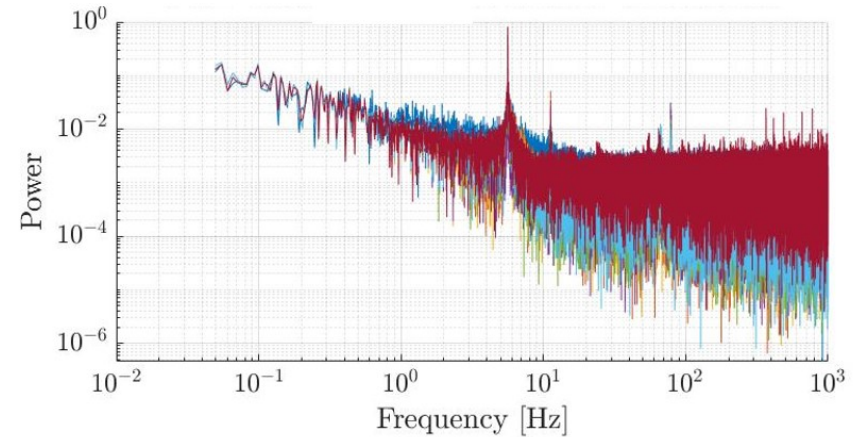
(e) Chugging response - bulk pressure



(f) Chugging response - PSD plot

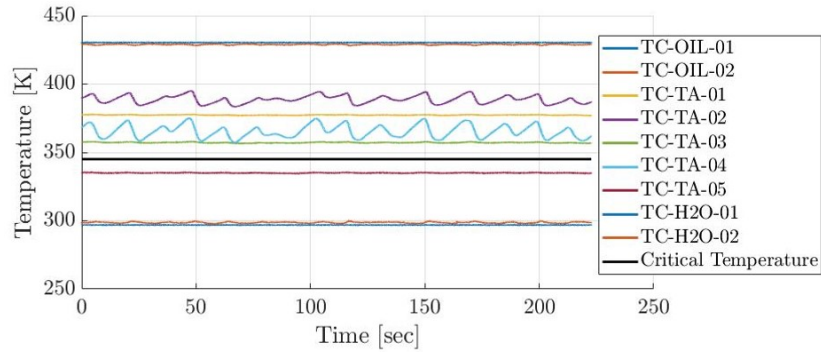


(g) Poor thermoacoustic response - bulkp pressure

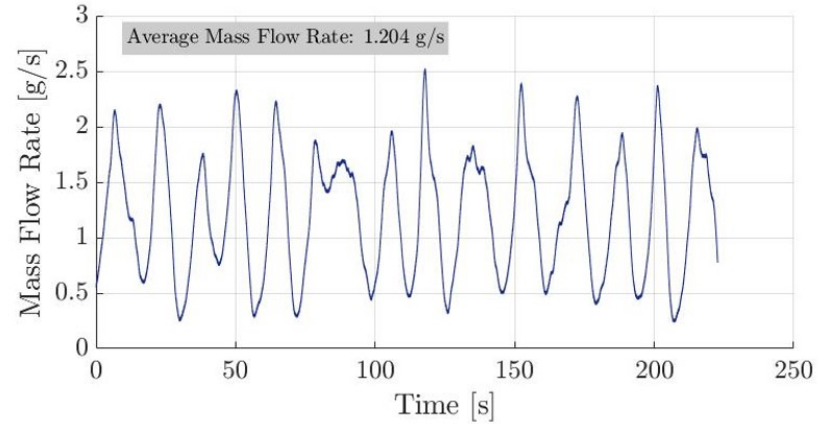


(h) Poor thermoacoustic response - PSD plot

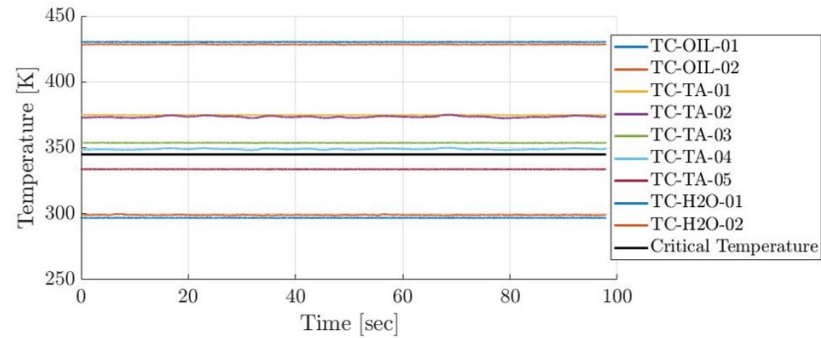
Figure 3.21. Progression of pressure behavior as fluid is recirculated. The example shown here is for $\Delta T = 134K$ and $P/P_{cr} = 1.2$.



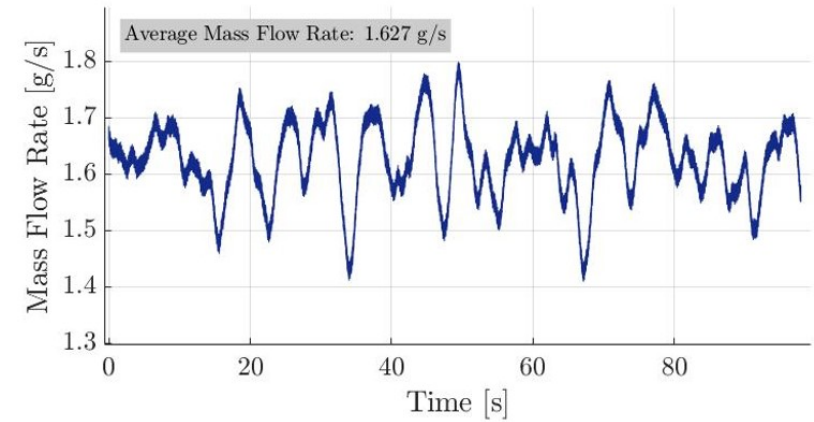
(a) Chugging response - system temperatures



(b) Chugging response - mass flow rate



(c) Sustained thermoacoustic response - system temperatures



(d) Sustained thermoacoustic response - mass flow rate

Figure 3.22. Comparison of temperature and mass flow rate of chugging response and sustained thermoacoustic response to demonstrate fluid jet injection into hot side cavity.

3.5.3 Test Matrix F: Pumping Tests at $\Delta T = 150K$

Test matrix F was conducted at $\Delta T = 150K$, and this produced the highest mass flow rates, as expected due to more thermal energy input. In an effort to increase the resolution on the valve angle, the method of angle measurement was switched to an imaging method, shown below. For each test, the valve was moved in as small of an increment as possible, and the valve angle was imaged and determined afterwards. This allowed for more data points to be collected in the region of sustained thermoacoustic response.



Figure 3.23. Picture demonstrating valve imaging method

Test Matrix F is shown in Table 3.6, and the test results are shown in Figure 3.24. Test Matrix F demonstrated the same wave behavior progression as Test Matrix E. In this set of tests, more data points were able to be collected, allowing for a higher resolution on any trends that might be seen. Once again, sustained thermoacoustic response and maximum flow rate capabilities are seen in the range of 20-30° valve angles. Additionally, the frequency is seen to drop with the opening of the valve.

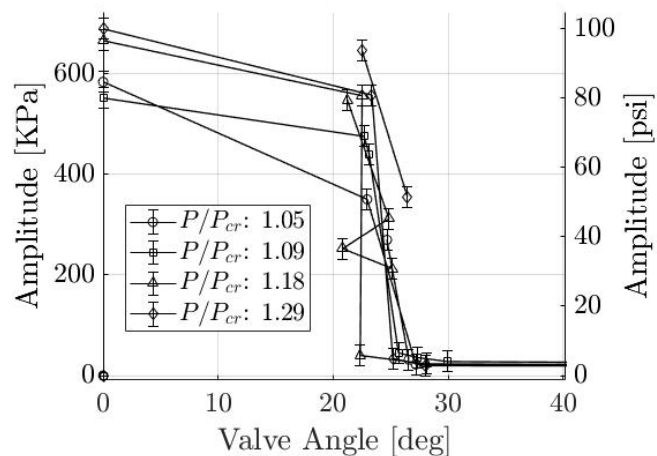
It should be noted that with the resonator length of 178 cm, test 160 achieved a pressure amplitude of 690 KPa (100 psi) at $P/P_{cr} = 1.3$ and $\Delta T = 150 K$ in the

valve close state, thus giving the highest recorded pressure amplitude for this testing campaign.

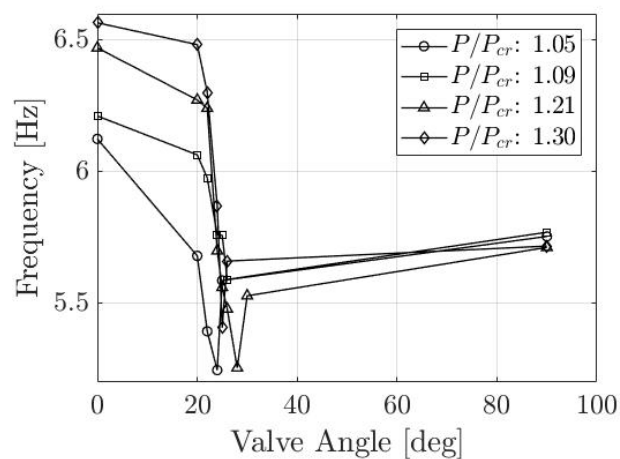
Table 3.6.: Test Matrix F: Pumping Tests at $\Delta T = 150K$

	1.05	1.10	1.20	1.3	P/P_{cr}
	2.77	2.90	3.17	3.43	P_{bulk} (MPa)
0	131	144	151	160	
20	132	145	152	165	
22	167	147	156	161	
24	168	146	157	166	
25	133	148	158	162	
26	-	149	153	163	
28	-	-	159	-	
30	-	-	154	-	
90	134	150	155	164	

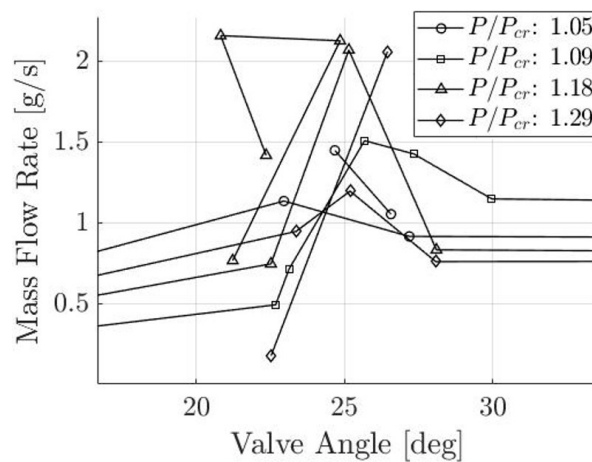
Valve Angle (deg)



(a) Pressure amplitude with varying valve Angle



(b) Frequency with varying valve angle



(c) Mass flow rate with varying valve Angle

Figure 3.24. Experimental results obtained from Test Matrix 5 of pumping assessment.

3.5.4 Assessment of Power Extraction

While plots for mass flow rate vs valve angle provide a qualitative history of the testing done, valve angle is not quantitatively reliable, as there is not an uncertainty that can be assigned to this parameter. Figure 3.25 shows the mass flow rate obtained from all data collected from Test Matricies D, E, and F, plotted against pressure amplitude. This provides a known and manageable uncertainty to compare results. Error bars on both mass flow rate and pressure amplitude are included, although the error on the mass flow rate is the largest at $2.4E-3$ g/s, and cannot be seen on the chart.

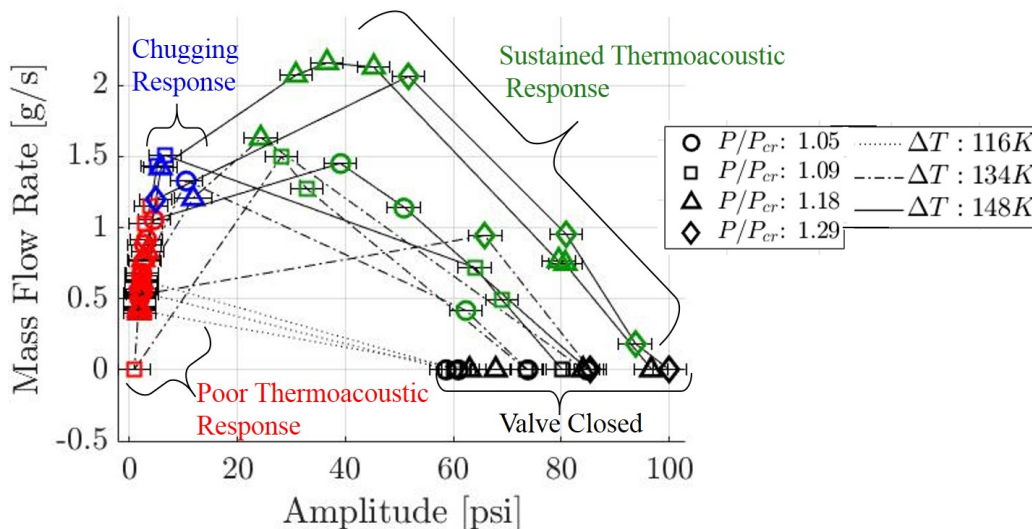


Figure 3.25. Mass flow rate vs pressure amplitude for all tests conducted in test Matricies 3,4,5. Line style indicates specified ΔT , marker shape indicates specified bulk pressure, and color indicates region of operation.

Figure 3.25 demonstrates that as the valve opens, the mass flow has a peak operational point in the region of sustained thermoacoustic response. To demonstrate the ability of the system to pump fluid, the data is represented in Figure 3.26 as pumping power vs acoustic power used. Pumping power, \dot{W}_{pump} , is given by Equation 3.1.

$$\dot{W}_{pump} = \frac{\dot{m}P}{\rho} \quad (3.1)$$

Here, \dot{m} is the mass flow rate measured by the Coriolis flow meter, P is the peak-to-peak pressure amplitude, and in this system represents the pressure drop across the pump. Finally, ρ is the fluid density measured by the Coriolis flow meter. In the recirculation line, the fluid is a liquid and has an average measured density of 1364 kg/s with a variation of ± 13 kg/s. The percentage of acoustic power used is obtained by Equation 3.2

$$\text{Percent Acoustic Power Used} = 1 - \left(\frac{P}{P_{max}}\right)^2 \quad (3.2)$$

Where P_{max} is the pressure amplitude at the valve-close condition, and P is the pressure amplitude as the valve opens. Because acoustic power is proportional to P^2 , Equation 3.2 represents the percentage of acoustic power that has been taken from the acoustic wave and used to create circulation in the system.

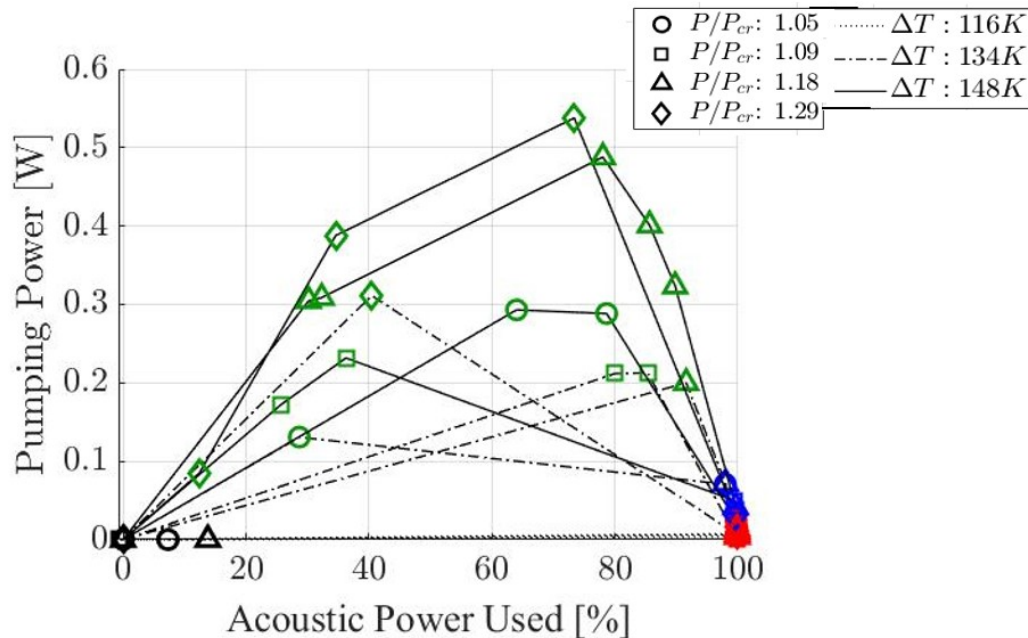


Figure 3.26. Pumping power vs percentage of acoustic power used for all tests conducted in Test Matrices D, E, and F.

Figure 3.26 is informative in demonstrating that a peak pumping is observed when approximately 73% of the available acoustic power is taped off. To demonstrate the variation in pumping ability with bulk pressure and ΔT , Figure 3.27 is presented.

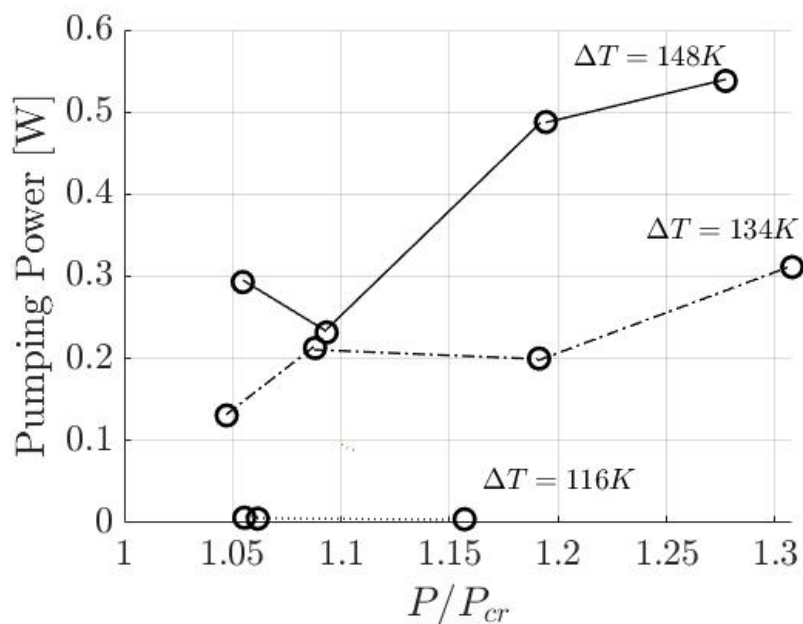


Figure 3.27. Pumping power vs bulk pressure for peak power obtained at each ΔT and bulk pressure condition.

Figure 3.27 was created by taking the peak power for each ΔT and bulk pressure tested. These trends exhibit a pattern which follows the pressure amplitude chart (Figure 3.8b), demonstrating that power extraction capability scales with acoustic pressure amplitude.

4. CONCLUSIONS AND FUTURE WORK

The goal of this research was to characterize the thermoacoustic response of transcritical R-218 and assess its feasibility of energy extraction and waste heat removal. This objective was met, as the behavior of the pressure amplitude and frequency was measured for a range of bulk pressures and temperature gradients. Transcritical R-218 is feasible to use for energy extraction and heat removal because recirculation tests demonstrated that the fluid can recirculate while still maintaining thermoacoustic pressure amplitude.

4.1 Summary of Results

The thermoacoustic response was characterized at seven different bulk pressures, ranging from $0.9 P/P_{cr}$ to $1.3 P/P_{cr}$ and five different ΔT s, ranging from 79 K to 150 K. This characterization was done in a closed rig without any energy extraction, and the highest pressure amplitude achieved up to 690 KPa (100 psi). To the author's knowledge this is the highest amplitude thermoacoustic wave ever produced in waveforms that do not include combustion. Overall, the amplitude of the instability grew with increased input energy as inferred by ΔT supplied to the thermoacoustic stack. For a given resonator configuration, the frequency of the instability varied only about 28% over the pressure and temperature ranges studied.

Additionally, the effect of resonator length on the thermoacoustic response was characterized. The thermoacoustic response was measured at five different resonator lengths varying from 100 cm to 200 cm at three different bulk pressures. The results of these tests demonstrated that the pressure amplitude was maximized at a resonator length of 179 cm. The reason for this is that the increased resonator length decreased the frequency, allowing for a longer thermal diffusion time inside the stack. It is

presumed that the amplitude peaked at the point where viscous losses in the resonator outweighed the benefit of lowered frequency.

Finally, the capability for energy extraction was assessed by opening the fluid to a recirculation line that connected the unheated end of the resonator to the hot side cavity. The recirculation line was installed with two check valves and a Coriolis flow meter. The check valves allowed the pressure amplitude to create a self-sustained circulation, and the Coriolis flow meter measured the mass flow rate and density of the fluid. Tests were conducted by opening a hand valve in small increments at a range of bulk pressures and ΔT s. The results of these tests demonstrated the ability for energy to be extracted from the fluid while still maintaining a sustained thermoacoustic response. The data showed that the peak power output (in terms of recirculated fluid flowrate) is obtained when 73% of the available acoustic power is extracted.

4.2 Future Work

4.2.1 Energy Extraction Options

In the literature review, several methods for energy extraction were discussed. The future work for this project should be focused on designing a system that can extract energy for conversion to electricity with the thermoacoustic response characterized in this testing campaign. Several options for energy extraction methods have been brainstormed. All options presented are capable of being interfaced with the current hardware.

The first option is a piston system attached to a linear encoder (Figure 4.1). The piston system has an advantage that Resonator Section 3 was designed to interface with a piston system, so the existing hardware could be used for this future work. The disadvantages of a piston system are that they have high friction and require dynamic seals, which are likely to leak. This could cause issue especially in a long-term solution.

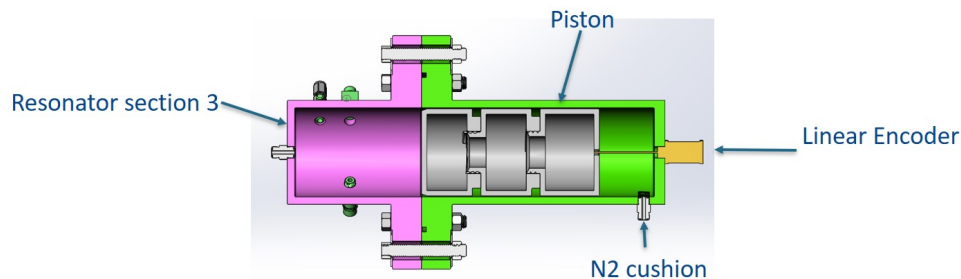


Figure 4.1. Piston system concept

The next option would be to install a flexible membrane at the end of the resonator (Figure 4.2). Like the piston, the membrane would also be attached to a linear encoder. The advantages of a flexible membrane over a piston is that there would not be frictional losses from the sliding seals in the piston. This would also allow the membrane to seal easier than the piston. The disadvantages of this concept is that the impedance of the membrane would need to match the resonance on the wave, so a membrane likely could only work for one setting. Additionally, the implementation of an alternator would still require dynamic seals.

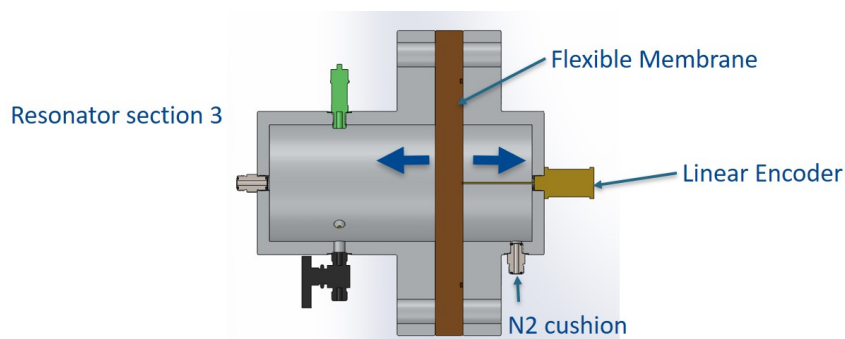


Figure 4.2. Flexible membrane concept

In an effort to remove frictional losses, one concept that emerged was the frictionless piston, or "buoy system". This piston, (Figure 4.3) uses flexure bearings to allow the piston to move back and forth without any dynamic sealing. This has the advantage that it is a constant volume system, and that there are no frictional losses from

piston seals. The disadvantage is that because fluid is traveling around and behind the piston, there could still be significant viscous losses. In this concept, the piston would be attached to a linear encoder or alternator, as in the flexible membrane and piston concepts.

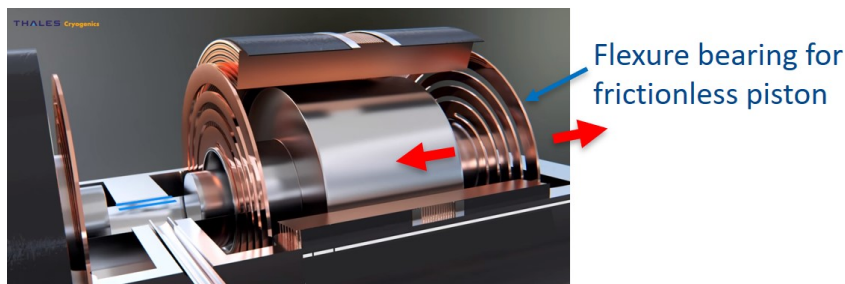


Figure 4.3. Frictionless piston, image from Thales Cryogenics

Finally, a magnetic bi-directional turbine concept was generated (Figure 4.4). In this concept, the turbine would be placed at the pressure node, in the middle of the resonator. The rotor would have magnetic blades, and the entire system would be in an enclosure with copper coils around the outside. This would allow a current to be induced by the rotation of the turbine blades. The attractive feature of this concept is that it would eliminate any need for dynamic sealing. A potential disadvantage is that for long term use, the system would likely be completely enclosed and this would make repairs difficult. The bi-directional turbine system likely offers the most promise and is recommended for future work.

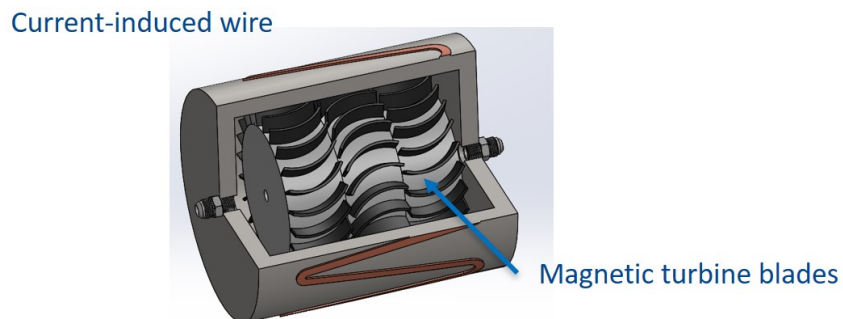


Figure 4.4. Bi-directional turbine concept

4.2.2 Generation 3 Rig

The Gen. 3 rig will likely employ a revised heat exchanger design. On the Gen. 2 rig, the microtubes on the heat exchanger were secured with epoxy to allow for the smallest possible microtube diameter. This made the system delicate, placing a temperature and pressure limitation on the system. The goal for the revised heat exchanger is to make a more robust design at the expense of microtube diameter. Having a larger microtube diameter will allow for the plates to be laser welded instead of epoxied. Because the microtube diameter will be larger in the Gen. 3 rig, the resonator will need to be longer to allow for more thermal diffusion time. Dr. Migliorino sized a notional Gen. 3 rig design for 0.457 mm microtubes. Table 4.1 shows a comparison of major dimensions and predicted outputs for the Gen. 3 rig vs the Gen. 2 rig.

Table 4.1.: Gen. 2 and Gen. 3 Rig Comparison

	Gen. 2	Gen. 3
pore diameter	.211 mm	.457 mm
porosity	12.30 %	28.42 %
hot side cavity length	2.03 cm	2.54 cm
stack length	6.10 cm	12.7 cm
HHX length	2.03 cm	2.54 cm
CHX length	2.03 cm	2.54 cm
Res. 1 length	5.08 cm	2.54 cm
Res 2 length	203.2 cm	254 cm
Res 3 length	15.2 cm	38.1 cm
D1	2.35 cm	3.84 cm
D2	0.457 cm	0.762 cm
D3	10.7 cm	30.48 cm

4.3 Lessons Learned

Several improvements can be made in moving forward with testing. First, alternate methods for measuring efficiency need to be evaluated. The intended method of measuring the energy balance with thermocouples placed on the inlet and outlet of

the heating and cooling fluids did not work. This was because the ΔT across each fluid was only about 4 K, which was approximately half of the thermocouple uncertainty range. For this reason, uncertainty on ΔT measurements across the heating and cooling fluids was over 100%. Uncertainty can be reduced by increasing the oil ΔT , but in doing so the ability to provide a linear temperature gradient along the stack may be compromised.

In the case that a Gen. 3 heat exchanger is designed, the author would recommend doing more analysis and testing of the limitations of the heat exchanger. Because the heat exchanger was a custom-made part, the pressure limitations were not known, and this information is necessary for both long-term testing and for safety. If possible, the author would recommend working with the manufacturer to test a Gen. 3 heat exchanger to failure. Additionally, in the event that higher pressures are going to be tested in the future, the author would recommend the use of stainless steel for construction of pressure vessels instead of aluminum.

Additionally, the author would not recommend the use of the Viton tubing used for the oil system. Although the tubing met the material compatibility and temperature requirements, it still failed at the highest temperature because the weight of the tubing caused stress at the hose clamp, and the high temperature weakened the tubing to failure. In the future, a braided high-temperature tubing is recommended.

The cooling system should be improved in future testing, the water supply was subjected to large fluctuations in outside air temperature, changing test conditions. Originally, the cooling method was an enclosed system with a water pump, but this was switched because the pump had trouble accommodating the large area restriction imposed on the flow by the microtubes. In the future, a larger pump and reservoir should be purchased, or a cooling fluid bath should be purchased, similar to the heated oil bath.

Finally, the method of using a hand valve to meter flow area was not a good method for experimentation because it did not provide quantitative measurements that had a reasonable amount of uncertainty. It is unlikely that pumping tests will be

continued in the future, but in the event that they are, the author would recommend the use of a computer-controlled regulator to meter flow area.

REFERENCES

- [1] Daniel Fritsche. *Origin and Control of Thermoacoustic Instabilities in Lean Premixed Gas Turbine Combustion*. PhD thesis, Swiss Federal Institute of Technology, 2005.
- [2] Dayle Alexander, Mario Tindaro Migliorino, Stephen Heister, and Carlo Scalo. Numerical and experimental analysis of a transcritical thermoacoustic prototype. In *2018 Fluid Dynamics Conference*, page 3536, 2018.
- [3] James R. Belcher, William Slaton, Richard Raspet, Henry E. Bass, and Jay Lightfoot. Working gases in thermoacoustic engines. *The Journal of the Acoustical Society of America*, 105:2677–84, 06 1999.
- [4] Dayle Alexander. Experimental study of a standing-wave transcritical thermoacoustic device. Master’s thesis, Purdue University, August 2018.
- [5] Tim Edwards. Usaf supercritical hydrocarbon fuels interests. In *31st Aerospace Sciences Meeting*, page 807, 1993.
- [6] H.K. Wiest and S.D. Heister. Experimental study of gas turbine combustion with elevated fuel temperatures. *Journal of Engineering for Gas Turbines and Power*, 136, 12 2014.
- [7] Stephen D. Heister and Steven Hunt. Thermoacoustic oscillations in supercritical fuel flows. In *12th International Energy Conversion Engineering Conference, IECEC 2014*, 07 2014.
- [8] C. Soundhaus. Ueber die schallschwingungen der luft in erhitzten glasroehren und in gedeckten pfeifen von ungleicher weite. *Annalen der Physik*, 1850.
- [9] John William Strutt and Baron Rayleigh. *The Theory of Sound*. MacMillan and Co., 1877.
- [10] J.R. Clement and J. Gaffney. Thermal oscillations in low temperature apparatus. *Advances in Cryogenic Engineering*, 1960.
- [11] K. T. Feldman. Review of the literature on sondhauss thermoacoustic phenomena. *J. Sound Vib.*, 7:71, 1968.
- [12] W.A. Marrison. Heat-controlled acoustic wave system, 1958. U.S. Patent No. 2,836,033.
- [13] D. L. Gardner and G. W. Swift. A cascade thermoacoustic engine. *The Journal of the Acoustical Society of America*, 114(4):1905–1919, 2003.
- [14] N. Rott. Damped and thermally driven acoustic oscillations in wide and narrow tubes. *Z. Angew. Math. Phys.*, 20:230, 1969.

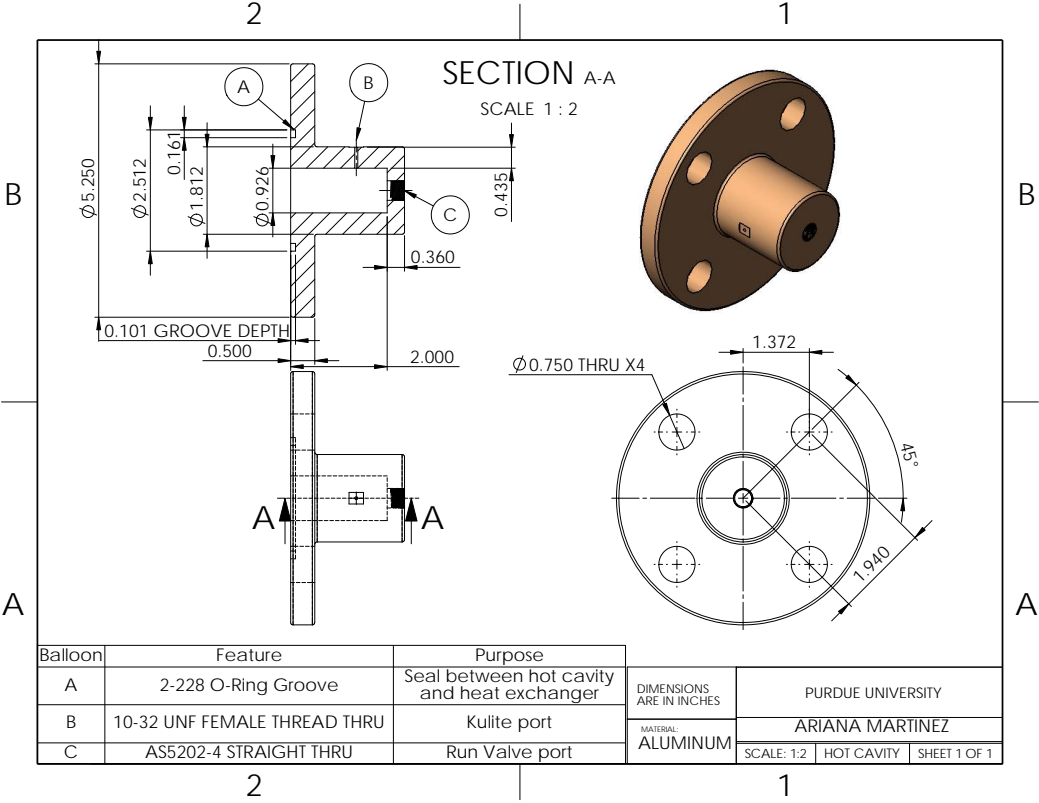
- [15] N. Rott. Thermally driven acoustic oscillations, part iii: Second-order heat flux. *Z. Angew. Math. Phys.*, 26:43, 1975.
- [16] N. Rott. Thermoacoustics. *Adv. Appl. Mech.*, 20:135, 1980.
- [17] P. H. Ceperley. A pistonless stirling engine: The traveling wave heat engine. *J. Acoust. Soc. Am.*, 66:1508, 1979.
- [18] P.H. Ceperly. Traveling wave heat engine, 1977. U.S. Patent No. 4114380A.
- [19] S. Backhaus and G.W. Swift. A thermoacoustic stirling heat engine. *Nature*, May 1999.
- [20] G. W. Swift. Thermoacoustic engines. *The Journal of the Acoustical Society of America*, 84(4):1145–1180, 1988.
- [21] S. Backhaus and G.W. Swift. Thermoacoustic engines and refrigerators: a short course. *Acoustical Societies of America and Europe*, August 1999.
- [22] J. Callanan and M. Nouh. Optimal thermoacoustic energy extraction via temporal phase control and traveling wave generation. *Applied Energy*, 241:599–612, January 2019.
- [23] Michael Timmer, Kees de Blok, and Theo H. van der Meer. Review on the conversion of thermoacoustic power into electricity. *The Journal of the Acoustical Society of America*, 143:841, January 2018.
- [24] Huidong Li, Chuan Tian, and Z. Daniel Deng. Energy harvesting from low frequency applications using piezoelectric materials. *Applied Physics Reviews*, 1(4):041301, 2014.
- [25] J. Smoker, M. Nouh, O. Aldraihem, and A. Baz. Energy harvesting from a standing wave thermoacoustic-piezoelectric resonator. *Journal of Applied Physics*, 111(10):104901, 2012.
- [26] A. Thakker, J. Jarvis, and A. Sahed. Quasi-steady analytical model benchmark of an impulse turbine for wave energy extraction. *International Journal of Rotating Machinery*, September 2008.
- [27] Tae-Ho Kim, Manabu Takao, Toshiaki Setoguchi, Kenji Kaneko, and Masahiro Inoue. Performance comparison of turbines for wave power conversion. *International Journal of Thermal Sciences*, 40(7):681–689, 2001.
- [28] Nicola Delmonte, Davide Barater, Giuliani Francesco, Cova Paolo, and Buticchi Giampaolo. Review of oscillating water column converters. *IEEE Transactions on Industry Applications*, 52(2):1698–1710, March 2016.
- [29] Toshiaki Setoguchi and Manabu Takao. Current status of self rectifying air turbines for wave energy conversion. *Energy Conversion and Management*, 47:2382–2396, November 2005.
- [30] Kees de Blok, Pawel Owczarek, and Maurice-Xavier Francois. Bi-directional turbines for converting acoustic wave power into electricity. *PAMIR International Conference on Fundamental and Applied MHD*, 9:433–438, 2014.
- [31] Kees de Blok. Beyond acoustic to electric power conversion limits, October 2015.

- [32] Mike Bradfield. Improving alternator efficiency measurably reduces fuel costs. Technical report, Remy, Inc., 2008.
- [33] S. Backhaus, E. Tward, and M. Petach. Traveling-wave thermoacoustic electric generator. *Appl. Phys. Lett.*, 85:1085, 2004.
- [34] Yu Z., A. J. Jaworski, and S. Backhaus. Travelling-wave thermoacoustic electricity generator using an ultra-compliant alternator for utilization of low-grade thermal energy. *Appl. Energy*, 99:135, 2012.
- [35] H. Kang, P. Cheng, Z. Yu, and H. Zheng. A two-stage traveling-wave thermoacoustic electric generator with loudspeakers as alternators. *Appl. Energy*, 137:9, 2015.
- [36] Z. Wu, M. Man, E. Luo, W. Dai, and Y. Zhou. Experimental investigation of a 500 w traveling-wave thermoacoustic electricity generator. *Chin. Sci. Bull.*, 56:1975, 2011.
- [37] Z. Wu, W. Dai, M. Man, and E. Luo. A solar-powered traveling-wave thermoacoustic electricity generator. *Sol. Energy*, 86:2376, 2012.
- [38] Z. Wu, L. Zhang, W. Dai, and E. Luo. Investigation on a 1kw traveling-wave thermoacoustic electrical generator. *Appl. Energy*, 124:140, 2014.
- [39] Z. Wu, G. Yu, L. Zhang, W. Dai, and E. Luo. Development of a 3kw double-acting thermoacoustic stirling electric generator. *Appl. Energy*, 136:866, 2014.
- [40] T. Bi, Z. Wu, L. Zhang, G. Yu, E. Luo, and W. Dai. Development of a 5 kw traveling-wave thermoacoustic electric generator. *Appl. Energy*, 185:1355, 2017.
- [41] D. Sun, K. Wang, X. Zhang, Y. Guo, Y. Xu, and L. Qiu. A traveling-wave thermoacoustic electric generator with a variable electric r-c load. *Appl. Energy*, 106:377, 2013.
- [42] K. Wang, D. Sun, J. Zhang, Y. Xu, K. Luo, N. Zhang, J. Zou, and L. Qiu. An acoustically matched traveling-wave thermoacoustic generator achieving 750w electric power. *Energy*, 103:313, 2016.
- [43] K. Wang, S. Dubey, F. H. Choo, and F. Duan. Thermoacoustic stirling power generation from lng cold energy and low-temperature waste heat. *Energy*, 127:280, 2017.
- [44] M.T. Migliorino and C. Scalo. Transcritical thermoacoustic instability. *Journal of Fluid Mechanics*, 2018.
- [45] I. E. Idelchik. *Handbook of Hydraulic Resistance*. CRC Press, 3rd edition, 2003.
- [46] Thermo Fisher Scientific. *ADVANCED Series Heated Immersion Circulators / ARCTIC Series Refrigerated & Heated Bath Circulators / GLACIER Refrigerated Bath Circulator / SAHARA Series Heated Bath Circulators User Manual [EN]*, May 2015.
- [47] Erik Oberg, Franklin D. Jones, Holbrook L. Horton, and Henry H. Ryffel. pages 241,472,3038. Industrial Press Inc., 27 edition, 2004.

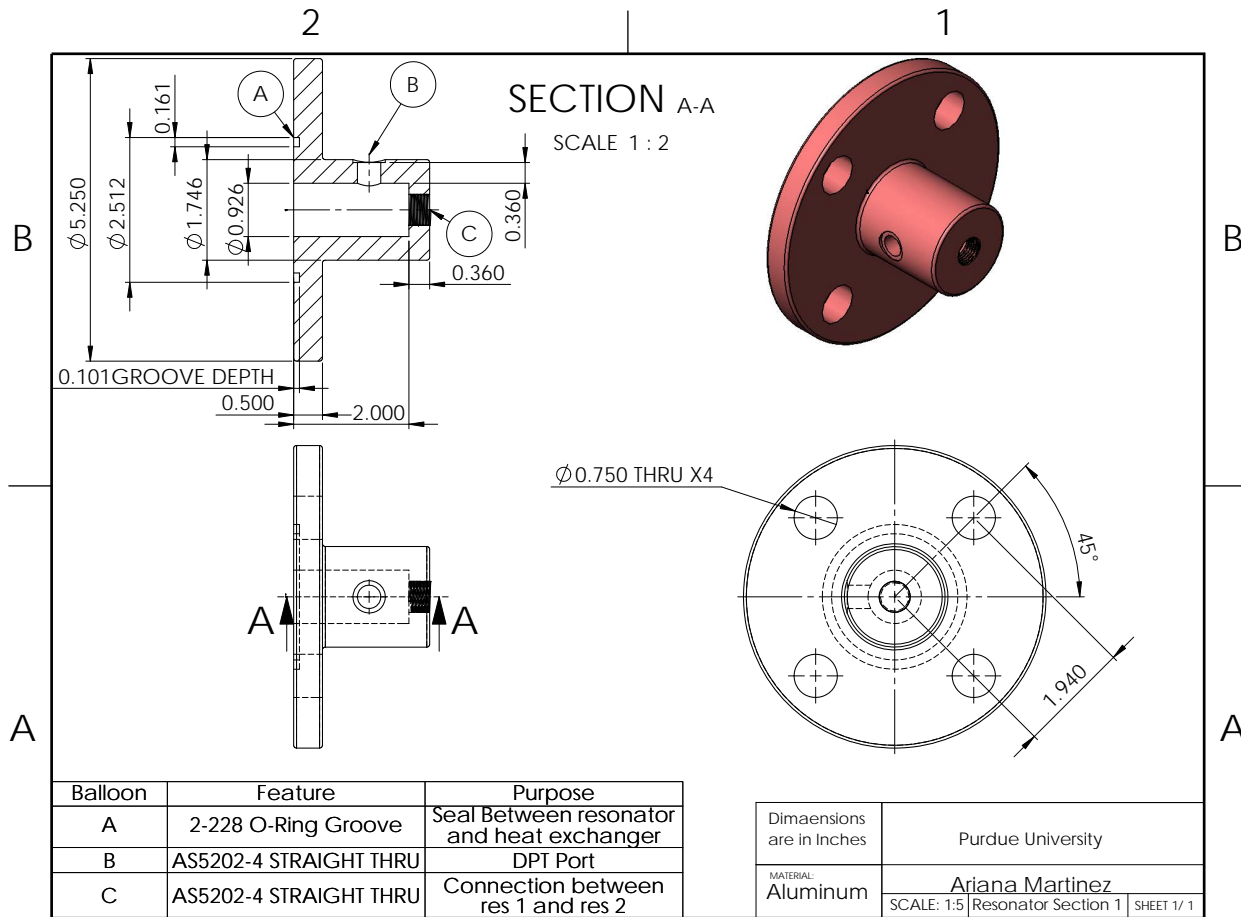
- [48] Frank P. Incropera and David P. DeWitt. John Wiley & Sons, second edition, 1981.
- [49] Waqar Khan. *Modeling of Fluid Flow and Heat Transfer for Optimization of Pin-Fin Heat Sinks*. PhD thesis, 2004.
- [50] WA Khan, JR Culham, and MM Yovanovich. Convection heat transfer from tube banks in crossflow: Analytical approach. *International journal of heat and mass transfer*, 49(25-26):4831–4838, 2006.
- [51] Warren C. Young and Richard G. Budynas. pages 128–129,193. McGraw-Hill, 7 edition, 2002.
- [52] Eric W. Lemmon, Mark O. McLinden, and Daniel G. Friend. Thermophysical properties of fluid systems.
- [53] Assessing experimental uncertainty-supplement to aiaa s-071a-1999, 2003.
- [54] Assessment of experimental uncertainty with application to wind tunnel testing, 1999.

A. Supplementary Material

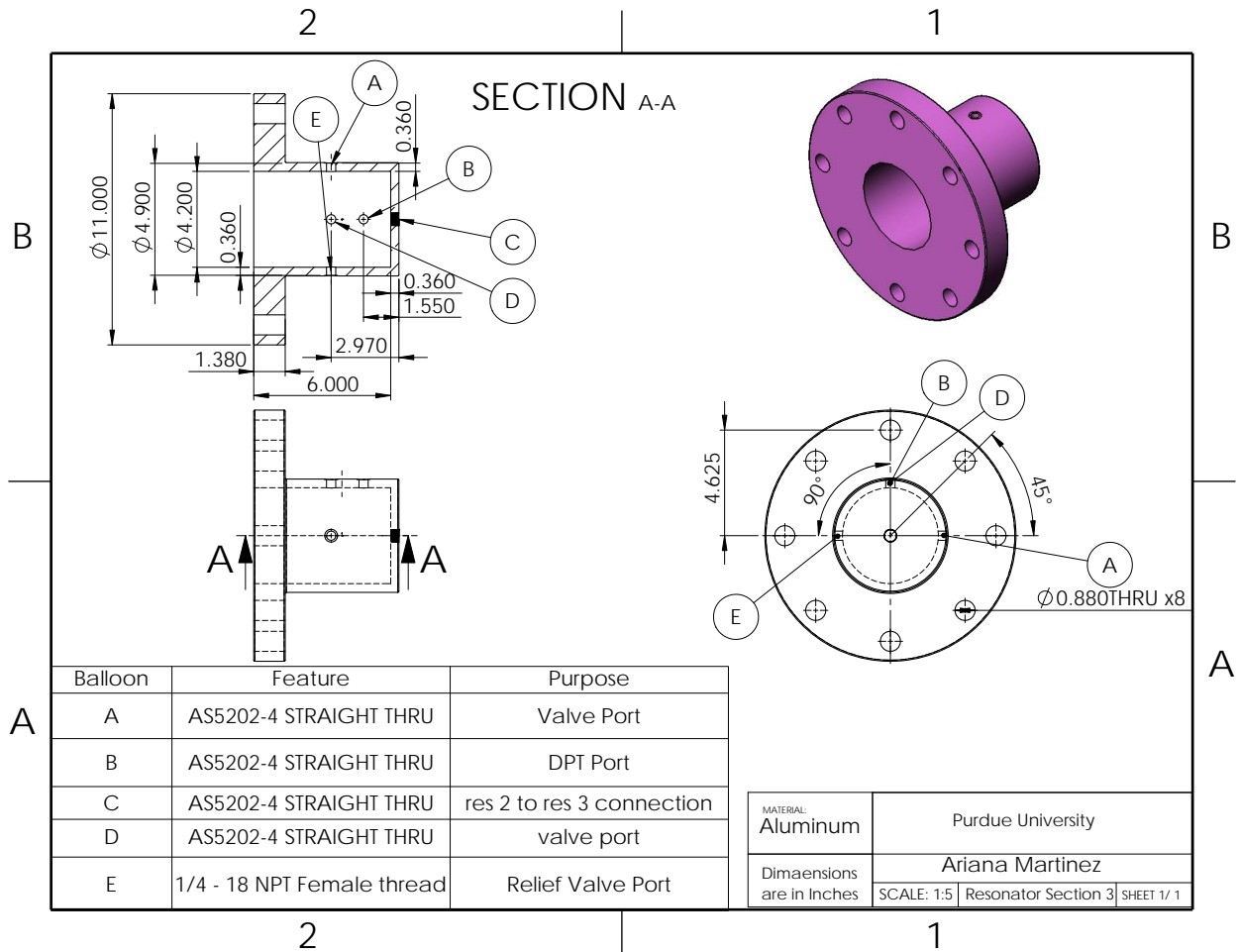
A.1 Hot Side Cavity Technical Drawing



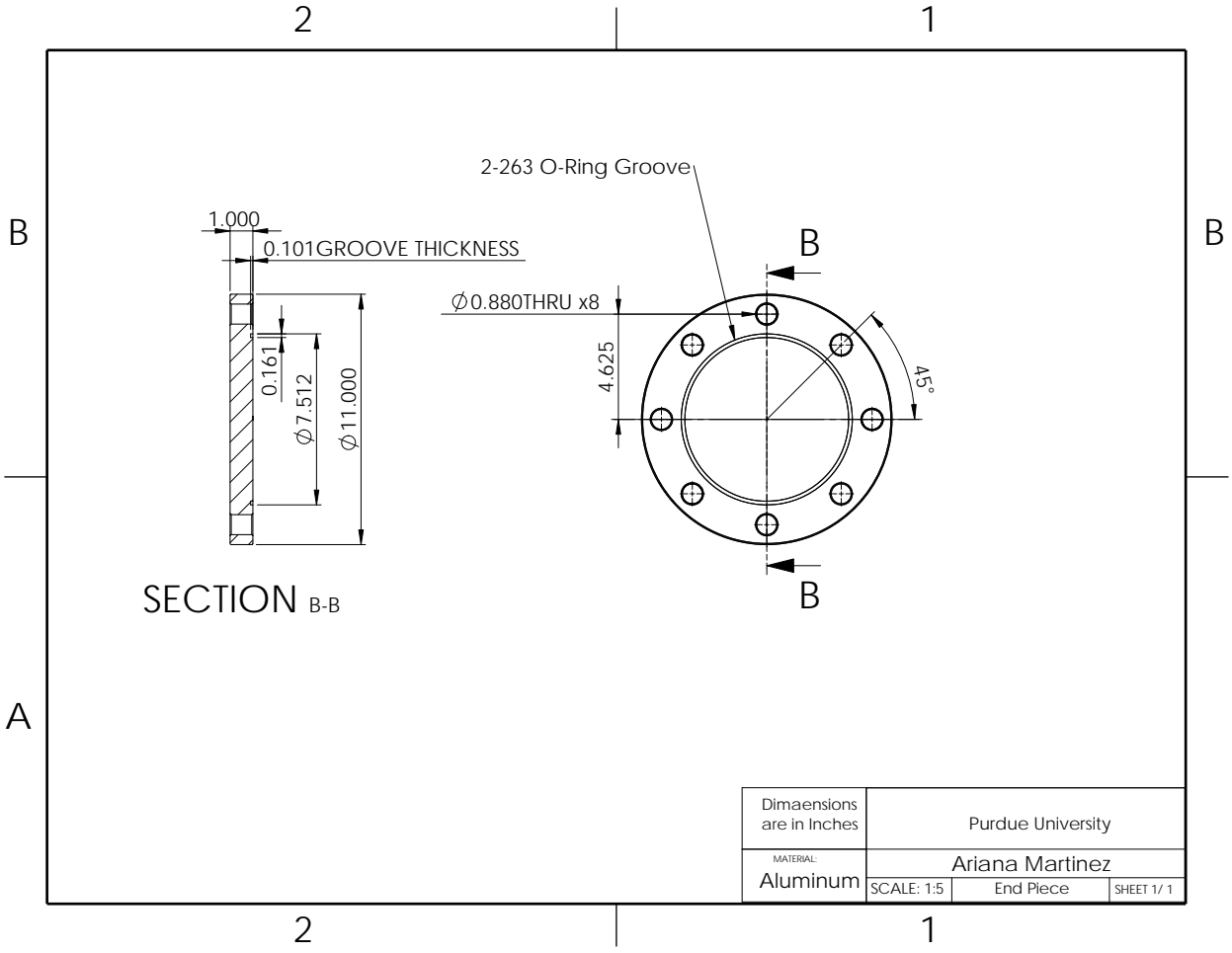
A.2 Resonator Section 1 Technical Drawing



A.3 Resonator Section 3 Technical Drawing



A.4 End Cap Technical Drawing



Dimensions are in Inches	Purdue University		
MATERIAL: Aluminum	Ariana Martinez		
SCALE: 1:5	End Piece	SHEET 1 / 1	

A.5 Duratherm G Technical Data Sheet

DURATHERM G

- Maximum temperature: 260°C / 500°F
- Flash point 248°C / 480°F
- Ideal for open bath systems
- Extreme oxidation resistance
- Non-toxic/non-hazardous
- Alternative to Ucon 500®
- Includes free fluid analysis and tech support



1 800 446 4910

www.durathermfluids.com

TEMPERATURE RATINGS

Maximum Bulk/Use Temp.	260°C	500°F
Maximum Film Temp.	287°C	550°F
Pour Point ASTM D97	-40°C	-40°F

SAFETY DATA

Flash Point ASTM D92	248°C	480°F
Fire Point ASTM D92	284°C	505°F
Autoignition ASTM E-659-78	373°C	690°F

THERMAL PROPERTIES

Thermal Expansion Coefficient	0.0679 %/°C	0.0377 %/°F
Thermal Conductivity	W/m K	BTU/hr F ft
38°C / 100°F	0.181	0.105
121°C / 250°F	0.173	0.100
260°C / 500°F	0.160	0.092
Heat Capacity	kJ/kg K	BTU/lb F
38°C / 100°F	1.976	0.472
121°C / 250°F	2.063	0.493
260°C / 500°F	2.207	0.528

PHYSICAL PROPERTIES

Appearance: clear liquid, very slight yellow tint		
Viscosity ASTM D445		
cSt at 40°C / 104°F	42.10	
cSt at 121°C / 250°F	5.16	
cSt at 260°C / 500°F	1.23	
Density ASTM D1298	kg/m ³	lb/ft ³
38°C / 100°F	920.28	57.46
121°C / 250°F	896.85	55.99
260°C / 500°F	857.61	53.54
Vapor Pressure ASTM D2879	kPa	psi
38°C / 100°F	0.20	0.04
121°C / 250°F	0.93	0.16
260°C / 500°F	3.40	0.51
Distillation Range ASTM D2887	10%	367°C (694°F)
	90%	513°C (957°F)

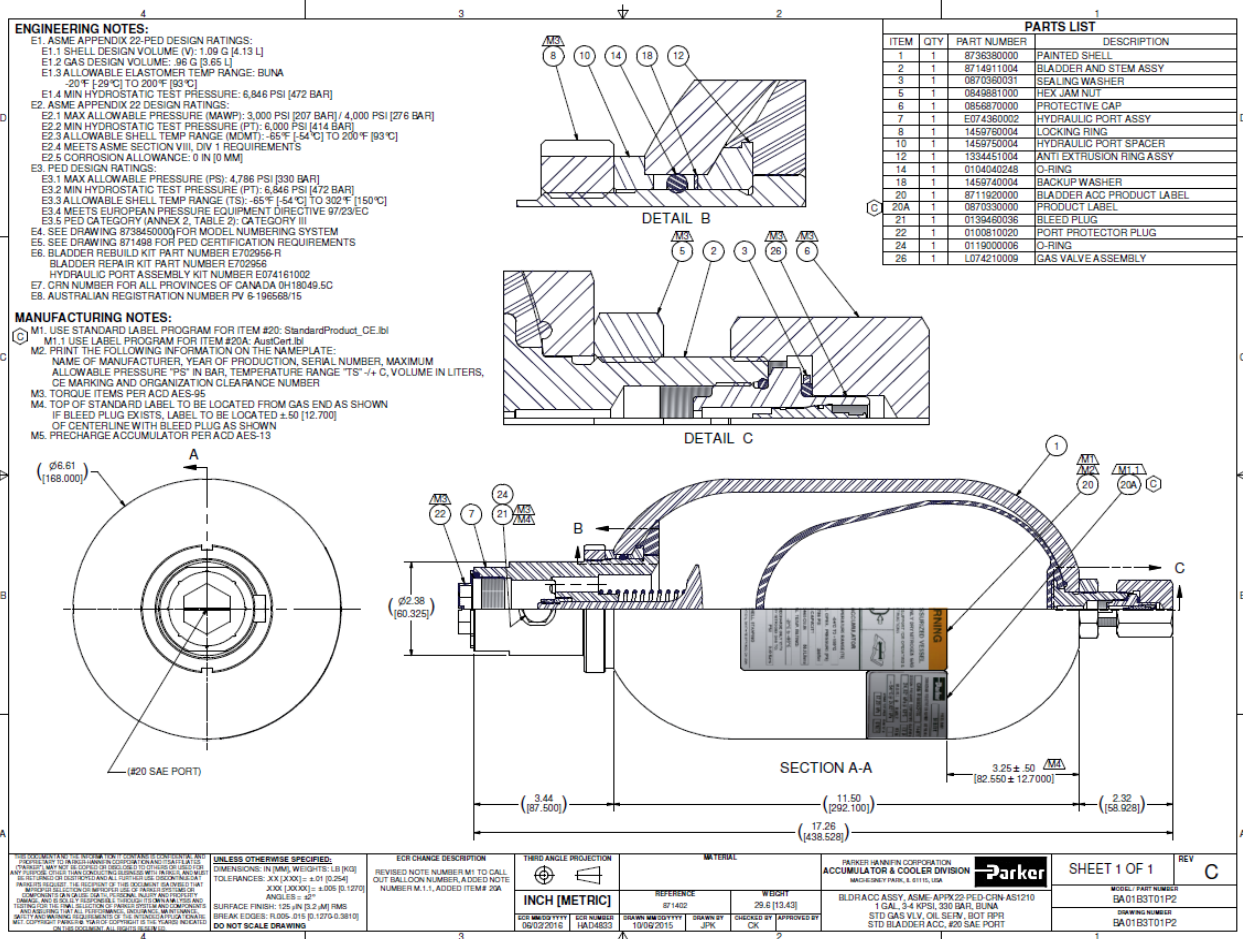
The values quoted are typical of normal production. They do not constitute a specification.

TEMPERATURE (Celsius)	DENSITY (kg/m ³)	KINEMATIC VISCOSITY (Centistoke)	DYNAMIC VISCOSITY (Centipoise)	THERMAL CONDUCTIVITY (W/m-K)	HEAT CAPACITY (kJ/kg-K)	VAPOR PRESSURE (kPa)
-40	942.31	19283.44	18170.94	0.189	1.895	0.00
-30	939.48	5429.06	5100.52	0.188	1.906	0.00
-20	936.66	1874.94	1756.18	0.187	1.916	0.00
-10	933.84	763.63	713.10	0.186	1.926	0.01
0	931.01	355.66	331.13	0.185	1.937	0.04
10	928.19	184.88	171.60	0.184	1.947	0.07
20	925.37	105.20	97.35	0.183	1.958	0.11
30	922.54	64.51	59.51	0.182	1.968	0.15
40	919.72	42.10	38.72	0.181	1.978	0.21
50	916.90	28.94	26.54	0.180	1.989	0.27
60	914.07	20.79	19.00	0.179	1.999	0.34
70	911.25	15.49	14.11	0.178	2.010	0.41
80	908.43	11.91	10.82	0.177	2.020	0.50
90	905.60	9.41	8.52	0.176	2.030	0.59
100	902.78	7.60	6.86	0.175	2.041	0.69
110	899.96	6.26	5.64	0.174	2.051	0.80
120	897.13	5.25	4.71	0.173	2.062	0.92
130	894.31	4.47	4.00	0.172	2.072	1.04
140	891.49	3.86	3.44	0.171	2.082	1.18
150	888.66	3.36	2.99	0.170	2.093	1.32
160	885.84	2.97	2.63	0.169	2.103	1.47
170	883.02	2.64	2.33	0.168	2.114	1.62
180	880.19	2.37	2.08	0.167	2.124	1.79
190	877.37	2.14	1.88	0.166	2.134	1.96
200	874.55	1.95	1.70	0.166	2.145	2.14
210	871.72	1.78	1.55	0.165	2.155	2.33
220	868.90	1.64	1.42	0.164	2.166	2.53
230	866.08	1.52	1.31	0.163	2.176	2.73
240	863.25	1.41	1.22	0.162	2.186	2.95
250	860.43	1.31	1.13	0.161	2.197	3.17
260	857.61	1.23	1.06	0.160	2.207	3.40

The values quoted are typical of normal production. They do not constitute a specification.

A.6 Bladder Accumulator Technical Drawing

132



A.7 Procedures



Zucrow Laboratories - Combustion Lab (ZL1-102)

Rolls-Royce Transcritical Thermoacoustic Engine Project

PROJECT: _____

DATE: _____

TEST CONDUCTOR: _____

PROJECT ENGINEER: _____

TEST OPERATOR(S): _____

DATA SYSTEM OPERATOR: _____

TC Test Conductor: In charge of all aspects of the test. Directs test operations through use of the test procedures.

TOP Test Operator: Performs all test stand related activities associated with loading propellants and pressurant gases. Receives instructions from the Test Conductor during operation of the test procedures.

DSO	Data System Operator: Responsible for the installation and operability of all instrumentation and controls consistent with the requirements for each test. Operates the computer control and data acquisition system during tests.
SAF	Site Safety: Responsible for insuring all test site safety equipment is in place and functioning properly. Is responsible for keeping the site clear of unauthorized personnel during test operations.
Rec	Reclamation
Ref	Refrigerant
Iso	Isolation
PG	Pressure Gauge
PT	Pressure Transducer
TC	Termocouple
RV	Relief Valve
MV	Manual Valve
MR	Manual Regulator
RP	Reclamation Pump
RM	Refrigerant Manifold
TA	Test Article

REQUIRED PPE: Safety Glasses

Attachments: Test Data Sheet; P&ID; Instrumentation List

SECTION 1: PRE-TEST SETUP									
Step #	Action By	Operation	Test Numbers						
0. Prepare Test Area									
1.001	SAF	PUT testing sign on door							
1.002	SAF	TURN ON testing light							
1.003	TOP	VERIFY cart wheels are locked							
1.004	DSO	CONNECT transducer cable to connector 0							
1.005	TOP	VERIFY all wiring is connected correctly							
1.006	TOP	VERIFY oil bath contains enough oil to submerge oil pump and heater							
1.007	TOP	ATTACH N2 flex hose to N2 Regulator (MR-N2-01)							
1.008	DSO	TURN ON 28V DC regulated power supply							
1.009	DSO	TURN ON 12V DC regulated power supply							
1.010	DSO	TURN ON Computer and login (pass: Purdue_Pete)							
1.011	DSO	OPEN LabVIEW							
1.012	DSO	START LabVIEW VI (run program)							
1.013	DSO	LOAD Config (data wiring) files: datawiring_TTE_pc.xlsx & datawiring_TTE_tc.xlsx in TTE folder							
1.014	DSO	VERIFY sampling rate 2 kHz							
1.015	DSO	START acquire all to see live data							
1.016	DSO	START the GUI schematic							
1.017	DSO	if ref is unloaded: ACQUIRE zeroing data for PT_TAs by clicking ACQUIRE ZEROING DATA							
1.018	DSO	if ref is unloaded: SAVE zero data							
1.019	DSO	if ref is loaded: LOAD zero data							
1.020	DSO	VERIFY all data channels are reading properly							
1.021	TOP	VERIFY all hoses and tubes connected (per P&ID)							
1.022	TOP	VERIFY Reclamation Pump Liquid Valve (RPV-R218-01) closed							
1.023	TOP	VERIFY Reclamation Pump Gas Valve (RPV-R218-02) closed							
1.024	TOP	VERIFY Reclamation Manual Liquid Valve (MV-R218-03) closed							
1.025	TOP	VERIFY Reclamation Manual Gas Valve (MV-R218-02) closed							
1.026	TOP	VERIFY Vacuum Iso Valve (MV-R218-04) closed							
1.027	TOP	VERIFY Fill Iso Valve (MV-R218-05) closed							
1.028	TOP	VERIFY Reclaim Iso Valve (MV-R218-06) closed							
1.029	TOP	VERIFY Circulation Line Close-Off Valve (MV-R218-10) open							
1.030	TOP	VERIFY Hot Side Run Valve (MV-R218-08) open							
1.031	TOP	VERIFY Cold Side Run Valve (MV-R218-09) open							
1.032	TOP	VERIFY Pressure Isolation Valve (MV-ISO-01) open							
1.033	TOP	VERIFY Vacuum Jacket Valve (MV-VAC-01) is closed							
1.034	TOP	VERIFY all valves closed on Refrigerant Manifold (RM-R128-01, RM-R218-02, RM-R218-03, RM-R218-04)							

1.035	TOP	VERIFY Oil Direction Control Valve (DCV-OIL-01) is in direction of oil pump (handle perpendicular to incoming flow)							
1.036	TOP	VERIFY Water Supply Valve (MV-H20-01) closed							
1.037	TOP	VERIFY N2 Iso Valve (MV-N2-02) closed							
1.038	TOP	VERIFY N2 Hammer Valve (MV-N2-03) closed							
1.039	TOP	VERIFY Nitrogen Regulator (MR-N2-01) is unloaded							
1.040	TOP	OPEN N2 Supply Valve (MV-N2-01)							
1.041	TOP	OPEN N2 Iso Valve (MV-N2-02)							
1.042	TOP	OPEN N2 Hammer Valve (MV-N2-03) (if system not already filled with refrigerant)							
1.043	TOP	IF REF ALREADY IN: SKIP to Section 2.1							
1. Vacuum Cycle									
1.100a	N/A	DO these steps if there isn't already refrigerant in the system (otherwise skip to Section 2)							
1.100b	N/A	WARNING: Vacuum pump gets hot during use							
1.100c	N/A	WARNING: Vacuum Pump may exhaust water/oil vapor until all is gone from lines							
1.100e	N/A	REFER to operation manual for oil replacement procedure if needed							
1.101	TOP	VERIFY all hoses and tubes connected (per P&ID)							
1.102	TOP	Verify Vacuum Pump is connected to Refrigerant Manifold (RM-R218-03)							
1.103	TOP	VERIFY Reclamation Pump Liquid Valve (RPV-R218-01) closed							
1.104	TOP	VERIFY Reclamation Pump Gas Valve (RPV-R218-02) closed							
1.105	TOP	VERIFY Reclamation Manual Gas Valve (MV-R218-02) closed							
1.106	TOP	VERIFY Reclamation Manual Liquid Valve (MV-R218-03) closed							
1.107	TOP	PLUG IN extention cord							
1.108	TOP	PLUG IN Vacuum Pump							
1.109	TOP	VERIFY exhaust cap removed							
1.110	TOP	CHECK oil level on vacuum pump							
1.111	TOP	FILL if low (should fill half of sight glass while running)							
1.112	TOP	TURN ON Vacuum Pump							
1.113	TOP	OPEN Vacuum Valve (RM-R218-03)							
1.114	TOP	RUN Vacuum Pump for about 1 minute to warm up							
1.115	TOP	OPEN Low Pressure Valve (RM-R218-01)							
1.116	TOP	OPEN High Pressure Valve (RM-R218-02)							
1.117	TOP	OPEN Reclamation Valve (RM-R218-04)							
1.118	TOP	CLOSE Reclamation Valve (RM-R218-04) after vacuuming for a few seconds							
1.119	TOP	OPEN Vacuum Iso Valve (MV-R218-04)							
1.120	TOP	OPEN Reclaim Iso Valve (MV-R218-06)							
1.121	TOP	OPEN Fill Iso Valve (MV-R218-05)							
1.122	TOP	IF Test Article Seal Was Broken: Open MV-ISO-01, MV-R218-08, MV-R218-09, MV-R218-10							

1.124	TOP	VACUUM until vacuum is reached (30 in Hg) on Low Pressure Gauge (PG-R218-05)							
1.125	TOP	VERIFY instrumentation is reading correct values							
1.126	TOP	CLOSE Reclaim Iso Valve (MV-R218-06)							
1.127	TOP	CLOSE Fill Iso Valve (MV-R218-05)							
1.128	TOP	CLOSE Vacuum Valve (RM-R218-03)							
1.129	TOP	CLOSE Low Pressure Valve (RM-R218-01)							
1.130	TOP	CLOSE High Pressure Valve (RM-R218-02)							
1.131	TOP	TURN OFF Vacuum Pump							
1.132	TOP	UNPLUG Vacuum Pump							
2. Refill from Rec Tank									
A.201	TOP	DO these steps to refill the test article with already reclaimed refrigerant							
A.202	TOP	DO these steps AFTER the entire rig and output side of Reclamation Pump have been vacuumed							
1.201	TOP	VERIFY all hoses and tubes connected (per Fill/Vacuum P&ID)							
1.202	TOP	VERIFY all valves closed on Refrigerant Manifold							
1.203	TOP	VERIFY Reclamation Pump Liquid Valve (RPV-R218-01) closed							
1.204	TOP	VERIFY Reclamation Pump Gas Valve (RPV-R218-02) closed							
1.205	TOP	VERIFY Reclamation Manual Liquid Valve (MV-R218-03) closed							
1.206	TOP	VERIFY Reclamation Manual Gas Valve (MV-R218-02) closed							
1.207	TOP	VERIFY Vacuum Iso Valve (MV-R218-04) closed							
1.208	TOP	VERIFY Fill Iso Valve (MV-R218-05) closed							
1.209	TOP	VERIFY Reclaim Iso Valve (MV-R218-06) closed							
1.210	TOP	VERIFY Hot Side Run Valve (MV-R218-08) open							
1.211	TOP	VERIFY Cold Side Run Valve (MV-R218-09) open							
1.212	TOP	VERIFY Pressure Isolation Valve (MV-ISO-01) open							
1.213	TOP	VERIFY Nitrogen Regulator (MR-N2-01) is unloaded							
1.214	TOP	OPEN N2 Hammer Valve (MV-N2-03)							
1.215	TOP	SET Nitrogen Regulator (MR-N2-01) to loading pressure ~80psig							
1.216	TOP	VERIFY High Pressure Tube (red tube) is connected to Rec Manual Liquid Valve (MV-R218-03)							
1.217	TOP	PLUG IN Extention cord							
1.218	TOP	OPEN High Pressure Valve (RM-R218-02)							
1.219	TOP	VERIFY Reclamation Pump is Plugged in							
1.220	TOP	OPEN Rec Tank Manual Liquid Valve (MV-R218-03)							
1.221	TOP	OPEN Reclamation Valve (RM-R218-04)							
1.222	TOP	OPEN Fill Iso Valve (MV-R218-05)							
1.223	TOP	OPEN circulation line Close-Off Valve (MV-R218-10)							
1.224	TOP	OPEN Rec Pump Gas Valve (RPV-R218-01)							
1.225	TOP	OPEN Rec Pump Gas Valve (RPV-R218-02)							
1.226	TOP	TURN ON Reclamation Pump							

1.227	TOP	VERIFY differential pressures on DPTs do not exceed 150 Psi						
1.228	TOP	FILL Rig to desired pressure ~150 Psi (adjust N2 pressure if needed)						
1.229	TOP	CLOSE Fill Iso Valve (MV-R218-05)						
1.230	TOP	TURN OFF Reclamation Pump						
1.231	TOP	VERIFY rig pressure increases with Nitrogen Regulator (MR-N2-01), repeat pump if not						
1.232	TOP	CLOSE Rec Pump Gas Valve (RPV-R218-01)						
1.233	TOP	CLOSE Rec Pump Gas Valve (RPV-R218-02)						
1.234	TOP	CLOSE Rec Tank Manual Liquid Valve (MV-R218-03)						
1.235	TOP	CLOSE High Pressure Valve (RM-R218-02)						
1.236	TOP	CLOSE Reclamation Valve (RM-R218-04)						
1.237	TOP	INCREASE N2 ullage pressure to test pressure (per test data sheet) (MR-N2-01)						
1.238	TOP	CLOSE N2 Hammer Valve (MV-N2-03)						
1.239	TOP	UNPLUG Reclamation Pump						
1.240	TOP	UNPLUG extention cord						

SECTION 2: ENGINE TEST

Step #	Action By	Operation	Test Numbers					
2.100a	N/A	WARNING: Do not over pressurize Low Pressure Gauge (RM-R218-05)						
2.001	TOP	IF SECTION 1.1 & 1.2 SKIPPED: INCREASE N2 ullage pressure to match rig pressure (MR-N2-01)						
2.002	TOP	IF SECTION 1.1 & 1.2 SKIPPED: OPEN N2 Hammer Valve (MV-N2-03) slowly						
2.003	TOP	IF SECTION 1.1 & 1.2 SKIPPED: INCREASE N2 ullage pressure to test pressure (MR-N2-01)						
2.004	TOP	IF SECTION 1.1 & 1.2 SKIPPED: CLOSE N2 Hammer Valve (MV-N2-03)						
2.005	TOP	WAIT for rig cool down						
2.006	DSO	UPDATE and VERIFY test settings on test data sheet						
2.007	TOP	VERIFY all tubes and hoses connected (per P&ID)						
2.008	TOP	VERIFY Pressure Isolation Valve (MV-ISO-01) open						
2.009	TOP	VERIFY Fill Iso Valve (MV-R218-05) closed						
2.010	TOP	VERIFY Vacuum Iso Valve (MV-R218-04) closed						
2.011	TOP	VERIFY Reclaim Iso Valve (MV-R218-06) closed						
2.012	TOP	VERIFY N2 Hammer Valve (MV-N2-03) closed						
2.013	TOP	VERIFY Hot Side Run Valve (MV-R218-08) open						
2.014	TOP	VERIFY Cold Side Run Valve (MV-R218-09) open						
2.015	TOP	VERIFY Recirculation Line Colse-Off Valve (MV-R218-10) open						
2.016	TOP	DO NOT RUN TEST WITH HAMMER VALVE OPEN						
2.017	TOP	VERIFY PT-TA-01, PT-TA-02, and PT-R218-01 are all reading desired test pressure						
2.018	TOP	VERIFY DPTs are reading 0 differential pressure						
2.019	TOP	If running standing wave conficuration: CLOSE MV-R218-08						
2.020	TOP	If running standing wave conficuration: CLOSE MV-R218-09						

2.021	TOP	PARTIALLY OPEN Water circulation Valve (MV-H20-01)							
2.022	TOP	VERIFY Water pressure does not exceed 10 psi							
2.023	TOP	MEASURE water mass flow rate using catch-and-weigh							
2.024	TOP	RECORD mass flow rate in test data sheet							
2.025	TOP	VERIFY TC-H20-01 and TC-H20-02 are reading ambient temperature							
2.026	TOP	PLUG IN Oil Heater							
2.027	TOP	VERIFY lid is placed on oil bath							
2.028	TOP	SET circuit protector to 'on' position							
2.029	TOP	PRESS power button							
2.030	TOP	SET desired temperature based on test data sheet							
2.031	TOP	SET speed to 'high'							
2.032	TOP	PRESS 'Enter' button to begin circulation							
2.033	TOP	VERIFY heating symbol and pump symbol are displayed on screen							
2.034	TOP	VERIFY TC-OIL-01 and TC-OIL-02 are reading desired temperature							
2.035	TOP	MONITOR PT-TA-01, TC-TA-01, TC-TA-02,TC-TA-03, TC-TA-04, and TC-TA-05							
2.036	TOP	When Oil temperature reaches 75 C: CLOSE Pressure Isolation Valve (MV-ISO-01)							
2.037	TOP	MONITOR DPTs to verify differential pressure does not exceed 150psid							
2.038	TOP	if differential Pressure exceeds 150 psid:OPEN Pressure Isolation Valve (MV-ISO-01)							
2.039	TOP	BEGIN data recording							
2.040	TOP	MONITOR PT-TA-01, and PT-TA-02							
2.041	TOP	If pressure increases rapidly:OPEN Cold Side Run Valve (MV-R218-09)							
2.042	DSO	SAVE .tdls files onto home drive							
2.043	DSO	UPDATE test data sheet							
2.044	TOP	When testing is done: Open MV-ISO-01							
2.045	TOP	PRESS 'Enter' button on oil to stop circulation							
2.046	TOP	SET oil bath heater setting to 'OFF'							
2.047	TOP	SET circuit protector to 'off' position							
2.048	TOP	CLOSE water supply valve (MV-H20-01)							
2.049	TOP	EQUALIZE N2 pressure on N2 Regulator (MR-N2-01) To PT-TA-01							
2.050	TOP	IF LEAVING REF IN: OPEN N2 Hammer Valve slowly (MV-N2-03)							
2.051	TOP	if standing wave configuration: OPEN MV-R218-08 and MV-R218-09							
2.052	TOP	if traveling wave configuration: OPEN circulation line Close-Off Valve (MV-R218-10)							
2.053	TOP	RELIEVE N2 Regulator to (MR-N2-01) ~230 psi							
2.054	TOP	IF LEAVING REF IN: CLOSE N2 Hammer Valve (MV-N2-01)							
2.055	TOP	IF LEAVING REF IN: SKIP to Section 3.2							

SECTION 3: SHUT DOWN

Step #	Action By	Operation	Test Numbers
0. Reclamation Cycle			

3.001a	N/A	WARNING: Do not over pressurize Low Pressure Gauge (RM-R218-05)							
3.001	TOP	VERIFY all tubes and hoses connected (per P&ID)							
3.002	TOP	VERIFY Vacuum Iso Valve closed (MV-R218-04)							
3.003	TOP	VERIFY Fill Iso Valve closed (MV-R218-05)							
3.004	TOP	VERIFY Reclaim Iso Valve closed (MV-R218-06)							
3.005	TOP	VERIFY Hot Side Run Valve open (MV-R218-08)							
3.006	TOP	VERIFY Cold Side Run Valve open (MV-R218-09)							
3.007	TOP	VERIFY Pressure Isolation Valve (MV-ISO-0)1 is Open							
3.008	TOP	VERIFY circulation line Close-Off Valve (MV-R218-10) is open							
3.009	TOP	VERIFY all valves closed on Refrigerant Manifold							
3.010	TOP	PLUG IN extention cord if not already plugged in							
3.011	TOP	PLUG IN Reclamation Pump							
3.012	TOP	INCREASE N2 Regulator to equalize pressure (MR-N2-01)							
3.013	TOP	OPEN N2 Hammer Valve (MV-N2-03) slowly							
3.014	TOP	DECREASE N2 Regulator to ~ 100 psia (MR-N2-01)							
3.015	TOP	OPEN Reclamation Manual Gas Valve (MV-R218-02)							
3.016	TOP	OPEN Reclamation Pump Liquid Valve (RPV-R218-01)							
3.017	TOP	OPEN Reclamation Pump Gas Valve (RPV-R218-02)							
3.018	TOP	OPEN Reclamation Valve (RM-R218-04)							
3.019	TOP	OPEN High Pressure Valve (RM-R218-02)							
3.020	TOP	OPEN Low Pressure Valve (RM-R218-01)							
3.021	TOP	OPEN Vacuum Iso Valve (MV-R218-04) slowly							
3.022	TOP	OPEN Reclaim Iso Valve (MV-R218-06)							
3.023	TOP	VERIFY pressure doesn't exceed limit on Reclamation Pump Liquid Gague							
3.024	TOP	TURN ON Reclamation Pump							
3.025	TOP	RECLAIM refrigerant until Rec Pump Liquid Valve (RP-R218-01) reaches 28 in Hg							
3.026	TOP	TURN OFF Reclamation Pump							
3.027	TOP	CLOSE Vacuum Iso Valve (MV-R218-04)							
3.028	TOP	WAIT a few minutes for fluid in Reclamation tank to condense							
3.029	TOP	OPEN Vacuum Iso Valve (MV-R218-04)							
3.030	TOP	TURN ON Reclamation Pump and reclaim for another 30 seconds							
3.031	TOP	TURN OFF Reclamation Pump							
3.032	TOP	CLOSE Reclamation Manual Liquid Valve (MV-R218-02)							
3.033	TOP	CLOSE Reclamation Pump Liquid Valve (RPV-R218-01)							
3.034	TOP	CLOSE Reclamation Pump Gas Valve (RPV-R218-02)							
3.035	TOP	CLOSE Reclamation Valve (RM-R218-04)							
3.036	TOP	CLOSE High Pressure Valve (RM-R218-02)							
3.037	TOP	CLOSE Low Pressure Valve (RM-R218-01)							

3.038	TOP	CLOSE Vacuum Iso Valve (MV-R218-04)							
3.039	TOP	CLOSE Reclaim Iso Valve (MV-R218-06)							
3.040	TOP	UNPLUG Reclamation Pump							
3.041	TOP	UNPLUG extention cord							
3.042	TOP	BACK OFF N2 Regulator (MR-N2-01)							
1. Rig/Instrumentation Shut Down									
3.101	TOP	VERIFY N2 Hammer Valve (MV-N2-03) closed							
3.102	TOP	UNLOAD N2 Regulator (MR-N2-01)							
3.103	TOP	VERIFY all valves closed on Refrigerant Manifold							
3.104	TOP	VERIFY MV-R218-08 and MV-R218-09 are open							
3.105	TOP	VERIFY MV-ISO-01 is open							
3.106	TOP	VERIFY MV-R218-10 is open							
3.107	TOP	SHUT OFF N2 Supply (MV-N2-01)							
3.108	TOP	REMOVE fitting from downstream side of N2 Regulator (MR-N2-01)							
3.109	TOP	INCREASE N2 Regulator (MR-N2-01) until nitrogen vented							
3.110	TOP	UNLOAD N2 Regulator (MR-N2-01)							
3.111	TOP	REPLACE fitting on downstream side of N2 Regulator (MR-N2-01)							
3.112	TOP	CLOSE N2 Iso Valve (MV-N2-02)							
3.113	TOP	RECORD current bulk pressure if leaving ref in							
3.114	DSO	STOP Acquire All on LabView VI							
3.115	DSO	CLOSE LABView VI							
3.116	DSO	CLOSE all other windows							
3.117	DSO	TURN OFF 28V DC regulated power supply							
3.118	DSO	TURN OFF 12V DC regulated power supply							
3.119	DSO	TURN OFF computer							
3.120	TOP	DISCONNECT wires for storage							
3.121	TOP	UNPLUG extention cord (if plugged in)							
3.122	TOP	UNPLUG oil heater							
3.123	SAF	TURN OFF testing light							
3.124	SAF	TAKE DOWN testing sign							

APPENDIX A: AS NEEDED PROCEDURES

Step #	Action By	Operation	Test Numbers
1. Vent and Vacuum Rec Tank and Tubes			
A.100a	N/A	WARNING: Vacuum pump gets hot during use	
A.100b	N/A	WARNING: Vacuum Pump may exhaust water/oil vapor until all is gone from lines	
A.100c	N/A	WARM UP pump before vacuuming anything (run about a minute)	
A.100d	N/A	REFER to operation manual for oil replacement procedure if needed	

A.101	TOP	VENT Rec tank of N2 using Rec Relief Valve (MV-R218-05) (Schrader Valve)							
A.102	TOP	CHECK oil level on vacuum pump; FILL if low							
A.103	TOP	VERIFY all valves closed on Refrigerant Manifold							
A.104	TOP	VERIFY all tubes and hoses connected (per P&ID)							
A.105	TOP	VERIFY Vacuum Iso Valve closed (MV-R218-04)							
A.106	TOP	VERIFY Fill Iso Valve closed (MV-R218-05)							
A.107	TOP	VERIFY Reclaim Iso Valve closed (MV-R218-06)							
A.109	TOP	TURN ON Vacuum Pump							
A.110	TOP	OPEN Ref Tank Liquid Valve (MV-R218-03)							
A.111	TOP	OPEN Ref Tank Gas Valve (MV-R218-02)							
A.112	TOP	VACUUM until vacuum (28 in Hg) is reached on Low Pressure Gauge (RM-R218-05)							
A.113	TOP	TURN OFF Vacuum Pump							
A.114	TOP	CLOSE Ref Tank Liquid Valve (MV-R218-03)							
A.115	TOP	CLOSE Ref Tank Gas Valve (MV-R218-02)							
2. Leak Check									
A.200a	N/A	DO these steps after a re-assembly and when no ref is in the system							
A.201	TOP	VERIFY N2 Regulator unloaded (MR-N2-01)							
A.202	TOP	OPEN N2 Supply Valve (MV-N2-01) if not already open							
A.203	TOP	VERIFY Pressure Isolation Valve (MV-ISO-01) is open							
A.204	TOP	VERIFY Hot Side Run Valve (MV-R218-08) is open							
A.205	TOP	VERIFY Cold Side Run Valve (MV-R218-09) open							
A.206	TOP	VERIFY Vacuum Iso Valve closed (MV-R218-04)							
A.207	TOP	VERIFY Fill Iso Valve closed (MV-R218-05)							
A.208	TOP	VERIFY Reclaim Iso Valve closed (MV-R218-06)							
A.209	TOP	VERIFY Rig Close-Off Valve open (MV-R218-10)							
A.210	TOP	DISCONNECT manifold from Vacuum Iso Valve (MV-R218-04)							
A.211	TOP	DISCONNECT N2 hose from N2 line							
A.212	TOP	CONNECT N2 hose to Vacuum Iso Valve (MV-R218-04)							
A.213	TOP	OPEN Vacuum Iso Valve (MV-R218-04)							
A.214	TOP	INCREASE N2 Regulator (MR-N2-01) to desired pressure (500 psi)							
A.215	TOP	SNOOP for leaks							
A.216	TOP	FIX leaks							
A.217	TOP	BACK OFF N2 Regulator (MR-N2-01)							
A.218	TOP	CLOSE Vacuum Iso Valve (MV-R218-04)							
A.219	TOP	DISCONNECT N2 hose from Vacuum Iso Valve (MV-R218-04)							
A.220	TOP	CONNECT N2 hose to N2 Hammer Valve (MV-N2-03)							
A.221	TOP	OPEN N2 Hammer Valve (MV-N2-03)							
A.222	TOP	REPEAT steps A.209-A.211 to leak check N2 side if needed							

A.223	TOP	CLOSE N2 Supply Valve (MV-N2-01) if no longer needed							
A.224	TOP	REMOVE fitting from downstream side of N2 Regulator (MR-N2-01)							
A.225	TOP	INCREASE N2 Regulator (MR-N2-01) until nitrogen vented							
A.226	TOP	UNLOAD N2 Regulator (MR-N2-01)							
A.227	TOP	REPLACE fitting on downstream side of N2 Regulator (MR-N2-01)							
A.228	TOP	CLOSE N2 Iso Valve (MV-N2-02)							

3. Vacuum Jacket Heat Exchanger

A.301a	TOP	DO these steps when center of heat exchanger needs to be vacuumed for insulation							
A.301b	N/A	WARNING: Vacuum pump gets hot during use							
A.301c	N/A	WARNING: Vacuum Pump may exhaust water/oil vapor until all is gone from lines							
A.301d	N/A	REFER to operation manual for oil replacement procedure if needed							
A.301	TOP	Disconnect Vacuum Pump line from Refrigerant Manifold (RM-R218-03) and connect to vacuum jacket isolation valve (MV-VAC-01)							
A.302	TOP	PLUG IN extention cord							
A.303	TOP	PLUG IN Vacuum Pump							
A.304	TOP	VERIFY exhaust cap removed							
A.305	TOP	CHECK oil level on vacuum pump							
A.306	TOP	FILL if low (should fill half of sight glass while running)							
A.307	TOP	TURN ON Vacuum Pump							
A.308	TOP	RUN Vacuum Pump for about 1 minute to warm up							
A.309	TOP	OPEN Vacuum Jacket Isolation Valve (MV-VAC-01)							
A.310	TOP	VACUUM for approximately 30 s							
A.311	TOP	CLOSE Vacuum Jacket Isolation Valve (MV-VAC-01)							
A.312	TOP	TURN OFF Vacuum Pump							
A.313	TOP	UNPLUG Vacuum Pump							

APPENDIX B: EMERGENCY PROCEDURES

Step #	Action By	Operation	Test Numbers
--------	-----------	-----------	--------------

1. In Case of Vacuum Pump Oil Spill

B.101	ALL	VERIFY oil drain fitting and oil tank cap are closed and secure							
B.102	ALL	WIPE UP oil spill with soap, water and paper towels							
B.103	ALL	DRY area to ensure oil is cleaned up							
B.104	ALL	DISPOSE OF paper towels in a trash can							
B.105	ALL	VERIFY Vacuum Pump is cleaned of oil							
B.106	ALL	VERIFY floor, hands and treset rig is clear of oil							

2. In Case of Heat Exchanger Oil Spill

B.201	ALL	TURN OFF oil pump circulation and heat (get exact proc. For pump)							
-------	-----	---	--	--	--	--	--	--	--

B.202	ALL	WAIT for oil to cool down to room temperature							
B.203	ALL	WIPE UP oil spill with soap, water and paper towels							
B.204	ALL	DRY area to ensure oil is cleaned up							
B.205	ALL	DISPOSE OF paper towels in a trash can							
B.206	ALL	VERIFY floor, hands and test rig is clear of oil							
B.207	ALL	VERIFY lid is placed on oil bath							
3. In Case of R-218 Spill									
B.301	ALL	PLUG leaks if possible (vacuum putty in control room)							
B.302	ALL	Reclaim R-218							
B.303	ALL	OPEN Exhaust Vent							
B.304	ALL	TURN ON Exhaust Fan							
B.305	ALL	STOP all leaks							
B.306	ALL	DO NOT breathe or vent R-218 if possible							
4. In Case of leak under Ref pressure									
B.301	ALL	TURN OFF oil pump circulation and heat							
B.302	ALL	CLOSE Water valve (MV-H2O-01)							
B.303	ALL	CLOSE rig close-off valve (MV-R218-10)							
B.304	ALL	OPEN Exhaust Vent							
B.305	ALL	TURN ON Exhaust Fan							
B.306	ALL	STOP all leaks							
B.307	ALL	USE vacuum putty to block leaks							
B.308	ALL	RECLAIM refrigerant							
5. In Case of R-218 Over-Pressurization (>650 psi)									
B.501	ALL	SET circuit protector to the 'o' position							
B.502	ALL	UNLOAD MV-N2-03							
B.503	ALL	VERIFY pressure in test article has equalized							
B.504	ALL	DIAGNOSE cause of over-pressurization and select appropriate path moving forward							

A.8 Complete Test Results

Test Matrix A: Assess the performance improvement provided by heat exchanger over heating cartridges

Test Number	Bulk Pressure (psi)	Bulk Pressure (Mpa)	P/P_cr	T hot (K)	Tcold (K)	Delta T (K)	Amplitude (psid)	Amplitude (Kpa)	Frequency (Hz)	Water LPM	Oil Setting
1	396	2.73	1.03	388	307	79	3.55	24.5	3.69	9.65	1
2	380	2.62	0.99	371	283	89	3.18	21.9	3.57	11.96	1
3	403	2.78	1.05	371	293	79	3.27	22.5	3.53	2.03	1
4	495	3.41	1.29	371	289	83	1.14	7.9	4.65	3.62	1

Test Matrix B: Characterize thermoacoustic behavior with varying bulk pressure and Delta T

Test Number	Bulk Pressure (psi)	Bulk Pressure (Mpa)	P/P_cr	T hot (K)	Tcold (K)	Delta T (K)	Amplitude (psid)	Amplitude (Kpa)	Frequency (Hz)	Water LPM	Oil Setting
48	352	2.43	0.92	374	296	78	31.8	219	4.73	3.85	1
49	360	2.48	0.94	374	295	78	30.9	213	4.72	3.85	1
51	381	2.62	0.99	374	295	79	32.1	221	4.81	3.85	1
52	396	2.73	1.03	374	295	79	30.0	207	4.87	3.85	1
53	433	2.99	1.13	374	295	79	28.0	193	4.93	3.85	1
54	456	3.14	1.19	374	295	79	24.5	169	4.95	3.85	1
55	508	3.50	1.33	374	295	79	19.8	137	5.16	3.85	1
22	351	2.42	0.92	392	287	105	46.0	317	4.94	3.50	4
23	365	2.51	0.95	392	287	105	46.2	319	4.98	3.50	4
24	379	2.61	0.99	392	286	106	50.8	351	5.11	3.50	4
25	412	2.84	1.08	392	287	105	51.9	358	5.30	3.50	4
26	431	2.97	1.13	392	286	105	51.8	357	5.34	3.50	4
27	465	3.21	1.21	392	286	106	50.8	350	5.39	3.50	4
28	485	3.34	1.27	392	286	106	48.7	336	5.40	3.50	4
32	347	2.39	0.91	410	294	116	52.1	359	5.08	3.96	7
38	352	2.42	0.92	410	294	116	53.8	371	5.09	3.96	7
33	394	2.71	1.03	410	294	116	60.0	414	5.39	3.96	7
35	410	2.83	1.07	410	294	116	61.8	426	5.48	3.96	7
34	420	2.90	1.10	410	294	116	63.7	439	5.53	3.96	7
36	460	3.17	1.20	410	294	116	63.4	437	5.59	3.96	7
37	479	3.30	1.25	410	294	116	63.5	438	5.63	3.96	7
39	333	2.29	0.87	428	294	134	64.4	444	5.23	3.63	10
40	345	2.38	0.90	428	294	134	65.7	453	5.25	3.63	10
41	368	2.54	0.96	428	294	134	68.2	470	5.33	3.63	10
42	396	2.73	1.04	428	294	134	71.1	491	5.55	3.63	10
43	406	2.80	1.06	428	294	134	72.3	498	5.61	3.63	10
44	432	2.98	1.13	428	294	134	81.1	559	5.79	3.63	10
45	498	3.43	1.30	428	294	134	83.2	574	5.95	3.63	10
46	329	2.27	0.86	445	294	151	79.8	550	5.34	3.63	13
47	335	2.31	0.87	445	294	151	81.2	560	5.38	3.63	13
56	380	2.62	0.99	445	295	150	84.6	583	5.50	3.85	13
58	394	2.71	1.03	444	295	150	82.2	567	5.57	3.85	13
57	401	2.76	1.05	444	295	150	81.3	560	5.61	3.85	13
59	459	3.16	1.20	445	295	150	95.1	656	5.96	3.85	13
60	491	3.39	1.28	445	295	150	97.0	669	6.04	3.85	13

Test Matrix C: Assess the impact of varying resonator length on thermoacoustic response

Test Number	Bulk Pressure (psi)	Bulk Pressure (Mpa)	P/P_cr	T hot (K)	Tcold (K)	Delta T (K)	Amplitude (psid)	Amplitude (Kpa)	Frequency (Hz)	Water LPM	Oil Setting
35	410	2.83	1.07	410	294	116	61.8	426	5.48	3.96	7
34	420	2.90	1.10	410	294	116	63.7	439	5.53	3.96	7
36	460	3.17	1.20	410	294	116	63.4	437	5.59	3.96	7
70	403	2.78	1.05	413	297	116	62.0	428	5.88	3.82	7
69	416	2.87	1.09	413	297	116	64.2	443	5.97	3.82	7
71	459	3.17	1.20	413	297	116	68.6	473	6.11	3.82	7
67	406	2.80	1.06	413	297	116	58.1	400	6.39	3.78	7
66	422	2.91	1.10	414	297	117	61.6	425	6.52	3.78	7
68	460	3.17	1.20	413	297	116	65.6	452	6.61	3.78	7
73	402	2.77	1.05	413	297	116	53.4	368	6.91	3.82	7
72	422	2.91	1.10	413	297	116	58.5	403	7.10	3.82	7
74	458	3.16	1.20	413	297	116	62.4	430	7.18	3.82	7
75	401	2.76	1.05	413	297	116	46.0	317	7.54	3.82	7
77	421	2.90	1.10	413	297	116	50.2	346	7.70	3.82	7
78	462	3.19	1.21	413	296	116	55.7	384	7.87	3.82	7

Test Matrix D: Assess fluid pumping capabilities at Delta T = 116 K

Test Number	Bulk Pressure (psi)	Bulk Pressure (Mpa)	P/P_cr	T hot (K)	Tcold (K)	Delta T (K)	Amplitude (psid)	Amplitude (Kpa)	Frequency (Hz)	Mass Flow Rate	Valve Angle	Water LPV	Oil Setting
99	405	2.79	1.06	413	297	116	60.9	420	5.89	0.000	0	3.82	7
100	417	2.87	1.09	413	297	116	58.7	404	5.89	0.000	10	3.82	7
101	417	2.88	1.09	413	297	116	58.7	405	5.89	0.000	20	3.82	7
102	404	2.79	1.06	413	297	116	2.3	16	5.29	0.545	30	3.82	7
103	404	2.79	1.06	413	297	116	1.9	13	5.39	0.514	40	3.82	7
104	403	2.78	1.05	413	297	116	1.9	13	5.40	0.503	50	3.82	7
105	402	2.78	1.05	413	297	115	2.0	13	5.40	0.513	60	3.82	7
106	402	2.77	1.05	413	297	115	2.0	14	5.38	0.535	70	3.82	7
107	401	2.77	1.05	413	297	115	2.0	13	5.41	0.524	80	3.82	7
108	401	2.76	1.05	413	297	115	2.0	14	5.43	0.522	90	3.82	7
79	422	2.91	1.10	413	297	116	60.1	414	5.92	0.000	0	3.82	7
80	422	2.91	1.10	413	297	116	60.2	415	5.90	0.000	10	3.82	7
81	422	2.91	1.10	413	297	116	60.3	416	5.90	0.000	20	3.82	7
82	405	2.79	1.06	413	297	116	2.3	16	5.45	0.629	30	3.82	7
83	406	2.80	1.06	413	297	116	2.0	14	5.39	0.509	40	3.82	7
84	406	2.80	1.06	413	297	116	1.9	13	5.43	0.503	50	3.82	7
85	406	2.80	1.06	413	297	116	1.9	13	5.38	0.508	60	3.82	7
86	405	2.79	1.06	413	297	116	2.0	13	5.43	0.513	70	3.82	7
87	404	2.79	1.06	413	297	115	2.0	14	5.41	0.499	80	3.82	7
89	458	3.16	1.20	413	297	116	67.8	468	6.11	0.000	0	3.82	7
90	467	3.22	1.22	413	297	116	63.0	434	6.03	0.000	10	3.82	7
91	467	3.22	1.22	413	297	116	63.0	434	6.03	0.000	20	3.82	7
92	451	3.11	1.18	413	297	116	1.9	13	5.55	0.414	30	3.82	7

93	450	3.10	1.17	413	297	116	1.9	13	5.53	0.401	40	3.82	7
94	448	3.09	1.17	413	297	116	1.9	13	5.53	0.417	50	3.82	7
95	446	3.08	1.17	413	297	116	1.9	13	5.53	0.424	60	3.82	7
96	445	3.07	1.16	413	297	116	1.9	13	5.53	0.431	70	3.82	7
97	444	3.06	1.16	413	297	116	1.9	13	5.53	0.432	80	3.82	7
98	443	3.05	1.16	413	297	116	1.9	13	5.51	0.450	90	3.82	7

Test Matrix E: Assess fluid pumping capabilities at Delta T = 134 K

Test Number	Bulk Pressure (psi)	Bulk Pressure (Mpa)	P/P_cr	T hot (K)	Tcold (K)	Delta T (K)	Amplitude (psid)	Amplitude (Kpa)	Frequency (Hz)	Mass Flow Rate	Valve Angle	Water LPM	Oil Setting
110	401	2.77	1.05	431	297	134	73.8	509	6.05	0.000	0	3.87	10
111	401	2.76	1.05	430	297	133	62.3	430	5.91	0.417	20	3.87	10
115	415	2.86	1.08	430	297	133	10.6	73	5.09	1.327	25	3.87	10
112	405	2.79	1.06	430	297	133	2.3	16	5.59	0.680	30	3.87	10
113	405	2.79	1.06	430	297	133	2.3	16	5.59	0.659	90	3.87	10
116	418	2.88	1.09	430	297	134	73.4	506	6.13	0.000	0	3.87	10
117	411	2.83	1.07	430	297	134	32.8	226	5.44	1.277	20	3.87	10
118	417	2.87	1.09	430	297	134	28.1	194	5.35	1.498	25	3.87	10
119	427	2.95	1.12	430	297	133	0.8	6	5.76	0.000	30	3.87	10
120	408	2.81	1.06	430	297	133	2.3	16	5.57	0.685	50	3.87	10
121	403	2.78	1.05	430	297	133	2.3	16	5.58	0.665	90	3.87	10
122	462	3.18	1.21	431	297	134	84.0	579	6.33	0.000	0	3.87	10
124	456	3.14	1.19	430	297	133	24.4	168	5.40	1.627	20	3.87	10
123	452	3.12	1.18	430	297	133	11.8	82	5.32	1.204	30	3.87	10
125	442	3.05	1.15	430	297	133	2.3	16	5.62	0.613	50	3.87	10
126	435	3.00	1.14	430	297	133	2.2	16	5.64	0.627	90	3.87	10
127	498	3.44	1.30	431	297	134	85.4	589	6.44	0.000	0	3.87	10
128	501	3.45	1.31	430	297	134	65.9	454	6.17	0.939	25	3.87	10
129	494	3.40	1.29	430	297	133	2.4	17	5.73	0.530	30	3.87	10
130	464	3.20	1.21	430	297	133	2.2	15	5.70	0.568	90	3.87	10

Test Matrix F: Assess fluid pumping capabilities at Delta T = 150

Test Number	Bulk Pressure (psi)	Bulk Pressure (Mpa)	P/P_cr	T hot (K)	Tcold (K)	Delta T (K)	Amplitude (psid)	Amplitude (Kpa)	Frequency (Hz)	Mass Flow Rate	Valve Angle	Water LPM	Oil Setting
131	401	2.76	1.05	445	297	148	84.7	584	6.12	0.000	0.0	3.97	13
132	404	2.78	1.05	445	297	148	50.8	351	5.68	1.136	23.0	3.97	13
167	390	2.69	1.02	445	297	148	39.1	270	5.39	1.450	24.7	3.93	13
168	385	2.65	1.01	445	297	148	4.6	32	5.25	1.055	26.6	3.93	13
133	387	2.67	1.01	445	297	148	3.2	22	5.59	0.918	27.2	3.97	13
134	386	2.66	1.01	445	297	148	2.8	19	5.75	0.881	90.0	3.97	13
144	418	2.88	1.09	445	297	148	80.1	552	6.21	0.000	0.0	3.93	13
145	417	2.88	1.09	445	297	148	69.0	476	6.06	0.494	22.7	3.93	13
147	419	2.89	1.09	445	297	148	63.9	441	5.98	0.717	23.1	3.93	13
146	426	2.94	1.11	445	297	148	6.6	45	5.76	1.510	25.7	3.93	13
148	421	2.91	1.10	445	297	148	5.2	36	5.76	1.428	27.3	3.93	13
149	362	2.50	0.95	445	296	148	4.0	28	5.59	1.149	30.0	3.93	13

150	354	2.44	0.92	445	296	149	3.0	21	5.77	1.028	90.0	3.93	13
151	453	3.12	1.18	445	296	149	96.6	666	6.47	0.000	0.0	3.93	13
152	447	3.08	1.17	445	296	149	80.7	557	6.27	0.748	22.5	3.93	13
156	448	3.09	1.17	445	297	148	79.5	548	6.24	0.768	21.2	3.93	13
157	457	3.15	1.19	445	297	148	45.3	312	5.70	2.128	24.8	3.93	13
158	457	3.15	1.19	445	297	148	36.6	252	5.56	2.159	20.8	3.93	13
153	451	3.11	1.18	445	297	149	30.9	213	5.48	2.071	25.1	3.93	13
159	438	3.02	1.14	445	297	148	5.8	40	5.25	1.419	22.4	3.93	13
154	430	2.96	1.12	445	297	148	3.4	23	5.53	0.834	28.1	3.93	13
155	421	2.90	1.10	445	297	148	2.6	18	5.71	0.774	90.0	3.93	13
160	492	3.39	1.29	445	297	148	100.0	690	6.57	0.000	0.0	3.93	13
165	493	3.40	1.29	445	297	148	93.6	646	6.48	0.180	22.5	3.93	13
161	479	3.30	1.25	445	297	148	80.9	558	6.30	0.949	23.4	3.93	13
166	489	3.37	1.28	445	297	148	51.6	356	5.87	2.061	26.4	3.93	13
162	463	3.19	1.21	445	297	148	4.9	34	5.41	1.198	25.2	3.93	13
163	444	3.06	1.16	445	297	148	2.8	20	5.66	0.762	28.1	3.93	13
164	429	2.96	1.12	445	297	148	2.6	18	5.72	0.775	90.0	3.93	13

Oil Flow Rate Setting Options		
setting options	temp [deg C]	pump speed
1	100	high
2	100	med
3	100	low
4	117.78	high
5	117.78	med
6	117.78	low
7	135	high
8	135	med
9	135	low
10	153.3	high
11	153.3	med
12	153.3	low
13	171.1	high
14	171.1	med
15	171.1	low